

© 2016 Vishal V. R. Nandigana

INFLUENCE OF EXTERNAL ENVIRONMENT ON FLUID/ION TRANSPORT IN  
CONFINED NANOSCALE SYSTEMS

BY

VISHAL V. R. NANDIGANA

DISSERTATION

Submitted in partial fulfillment of the requirements  
for the degree of Doctor of Philosophy in Mechanical Engineering  
in the Graduate College of the  
University of Illinois at Urbana-Champaign, 2016

Urbana, Illinois

Doctoral Committee:

Professor Narayana R. Aluru, Chair  
Professor Emeritus Surya P. Vanka  
Professor Placid M. Ferreira  
Professor Paul J. A. Kenis

# Abstract

The advancements in micro–nano–manufacturing technology has lead to a significant leap in understanding the nuances of transport phenomenon in nanopore architecture. The large nanopore surface compared to the volume favors a predominant transport of ions. The environment results in a near ideal ion–selective nanoporous membrane. The selective nature of ions can be triggered in the fields like single molecule/particle sensing, preconcentration of analytes using electric field focusing and desalination applications. A single nanoporous membrane leveraged with microporous reservoirs manifests the current in the system supporting the engineering and biosciences applications. The external microporous environment influences the transport in a nanopore. My field of contribution contradicts the existing theories and methodologies.

Earlier works revealed a non-monotonic growth in the current–voltage characteristics in a nanoporous membrane. The experimental observations predicted a deviation from the classical diffusion–limited current transport theory, which highlights a saturation of the current density at higher applied voltages with an infinite differential resistance. Furthermore, the quasi–equilibrium regime confers a monotonic increase in the current, following the Ohm’s law. However, at a critical voltage ( $V_{LI}$ ), the current increases infinitesimally postulating a novel limiting resistance regime (LRR) in contradiction to self diffusion mechanism. A push in voltage manifests a second critical voltage ( $V_{LII}$ ), referred to as the overlimiting current regime with a higher slope, and constant conductivity.

Many plausible mechanisms are discussed to explain the overlimiting current characteristics. Using a 1–D ideal ion–selective membrane model a possible mechanism for the limiting resistance region deviating from the self diffusion mechanism was set forth. Further, the theory predicted a region of induced charge arising in the unstable depletion micro–nano junction owing to the convective fluid instabilities. Experimental works were navigated this field of research and postulated

a probable convective fluid and charge instabilities for the overlimiting current characteristics in micro–nanostructures. However, an exact physical understanding of the large, yet finite differential resistance, in the limiting resistance regime, in conjecture with the transition to the overlimiting regime and the true overlimiting current mechanism is still unexplored.

In this thesis, I have explained the fundamental physics unraveling the mystery of overlimiting current in micro–nano interconnect architecture. A comprehensive physical model to discuss all the three current regions are numerically predicted by considering the microporous membrane interconnected with nanochannel. I tackled this problem by using a detailed 2–D nonlinear, nonideal ion–selective model. Further, I discuss the necessary governing equations required to model the system. The model illustrates a constant conductivity in the overlimiting current, consistent with all the experimental observations. I highlight the mechanism, by analyzing the behavior of the ionic concentration, near the depletion junction of the cathodic microporous membrane integrated with nanochannel. The redistribution of charges at the depletion junction manifests in the overlimiting current, in contradiction to convective charge/fluid instabilities at this junction. My understanding propelled me to investigate the charge dynamics in the nanoporous membranes influenced by external microporous architecture. To this end, I first reduce the order of the governing equations, developing a novel dynamical area–averaged multi–ion transport model (DAAM). The concentration and electric potential are integrated in the radial direction. Furthermore, the convective fluid flow contribution plays an insignificant role in the mechanism, and hence, is neglected in my DAAM model. To understand the charge dynamics, I proposed a novel computational impedance spectroscopy model (CIS). Henceforth, we apply a harmonic electric potential in the system and investigate the harmonic output current. I infer the phase effects between the concentration and the electric potential wave, and determine the system dynamics under equilibrium, quasi–equilibrium (Ohmic regime), limiting resistance regime and in the overlimiting current regime.

My findings led to a fruitful collaboration with the experimentalists to invent a novel nano–diode. The invention is in conjecture with a bio–inspired gating channel, with an added advantage of their application in radioactive environment. The semiconductor diodes fail to serve this purpose. The advantage stems from the fact that the current rectification (ON/OFF states) can be put forth by the change in the the cross-sectional area of the external microporous environment leveraged with a

nanopore in addition to the migration of the enriched and depleted concentration zones. Temporal power spectra map of the ON state current dynamics postulated an electroconvective origin from our experimental observations.

However, I present an advanced theoretical correlation between the ON state current dynamics (for nano–diodes) with the chaotic clustering of ions at the anodic micro–nano enriched/Avalanche regime. I mathematically quantify chaos in terms of maximum Lyapunov exponent. The maximum Lyapunov exponent increases monotonically with an increase in the applied bias voltage and the macropore reservoir diameter. Furthermore, I postulate a low frequency “ $1/f$ ” type dynamics for the voltage dominated chaos and “ $1/f^2$ ” type dynamics for the macropore reservoir dominated chaos.

Finally, I establish a new route for depletion induced chaos postulated by earlier works using a deterministic hypothesis. The depletion chaos is manifested at near ideal ion–selective condition and under nonequilibrium potential. The maximum Lyapunov exponent monotonically increases with the ideality and is independent of the applied voltage. The current oscillations are inherited at the theoretical ideal limit highlighting the propagation of the ion depletion region from the external microporous membrane towards the nanostructure. The nonequilibrium instability in potential navigates this result. The potential instability leads to bidirectional ion hopping, fabricating in chaotic motion of the ions. I postulate a novel correlation between the temporal map and the depletion chaos and propose a new mechanism for  $1/f$  type dynamics in nanoporous membranes.

# Acknowledgments

With regard to the journey of my PhD program, Dr. Narayan was the pioneering man in my research efforts. Our fruitful discussions led to a successful roadmap towards my character enrichment in science and non-engineering walks of life. Our vision in nanofluidics corroborated a successful collaboration with Dr. Aaron T. and Dr. Kyoo J, from university of Notre Dame and US Army construction for Engineering research laboratory, respectively. During the journey of my PhD, my successful planning had initiated an intra department collaboration with Dr. John R. from Materials Research Laboratory and an international collaboration with Dr. Aleksandra R. from, *École Polytechnique Fdrale de Lausanne (EPFL)*, Switzerland. I like to extend my congratulations to Jiandong F. and Mohammad H. for their contribution on osmotic power generator. I wish to extend my support to all my reviewers. My interactions with my colleagues helped us to actively kinder our minds towards our research. More importantly, I would like to present my direct appreciation to my parents, Dr. Krishna Mohan Nandigana, and my mother Mrs. Lakshmi Nandigana.

My research was supported by National Science Foundation (NSF) under Grants 0328162 (nano-CEMMS, UIUC), 0852657, 0915718, 0941497, 1264282, 1420882, 1506619 and 1545907 and AFOSR under grant FA9550-12-1-0464. The other collaborative support includes, European Research Council (grant no. 259398, PorABEL) and funding from the European Unions Seventh Framework Programme FP7/2007-2013 under Grant Agreement No. 318804 (SNM) and Swiss SNF Sinergia Grant no. 147607. I acknowledge the use of the parallel computing resource provided by the University of Illinois. I like to extend my support to Micheal Campbell for fruitful discussions and help with regard to efficient resource utilization in the parallel cluster.

# Table of Contents

<b>Chapter 1 Understanding anomalous current - voltage characteristics in microchannel nanochannel interconnect devices . . . . .</b>	<b>1</b>
1.1 Abstract . . . . .	1
1.2 Introduction . . . . .	1
1.3 Theory . . . . .	3
1.4 Simulation Details . . . . .	8
1.5 Results and Discussion . . . . .	9
1.6 Anomalous current rectification under combined AC/DC electric fields . . . . .	13
1.7 Derivation of limiting current and first critical voltage . . . . .	17
1.8 Conclusions . . . . .	20
1.9 Tables . . . . .	22
1.10 Figures . . . . .	23
1.11 References . . . . .	37
<b>Chapter 2 Characterization of electrochemical properties of a micro-nano channel integrated system using computational impedance spectroscopy (CIS) . .</b>	<b>38</b>
2.1 Abstract . . . . .	38
2.2 Introduction . . . . .	39
2.3 Theory . . . . .	41
2.4 Simulation details . . . . .	43
2.5 Results and discussion . . . . .	44
2.6 Area-averaged multi-ion transport model (AAM) . . . . .	56
2.7 Impedance calculation . . . . .	61
2.8 Characterization of DBL thickness . . . . .	63
2.9 AC rectification effects . . . . .	64
2.10 Conclusions . . . . .	66
2.11 Tables . . . . .	68
2.12 Figures . . . . .	72
2.13 References . . . . .	84
<b>Chapter 3 Controlling the Ionic Current Rectification Factor of a Nanofluidic/Microfluidic Interface with Symmetric Nanocapillary Interconnects . . . .</b>	<b>86</b>
3.1 Abstract . . . . .	86
3.2 Introduction . . . . .	87
3.3 Results and Discussion . . . . .	90
3.4 Conclusions . . . . .	94
3.5 Figures . . . . .	95
3.6 References . . . . .	102

<b>Chapter 4</b>	<b>Avalanche effects near nano-junctions . . . . .</b>	<b>103</b>
4.1	Abstract . . . . .	103
4.2	Introduction . . . . .	103
4.3	Theory . . . . .	105
4.4	Simulation details . . . . .	109
4.5	Results and Discussion . . . . .	110
4.6	Calculation of maximum Lyapunov exponent . . . . .	117
4.7	Conclusions . . . . .	121
4.8	Figures . . . . .	122
4.9	References . . . . .	129
<b>Chapter 5</b>	<b>Unraveling the physics of nonequilibrium 1/f dynamics in nano- porous membranes . . . . .</b>	<b>130</b>
5.1	Abstract . . . . .	130
5.2	Figures . . . . .	137
5.3	References . . . . .	141
<b>Chapter 6</b>	<b>Super large velocity in osmotic nano pumps . . . . .</b>	<b>142</b>
6.1	Abstract . . . . .	142
6.2	Introduction . . . . .	143
6.3	Theory . . . . .	145
6.4	Simulation details . . . . .	148
6.5	Results and Discussion . . . . .	149
6.6	Conclusions . . . . .	154
6.7	Figures . . . . .	155
6.8	References . . . . .	161
<b>Chapter 7</b>	<b>Conclusions . . . . .</b>	<b>162</b>

# Chapter 1

## Understanding anomalous current - voltage characteristics in microchannel nanochannel interconnect devices

### 1.1 Abstract

The integration of a microchannel with a nanochannel is known to exhibit anomalous nonlinear current–voltage characteristics. In this chapter, we perform detailed numerical simulations considering a 2–D nonlinear ion transport model, to capture and explain the underlying physics behind the limiting resistance and the overlimiting current regions, observed predominantly in a highly ion–selective nanochannel. We attribute the overlimiting current characteristics to the redistribution of the space charges resulting in an anomalous enhancement in the ionic concentration of the electrolyte in the induced space charge region, beyond a critical voltage. The overlimiting current with constant conductivity is predicted even without considering the effects of fluidic nonlinearities. We extend our study and report anomalous rectification effects, resulting in an enhancement of current in the non–ohmic region, under the application of combined AC and DC electric fields. The necessary criteria to observe these enhancements and some useful scaling relations are discussed.

### 1.2 Introduction

Owing to the advancements in micro–nano–manufacturing technology, there is a significant interest to investigate the transport phenomenon in channel sizes of the order of few hundreds of nanometers. Due to their large surface–area–to–volume ratio, the thickness of the electrical double layer (EDL) in these devices spans much of the channel height leading to the predominant transport of counterions in the channel. This enables the channel to be ion–selective[Qiao et

al.(2005)] and hence, can be used as an ion–exchange membrane. The transport in these devices is typically studied by connecting the nanochannel with two microchannels and a potential difference is applied between the ends of the microchannel[Jin et al.(2007), Mani et al.(2009), Postler et al.(2008) and Choi et al.]. The integration of a micro and a highly ion–selective nanochannel has paved way to many complex physics at the interfaces leading to anomalous effects in their transport.

Recent experiments by Kim et al.[Kim et al.(2007)]and by Yossifon and Chang et al.[Yossifon et al.(2008) and Chang et al.(2008)] revealed nonlinear current–voltage characteristics in a micro-nanochannel integrated system. The current characteristics were found to deviate from the classical diffusion–limited current transport theory, which predicts a saturation of the current density at higher applied voltages with an infinite differential resistance. Fig. 1.1 shows a schematic illustration of the nonlinear current–voltage characteristics in a highly ion–selective nanochannel integrated with a microchannel. At low electric fields, the current increases linearly with the applied voltage, following the Ohm’s law. This region is typically referred to as the Ohmic region or quasi–equilibrium region. However, beyond the first critical voltage ( $V_{LI}$ ), the current deviates from the Ohmic behavior, but continues to increase with a slope smaller than that of the Ohmic region. This region is often referred to as the limiting resistance region (LRR). Finally, beyond a second critical voltage ( $V_{LII}$ ), the slope of the current increases in comparison to the limiting regime and this region is typically referred to as the overlimiting current region.

Many plausible mechanisms are discussed to explain the overlimiting current characteristics [Rubinstein et al.(2009)]. Using a 1–D ideal ion–selective membrane model, Rubinstein [Rubinstein(1990)] suggested that the ionic concentration of the electrolyte doesn’t saturate to zero at the depletion membrane surface, as predicted by the diffusion–limited theory. Further, Staude et al.[Staude et al.(1988)] predicted a region of induced space charge (SCR) between the quasi-equilibrium EDL and the electroneutral diffusion boundary layer (DBL) at the depletion junction, resulting in a decrease in the length of the DBL. This decrease in DBL length was believed to result in the overlimiting current. They further proposed a possible mechanism to select the length of the SCR, by measuring the thickness of the vortex array, developed due to the instabilities in the space charge region. Yossifon et al.[Yossifon et al.(2008)], measured the vortex instability length from

their experiments and used it as a parameter in their model, to capture the overlimiting current region in their nanoporous membrane. However, an exact physical understanding of the large, yet finite differential resistance, in the limiting resistance region and the transition from the limiting to the overlimiting region is still unclear. A comprehensive physical model to discuss all the three I–V regions by considering the micro–nanochannel interconnect system is still missing. In this chapter, using a detailed 2–D nonlinear, nonideal ion–selective model, we capture and explain all the three regions, by analyzing the behavior of the ionic concentration, near the depletion junction of the micro–nanochannel. The model predicts a constant conductivity in the overlimiting current region, which is consistent with the experimental results.

With the understanding of the polarization physics at the junctions of the micro–nanochannel, we investigate the influence of small amplitude external AC perturbations along with the DC voltage, on the current characteristics, predominantly beyond the Ohmic region. The necessary criteria to observe the anomalous current rectification, resulting in an enhancement of current, under suitable AC field is discussed. Further, some useful scaling relations are presented. The anomalous transport characteristics may find applications in the field of water desalination, energy storage systems, protein separation and in the field of supercapacitors.

The rest of the chapter is outlined as follows. Section 1.3 discusses the nonlinear ion–transport model. The necessary simulation details are elucidated in section 1.4. A detailed discussion of the nonlinear current–voltage characteristics under the application of DC electric fields and under different EDL thickness is presented in section 1.5. In section 1.6, the anomalous rectification effect under combined AC/DC electric fields is discussed. A discussion on the calculation of first critical voltage is highlighted in section 1.7. Finally, conclusions are presented in section 1.8.

## **1.3 Theory**

### **1.3.1 Governing Equations**

In this section, the complete set of equations and the necessary boundary conditions to model the ion transport characteristics for a typical micro–nanochannel interconnect system (see Fig. 1.2) are

discussed. It has been shown that an accurate description of ion transport can be provided using the concepts of continuum theory for dimensions larger than several nanometers[Jin et al.(2007)]. Hence, continuum theory has been used in this chapter, as the smallest dimension considered is 30 *nm*. In this chapter, we consider a symmetric monovalent electrolyte like *KCl* with bulk concentration,  $c_0$ , and assume that the concentration of  $H^+$  and  $OH^-$  is much lower compared to the bulk concentration of the ionic species. Hence, the water dissociation effects are not considered in the numerical model[Jin et al.(2007)]. Further, we assume that the ions inside the Steric layer are rigidly held and do not contribute to the ionic current. We also neglect the Faradaic reactions that occur near the electrode in the present chapter. Under these assumptions, the total flux of the ionic species is contributed by a diffusive component resulting from the concentration gradient, an electrophoretic component arising due to the potential gradient and a convective component originating from the fluid flow. The total flux of each species in the solution is given by,

$$\mathbf{\Gamma}_i = -D_i \nabla c_i - \Omega_i z_i F c_i \nabla \phi + c_i \mathbf{u} \quad (1.1)$$

where  $\mathbf{\Gamma}_i$  is the flux vector,  $F$  is Faraday's constant,  $z_i$  is the valence,  $D_i$  is the diffusion coefficient,  $\Omega_i$  is the ionic mobility,  $c_i$  is the concentration of the  $i^{th}$  species,  $\mathbf{u}$  is the velocity vector of the fluid flow and  $\phi$  is the electrical potential. Note that the ionic mobility is related to the diffusion coefficient by Einstein's relation,  $\Omega_i = \frac{D_i}{RT}$ , where  $R$  is the ideal gas constant and  $T$  is the thermodynamic temperature. The mass transfer of each buffer species is given by,

$$\frac{\partial c_i}{\partial t} = -\nabla \cdot \mathbf{\Gamma}_i \quad (1.2)$$

The individual ionic current through the channel is calculated by integrating their respective fluxes over the cross-sectional area, i.e.,

$$\mathbf{I}_i = \int_S z_i F \mathbf{\Gamma}_i dS \quad (1.3)$$

and the total ionic current through the channel is calculated as,

$$\mathbf{I} = \int_S \sum_i z_i F \mathbf{\Gamma}_i dS \quad (1.4)$$

where  $S$  is the cross-sectional area of the channel. The electrical potential distribution is calculated by solving the Poisson equation,

$$\nabla \cdot (\epsilon_r \nabla \phi) = -\frac{\rho_e}{\epsilon_0} \quad (1.5)$$

where  $\epsilon_0$  is the permittivity of free space,  $\epsilon_r$  is the relative permittivity of the medium and  $\rho_e$  is the net space charge density of the ions defined as,

$$\rho_e = F \left( \sum_{i=1}^m z_i c_i \right) \quad (1.6)$$

where  $m$  is the total number of species considered in the system. Eq. (1.5), Eq. (1.2) and Eq. (1.1) are the classical Poisson–Nernst–Planck (PNP) equations, which describe the electrochemical transport. The incompressible Navier–Stokes and the continuity equations are considered, to describe the movement of the fluid flow,

$$\rho \left( \frac{\partial \mathbf{u}}{\partial t} + \mathbf{u} \cdot \nabla \mathbf{u} \right) = -\nabla p + \mu \nabla^2 \mathbf{u} + \rho_e \mathbf{E} \quad (1.7)$$

$$\nabla \cdot \mathbf{u} = 0 \quad (1.8)$$

where  $p$  is the pressure,  $\rho$  and  $\mu$  are the density and the viscosity of the fluid, respectively, and  $\mathbf{E} = -\nabla \phi$  is the electric field.  $\rho_e \mathbf{E}$  is the electrostatic body force acting on the fluid due to the space charge density and the applied electric field. The aforementioned set of coupled PNP and Navier–Stokes equations are also referred to as the space charge model.

We discuss the necessary boundary conditions for the closure of the problem. The normal flux of each ion is assumed to be zero on all the channel walls so that there is no leakage of current. The fluid velocity on the wall surfaces is assumed to be subjected to non-slip boundary condition and the gradients of pressure are assumed to be zero on the walls. Applying the charge conservation at the walls lead to the following electrostatic boundary condition,

$$\mathbf{n} \cdot \nabla \phi = \frac{\sigma}{\epsilon_0 \epsilon_r} \quad (1.9)$$

where  $\mathbf{n}$  denotes the unit normal vector (pointing outwards) to the wall surface and  $\sigma$  is the surface

charge density of the walls. We consider the microchannel on the right side, as the source and is given a positive voltage ( $\phi^{DC}$ ), while, the microchannel on the left is considered as the receiver and is grounded. The boundary conditions at the ends of the source (Eq. (1.10)) and receiver (Eq. (1.11)) microchannels are specified as:

$$\phi = \phi^{DC}, \quad c_i = c_o, \quad \mathbf{n} \cdot \nabla \mathbf{u} = 0, \quad p = 0 \quad (1.10)$$

$$\phi = 0, \quad c_i = c_o, \quad \mathbf{n} \cdot \nabla \mathbf{u} = 0, \quad p = 0 \quad (1.11)$$

All the equations are non-dimensionalized by scaling the distance with the length of the microchannel ( $L_m$ ), time with the diffusion time scale ( $L_m^2/D$ ), concentration with the bulk concentration of the electrolyte solution ( $c_0$ ), electric potential with  $\phi_0 = RT/Fz$ , fluid velocity with  $U_0 = \epsilon_0 \epsilon_r E_0 \phi_0 / \mu$ , where  $E_0$  is the average applied field in the system, pressure with  $p_0 = \mu U_0 / L_m$ , and space charge density with  $\rho_{e_0} = Fz c_0$ . We consider a symmetric monovalent electrolyte ( $z_+ = -z_- = z$ ) like *KCl* in the present analysis and normalize the diffusion coefficient of each ionic species with the characteristic diffusion coefficient,  $D = 2 \times 10^{-9} m^2/s$ . Applying these scaling variables, the system of governing equations in the dimensionless form can be written as:

Transport of positive ions,

$$\frac{\partial c_+^*}{\partial t^*} = D_+^* \nabla^{*2} c_+^* + D_+^* \nabla^* \cdot (c_+^* \nabla^* \phi^*) - Pe \nabla^* \cdot (c_+^* \mathbf{u}^*) \quad (1.12)$$

Transport of negative ions,

$$\frac{\partial c_-^*}{\partial t^*} = D_-^* \nabla^{*2} c_-^* - D_-^* \nabla^* \cdot (c_-^* \nabla^* \phi^*) - Pe \nabla^* \cdot (c_-^* \mathbf{u}^*) \quad (1.13)$$

Poisson equation for electrical potential,

$$\nabla^{*2} \phi^* = -\frac{1}{2\beta^2} \rho_e^* \quad (1.14)$$

Conservation of mass

$$\nabla^* \cdot \mathbf{u}^* = 0 \quad (1.15)$$

Conservation of momentum

$$\frac{1}{Sc} \frac{\partial \mathbf{u}^*}{\partial t^*} + Re \mathbf{u}^* \cdot \nabla^* \mathbf{u}^* = -\nabla^* p^* + \nabla^{*2} \mathbf{u}^* + \frac{1}{2\beta^2} \rho_e^* \mathbf{E}^* \quad (1.16)$$

In the above equations, variables with superscript  $'^*$  are the dimensionless variables. The various nondimensional numbers are given by,  $\beta = \lambda_D/L_m$ , Peclet number,  $Pe = L_m U_0/D$ , Reynolds number,  $Re = \rho U_0 L_m/\mu$ , and Schmidt number,  $Sc = \nu/D$  is the ratio of the kinematic viscosity ( $\nu = \mu/\rho$ ) to the ionic diffusion coefficient. The Debye length ( $\lambda_D$ ), determining the thickness of the EDL, is defined as,  $\lambda_D = \sqrt{\epsilon_0 \epsilon_r RT/2F^2 z^2 c_0}$ . In the present study, we understand the current–voltage characteristics for different values of  $\beta$ . Typically  $\beta$  varies in the range of  $10^{-3} - 10^{-5}$  [Yossifon et al.(2008)].

Using the aforementioned set of equations, analytical expressions are derived to calculate the magnitude of the normalized limiting current per unit width ( $I_L^* = |I_L/FzDc_0|$ ) and the corresponding normalized first critical voltage ( $V_{LI}^* = V_{LI}Fz/RT$ ). These expressions provide a quick understanding of the effect of the micro–nanochannel geometry and each system parameter on the emergence of nonlinear effects, i.e.,

$$I_L^* = \frac{2H_m}{L_m} \left( \frac{\hat{c}_{n+} + \hat{c}_{n-}}{\hat{c}_{n+} - \hat{c}_{n-}} \right) \quad (1.17)$$

$$V_{LI}^* = -I_L \left( \frac{L_n}{FzDH_n(\hat{c}_{n+} + \hat{c}_{n-})} \right) + \ln \left( \frac{\hat{c}_+|_{x=x_{e-}}}{\hat{c}_+|_{x=x_{e+}}} \right) - I_L \left( \frac{L_m}{FzDH_m c_0} \right) \quad (1.18)$$

where  $\hat{c}_{n+}$  and  $\hat{c}_{n-}$  are the counter–ion and co–ion concentration inside the nanochannel (averaged over the height of the nanochannel,  $H_n$ ).  $\hat{c}_+|_{x=x_{e-}}$  and  $\hat{c}_+|_{x=x_{e+}}$  are the cation concentration (averaged over the channel height) at the left and right end of the anodic micro–nanochannel

interface, respectively (see Fig. 1.14 and section 1.7 for details).  $L_n$  and  $H_m$  are the nanochannel length and microchannel height, respectively. It can be observed from Eq. (1.17) that, in the case of an ideal cation-selective membrane, ( $\hat{c}_{n-} = 0$ ), we obtain the classical asymptotic limit given by the diffusion-limited theory,  $I_L^*|_{ideal} = \frac{2H_m}{L_m}$ , for a symmetric monovalent electrolyte.

## 1.4 Simulation Details

The simulated domain consists of a rectangular nanochannel of length  $5 \mu m$  ( $L_n$ ) and height  $30 nm$  ( $H_n$ ) connected to two microchannels of length  $6 \mu m$  ( $L_m$ ) and height  $1 \mu m$  ( $H_m$ ), on either side of the nanochannel (see Fig. 1.2). A 2-D simulation study is carried out by assuming that the depth (perpendicular to the plane of the paper) of the micro and nanochannel to be much larger than the length. The thermodynamic temperature is  $T = 300 K$ , the density and the viscosity of the fluid are  $1000 kg/m^3$  and  $1.003 \times 10^{-3} Pa \cdot s$ , respectively. The diffusivities of  $K^+$  and  $Cl^-$  are  $1.96 \times 10^{-9} m^2/s$  and  $2.03 \times 10^{-9} m^2/s$ , respectively. We assume the dielectric constant of the aqueous solution to be,  $\epsilon_r = 80$ [Hille(2001)]. Further, we also assume the surface charge on the walls of the microchannel,  $\sigma_m = 0$  and on nanochannel,  $\sigma_n = -1 mC/m^2$ , respectively.

The coupled PNP and Navier-Stokes equations are numerically solved using the finite volume method in OpenFOAM[<http://www.openfoam.com/>(2011)](Open Field Operation and Manipulation). The convective terms in the PNP equations are discretized using second-order bounded NVD schemes[Toro(1999)] and all the Laplacian terms are discretized using second-order central differencing scheme. SIMPLE algorithm is used for pressure-velocity coupling. Second-order implicit time differencing scheme is used to discretize the variables in time. A finer mesh is introduced near the walls, at the entrance and exit of the nanochannel. The model is validated with the numerical results of Daiguji and Jin et al.[Jin et al.(2007)]. Furthermore, the results reported here are ensured to be independent of the grid size.

## 1.5 Results and Discussion

### 1.5.1 Nonlinear current–voltage characteristics

We initially consider low bulk ionic concentration,  $c_0 = 0.1 \text{ mM}$  (corresponding to a thick EDL regime,  $\beta = 0.0051$ ) to investigate the current–voltage characteristics. The nanochannel ion-selectivity can be modulated by controlling the bulk ionic concentration (in other words controlling  $\lambda_D$ ) and also by controlling the nanochannel wall surface charge density. In this study, we use the former approach to control the ion–selectivity and the study can easily be extended to understand the surface charge effects. Fig. 1.3 shows the magnitude of the normalized current as a function of the normalized voltage which reveals all the three regions, namely Ohmic region, limiting resistance region (LRR) and the overlimiting region. In this section, we will briefly discuss the first two regions. In the Ohmic/quasi–equilibrium region, the current is found to vary linearly with the applied voltage. With increase in the voltage, the current deviates from the Ohmic behavior as shown in the inset of Fig. 1.3. The normalized value of  $I_L$  (in magnitude) and the first critical voltage,  $V_{LI}$  are found to be 0.3175 and 13.5394, respectively. The corresponding analytical values (using Eq. (1.17) and Eq. (1.18)) are 0.347 and 13.8205, respectively. The analytical expressions provide a reasonable degree of accuracy in comparison to the numerical solutions. Fig. 1.3 also reveals that the current beyond the first critical voltage, does not saturate as predicted by the classical diffusion–limited theory, but increases with a slope smaller than that of the Ohmic region. All these results are consistent with the experiments of Yossifon et al.[Yossifon et al.(2008)] and Kim et al.[Kim et al.(2007)] for a micro-nanochannel system.

An exact reason for the large, yet finite differential resistance in the limiting resistance region is yet to be understood in these systems[Yossifon et al.(2008)]. In order to understand this, we investigate the ionic concentration distribution along the axial direction in the Ohmic region and in the LRR. Fig. 1.4(a) shows that, for DC voltage ( $\phi^{DC} Fz/RT = 7.7367$ ), corresponding to the Ohmic region, due to the concentration polarization effects, there is a depletion of ions in the anodic region and an enrichment of ions in the cathodic region. This results in a linear concentration gradient from the end of the microchannel (where the concentration of the ionic solution

is the bulk ionic concentration) until the regions close to the micro–nanochannel interface. We also observe that, local electroneutrality is maintained in the regions of linear concentration gradient, with no additional space charges. Typically, these regions are referred to as the diffusion boundary layer (DBL) regions[Rubinstein(1990)]. It is also observed that the linear concentration gradient in the DBL regions becomes steeper with the increase in the voltage. Further, we observe a thin quasi–equilibrium EDL region at the micro/nanochannel depletion interface (see inset of Fig. 1.4(a)). Similarly, we also observe a thin quasi–equilibrium EDL region at the micro/nanochannel enrichment interface. Furthermore, Fig. 1.4(a) reveals that, in the Ohmic region, the location of the minimum anion concentration is inside the nanochannel. The minimum anion concentration along the axial direction is observed at  $x/L_m = 1.8267$ .

Fig. 1.4(b) shows that, for DC voltage ( $\phi^{DC} Fz/RT = 77.3677$ ), corresponding to the limiting resistance region, the ionic concentration at the depletion micro/nanochannel interface does not saturate to zero as predicted by the classical diffusion–limited theory. Further, a region of space charge is induced between the quasi–equilibrium EDL at the micro–nanochannel depletion interface and the local electroneutral diffusion boundary layer. The induced space charge region results in a nonlinear concentration distribution near the depletion interface (see inset of Fig. 1.4(b)). Further, we observe that, beyond the first critical voltage, the location of the minimum anion concentration shifts from the nanochannel region towards the microchannel interface region. The new location of the minimum anion concentration along the axial direction is observed at  $x/L_m = 1.8375$  which is outside the nanochannel. It is also found that, the new position of the minimum anion concentration does not change beyond the first critical voltage. In spite of the changes in the concentration near the depletion junction, we observe that a linear concentration gradient and local electroneutrality is always maintained in the cathodic enrichment region.

Fig. 1.5 shows the resistance of each channel as a function of DC voltage. The normalized resistance in each channel is numerically determined by calculating the normalized voltage drop across each channel and dividing it with the magnitude of the normalized current. It can be observed that, in the Ohmic region, the nanochannel has a constant finite conductance, and hence should be considered, in understanding the current characteristics in such interconnect systems unlike most of the earlier theories discussed in the literature[Rubinstein(1990)]. The large nanochannel resistance

can be understood from the fact that, most of the voltage drop occurs inside the nanochannel in the Ohmic region. Further, the inset of Fig. 1.5 shows that the resistance of the depletion microchannel is relatively smaller compared to the nanochannel resistance. This is because we observe that the microchannel is still electroneutral, even though there is a depletion of ions. Furthermore, in the enrichment microchannel, as the concentration of the ionic species is greater than the bulk ionic concentration, the resistance of this microchannel is minimal.

In the limiting resistance region (LRR), Fig. 1.5 reveals that, there is a gradual increase in the resistance of the depletion microchannel and it starts becoming comparable to the nanochannel resistance as the voltage increases. This is due to the formation of the induced space charges near the depletion micro/nanochannel interface resulting in an increase in the electric field at this interface. Hence, beyond the Ohmic region, the resistances of both the nanochannel and the depletion microchannel are important. Furthermore, we note that the induced space charge is accompanied by a shift in the location of the minimum anion concentration towards the microchannel interface. Fig. 1.6(a) and Fig. 1.6(b) reveal the normalized ionic concentration along the axial direction for various DC electric fields ( $\phi^{DC} Fz/RT = 77.3677$ ,  $\phi^{DC} Fz/RT = 116.0516$ ,  $\phi^{DC} Fz/RT = 232.1032$ ,  $\phi^{DC} Fz/RT = 773.6773$ ), beyond the first critical voltage. It can be observed that, until the second critical voltage, the charges propagate predominantly towards the anodic end of the microchannel. This is accompanied by a monotonic decrease in the minimum anion concentration as shown in Fig. 1.7.

We believe that the predominant propagation of charges towards the microchannel along with the decrease in the minimum anion concentration until the second critical voltage, results in a finite differential resistance. Hence, we observe a change in the slope of the I–V curve, leading to the limiting resistance region. The anomalous increase in the minimum anion concentration beyond the second critical voltage (see Fig. 1.7) leading to the overlimiting current would be discussed in the next section.

## 1.5.2 Overlimiting current characteristics

Fig. 1.8 shows that beyond a second critical voltage ( $V_{LII}^* = 154.7355$ ), the slope of the I–V curve increases from that of the limiting region leading to the overlimiting current region. Fig. 1.6(a) and Fig. 1.6(b) show that, beyond the second critical voltage, the space charges formed near the depletion junction propagate inside the nanochannel (solid arrow indicates the propagation of charges inside the nanochannel) along with its propagation towards the anodic end of the microchannel. Such propagation of space charges under large DC electric fields can be captured only by considering the entire micro–nanochannel interconnect system. The propagation leads to a redistribution of space charge near the depletion interface, resulting in an increase in the concentration of the ions near this interface as shown in Fig. 1.6(a) and Fig. 1.6(b). Further, we observe that the increase in the concentration is more pronounced in the case of anions (co–ion) compared to that of the cation (counter–ion) concentration. Furthermore, the propagation of charges towards the nanochannel interface, results in a significantly higher electric field inside the nanochannel interface beyond the second critical voltage. These effects result in a shift in the slope of the overall system resistance beyond the second critical voltage (see Fig. 1.5), leading to an overlimiting current region. We note that, by investigating the behavior of the minimum anion concentration alone, we can capture all the three regions of the I–V characteristics.

We would also like to highlight that, all the three regions of the I–V curve can be captured and explained even without considering the fluid flow equations in the model (see Fig. 1.3). This suggests that the fluidic nonlinearities observed in the space charge region may not necessarily contribute towards understanding the origin of the overlimiting current. Fig. 1.3 also shows the current characteristics at high concentration limit,  $c_0 = 5 \text{ mM}$ , corresponding to thin EDL regime ( $\beta = 7.2605 \times 10^{-4}$ ). Under thin EDL limit, the ion–selectivity of the nanochannel decreases significantly and we do not observe the space charges at the depletion region. Hence, we observe only Ohmic region in the current–voltage characteristics. Thus, the ion–selectivity of the nanochannel plays a prominent role in order to observe all the three regions of the I–V curve.

## 1.6 Anomalous current rectification under combined AC/DC electric fields

We extend our study to investigate the influence of small amplitude external AC perturbations along with the DC voltage, on the current characteristics. Note that the application of a large AC amplitude leads to higher complexities in the system, which is beyond the scope of the present work. In order to understand the AC effects, we solve the same set of governing equations with the necessary boundary conditions discussed in section 1.3. The only variation is the boundary condition for the potential at the source microchannel,

$$\phi = \phi^{DC} + \phi^{AC} \sin(\omega t) \quad (1.19)$$

where  $\phi^{AC}$  is the amplitude of the AC electric potential and  $\omega$  is the angular frequency ( $\omega = 2\pi f$ ,  $f$  is the applied frequency). An AC voltage is applied after the system reaches a steady-state with the DC field. We consider the same system parameters as discussed before and initially investigate the effect of combined AC/DC electric fields under thick EDL limit ( $\beta = 0.0051$ ). We understand the frequency effects using the dimensionless frequency ( $fL_m^2/D$ ) and consider the ratio of AC amplitude to DC voltage ( $\alpha = \phi^{AC}/\phi^{DC}$ ), to investigate the amplitude effects. Further, the effect of the combined AC/DC electric field on the current characteristics is investigated by time averaging the current (per unit width) measured at the end of the source microchannel over one time period:

$$\langle \mathbf{I} \rangle = \frac{1}{T_p} \int_0^{T_p} \mathbf{I} dt \quad (1.20)$$

where  $T_p$  is the time period of one cycle. In Fig. 1.9, we present the relative current rectification as a function of the dimensionless frequency ( $fL_m^2/D$ ) for various DC voltages. To understand the frequency effects,  $\alpha$  ( $= 1.333$ ) is kept constant. The relative current rectification is calculated as:

$$\frac{\Delta \mathbf{I}}{\mathbf{I}_{DC}} = \frac{\langle \mathbf{I} \rangle - \mathbf{I}_{DC}}{\mathbf{I}_{DC}} \quad (1.21)$$

where  $\mathbf{I}_{DC}$  is the current (per unit width) obtained when only DC voltage is applied and  $\langle \mathbf{I} \rangle$  is the time averaged current (per unit width) under combined AC/DC electric field computed using Eq. (1.20). It can be observed that for a given DC voltage of  $\phi^{DC} Fz/RT = 77.3677$ , at a low frequency, ( $fL_m^2/D = 90$ ), there is no significant current rectification. However, with increase in the frequency, positive rectification effects are observed with enhancements in the current. A maximum positive current rectification is observed at  $fL_m^2/D = 540$ , while a further increase in the frequency leads to a decrease in the rectification effects. Furthermore, at a very high frequency ( $fL_m^2/D = 4500$ ), no current rectification is observed. Similar anomalous rectification effects were also observed in the experiments of Rubinstein et al. [Rubinstein(1990)] for simple cation–selective ion exchange membranes. Fig. 1.9 also shows that as the DC voltage increases and under same  $\alpha$ , the rectification effects increase. Furthermore, we observe that, for a given system, the frequency at which the maximum positive rectification occurs is independent of the applied DC voltage, provided the voltage is beyond the first critical voltage.

In order to understand the current rectification, we consider a 1- $D$  Nernst–Planck (NP) model and investigate the current (per unit width) in the induced space charge region using Eq. (1.1) and Eq. (1.4). Neglecting the contributions of diffusive and convective flux in the induced space charge region, and assuming a symmetric monovalent electrolyte with equal diffusivities ( $D_+ = D_- = D$ ), we obtain the following expression for the total current per unit width,

$$I = -\frac{F^2 z^2 D H_m}{RT} \frac{d\hat{\phi}}{dx} (\hat{c}_+ + \hat{c}_-) \quad (1.22)$$

where  $\hat{\cdot}$  denotes the area averaged quantity considering the width of the system to be unity. Under the application of combined AC and DC field, we assume,  $(\hat{c}_+ + \hat{c}_-) = C_0 + C_1 \cos(\omega t + \theta_1)$  and  $\frac{d\hat{\phi}}{dx} = \phi_{x_0} + \phi_{x_1} \cos(\omega t + \phi_1)$ , neglecting the contribution of other higher harmonic components.  $C_0, \phi_{x_0}$  are the DC component of the total ionic concentration and the field, respectively.  $C_1, \phi_{x_1}$  are the respective first harmonic contributions of the ionic concentration and field.  $\theta_1$  and  $\phi_1$  are the corresponding phase angles of the former and latter terms, respectively. Substituting the aforementioned expressions into Eq. (1.20) and averaging over one time period ( $T_p$ ), the time

averaged current per unit width  $\langle I \rangle$  due to the combined AC and DC electric field is calculated as,

$$\langle I \rangle = I_{DC} - \frac{F^2 z^2 D H_m C_1 \phi_{x1}}{RT} \cos(\theta_1 - \phi_1) \quad (1.23)$$

where  $I_{DC} = -\frac{F^2 z^2 D H_m}{RT} (C_0 \phi_{x0})$  is the DC component of the current per unit width. To explain the current rectification under different excitation frequencies, the normalized first harmonic contribution of the total concentration and field, ( $C_1^* \phi_{x1}^* = C_1 \phi_{x1} L_m / c_0 \phi_0$ ), and their relative phase difference ( $\theta_1 - \phi_1$ ) is numerically calculated in the induced space charge region at  $x/L_m = 2$ , for a given DC voltage of  $\phi^{DC} Fz/RT = 154.7354$ . The results are shown in Fig. 1.10. It can be observed that for low frequency, inspite of large contribution of the harmonic terms, we do not observe significant rectification as the electric field and the ionic concentration tend to be out of phase with each other ( $\theta_1 - \phi_1 \simeq 90^\circ$ ) as shown in the inset of Fig. 1.10. While, at a very high frequency ( $fL_m^2/D = 4500$ ), we observe minimal contribution from the harmonic terms ( $C_1^* \phi_{x1}^* \simeq 0$ ) (see Fig. 1.10), and hence observe minimal rectification. However, at moderate excitation frequencies, we observe an appreciable contribution of the ionic concentration and the electric field. Also at these frequencies the relative phase difference between the concentration,  $C_1^*$  and field,  $\phi_{x1}^*$  decreases which implies that they gradually tend to become in-phase with each other as shown in the inset of Fig. 1.10. The above two effects together result in a positive current rectification and a maximum rectification is observed at  $fL_m^2/D = 540$ . These arguments also help us to conclude that the current rectification can be understood without considering the effects of fluidic nonlinearities observed in the induced space charge region of micro/nanochannel as we have neglected the convective flux contribution in the  $1 - D$  NP model. Similar physics is also observed at other DC voltages, beyond the first critical voltage. Furthermore, from our NP model we would like to comment that it is also possible to suppress the current and achieve negative rectification under combined AC/DC electric field when  $fL_m^2/D \leq 1$ , as the relative phase difference between the concentration and field ( $\theta_1 - \phi_1$ ) can be greater than  $90^\circ$ .

Fig. 1.9 also shows that, when the DC voltage is in the Ohmic regime ( $\phi^{DC} Fz/RT = 7.7367$ ), i.e., when there are no induced space charges near the depletion micro-nanochannel interface, no change in the time averaged current is observed at any frequency, under same  $\alpha$ . These results are

observed due to the minimal contribution of the harmonic terms ( $C_1\phi_{x1}$ ) to the DC current. Thus, the application of combined AC/DC electric fields offer a means to control the current beyond the Ohmic region. Further, the combined AC/DC electric field can also be potentially used to understand and measure the induced space charge region developed at the depletion micro/nanochannel interface. Fig. 1.11 displays the relative current rectification as a function of  $\alpha$ . To understand the amplitude effects, the frequency ( $fL_m^2/D = 450$ ) and DC voltage,  $\phi^{DC}Fz/RT = 154.7354$  are kept constant. It is observed that, the relative rectification shows a quadratic scaling with  $\alpha$ .

### 1.6.1 EDL effects on AC current rectification

In this section, we understand the AC current rectification for different EDL thickness,  $\beta = \lambda_D/L_m$ .  $\beta$  is varied by changing the bulk ionic concentration ( $c_0$ ) of the electrolyte. The bulk ionic concentrations chosen are summarized in Table 1.1. Note that a similar range of low ionic concentrations are used even in experiments on highly ion-selective nanochannels[Yossifon et al.(2008)].

For each concentration, different AC frequencies are applied systematically to understand the current rectification. Fig. 1.12 shows the dimensionless frequency, at which the current rectification is maximum, as a function of  $\beta$  at a constant amplitude ( $\alpha = 1.333$ ) and DC voltage,  $\phi^{DC}Fz/RT = 154.7354$ . The applied DC voltage is ensured to be greater than the first critical voltage,  $V_{LI}$ , for all the concentration cases chosen. We observe that the dimensionless frequency approximately scales inversely with  $\beta$ .

Fig. 1.13 shows the AC current rectification as a function of dimensionless frequency, under two different EDL limits,  $\beta = 0.0051$ , corresponding to thick EDL region (when the nanochannel is highly ion-selective) and  $\beta = 7.2605 \times 10^{-4}$ , corresponding to thin EDL limit, i.e., when the ion-selectivity of the nanochannel is significantly reduced. Here amplitude ( $\alpha = 1.333$ ) and DC voltage,  $\phi^{DC}Fz/RT = 154.7354$  are kept constant. Under thin EDL limit, minimal current rectification is observed, as the induced space charge region is not developed at the depletion micro-nanochannel interface. As discussed in section 1.5, we observe only the Ohmic region in the absence of induced space charge region (see Fig. 1.2). The minimal current rectification at thin EDL limit further reveals the criteria to establish positive current rectification phenomenon.

A discussion on the mathematical framework for the calculation of critical voltage to corroborate limiting resistance regime is highlighted in section 1.7.

## 1.7 Derivation of limiting current and first critical voltage

We use an approach similar to Yossifon et al.[Yossifon et al.(2008)] to calculate the limiting current,  $I_L$  per unit width. Using a  $1 - D$  model, and assuming a symmetric monovalent electrolyte, with equal diffusivities ( $D_+ = D_- = D$ ) and neglecting the convective flux, the flux of each ion in the  $x$ -direction can be calculated from Eq. (1.1)

$$\hat{\Gamma}_{\pm}(x) = -D \frac{d\hat{c}_{\pm}}{dx} \mp \frac{zFD}{RT} \hat{c}_{\pm} \frac{d\hat{\phi}}{dx} \quad (1.24)$$

where  $\hat{\cdot}$  denotes the area averaged quantity considering the width of the system to be unity. As it is observed that, until the first critical voltage, local electroneutrality is observed near both the anodic and the cathodic microchannel region ( $\hat{c}_+ = \hat{c}_- = \hat{c}$ ), with linear concentration gradients observed at these regions,  $\frac{d\hat{c}_+}{dx} = \frac{d\hat{c}_-}{dx} = \frac{d\hat{c}}{dx}$ , the concentration gradient outside the nanochannel,

$$\frac{d\hat{c}}{dx} = -\frac{\hat{\Gamma}_+ + \hat{\Gamma}_-}{2D} \quad (1.25)$$

We neglect the concentration distribution in the quasi-equilibrium EDL region near the micro-nanochannel interface and consider the concentration of the ions to be zero at the interface of the micro-nanochannel (similar to the analogy of Levich's limiting-current density). Further, it is known that the concentration at the end of the source microchannel is equal to the bulk ionic concentration of the solution. Under these assumptions,

$$\hat{\Gamma}_+ + \hat{\Gamma}_- = -\frac{2Dc_0}{L_m} \quad (1.26)$$

where  $L_m$  is the length of the microchannel (can also be taken to be equal to the length of the diffusion boundary layer). Considering  $\bar{\Gamma} = -\frac{\hat{\Gamma}_+}{\hat{\Gamma}_-}$  to be the ratio of counter-ion and co-ion fluxes, we obtain the following expression for the limiting current density,  $i_L = (\hat{\Gamma}_+ - \hat{\Gamma}_-) Fz$ ,

$$i_L = -\frac{2Dc_0Fz}{L_m} \left( \frac{\bar{\Gamma} + 1}{\bar{\Gamma} - 1} \right) \quad (1.27)$$

It can be easily shown that,  $\bar{\Gamma} = \frac{\hat{c}_{n+}}{\hat{c}_{n-}}$  [Yossifon et al.(2008)], where  $\hat{c}_{n+}$  and  $\hat{c}_{n-}$  are the counter-ion and co-ion concentrations inside the nanochannel (averaged over the height of the nanochannel). The individual ionic concentrations inside the nanochannel can be approximately calculated using the Donnan equilibrium theory [Schoch et al.(2008)]

$$\hat{c}_{n\pm} = \pm \frac{\bar{c}}{2} + \sqrt{\left(\frac{\bar{c}}{2}\right)^2 + c_0^2} \quad (1.28)$$

where  $\bar{c} = \hat{c}_{n+} - \hat{c}_{n-} = -\frac{2\sigma_n}{FzH_n}$ , is obtained from the electroneutrality condition inside the nanochannel. Substituting Eq. (1.28) and the aforementioned conditions into Eq. (1.27), we obtain the magnitude of the normalized limiting current ( $I_L^* = |I_L/FzDc_0|$ ) per unit width at the end of the microchannel,

$$I_L^* = \frac{2H_m}{L_m} \left( \frac{\hat{c}_{n+} + \hat{c}_{n-}}{\hat{c}_{n+} - \hat{c}_{n-}} \right) \quad (1.29)$$

Using the limiting current expression, we now derive an expression to calculate the first critical voltage ( $V_{LI}$ ), by considering the resistances of both nanochannel and microchannel, as both the resistances play an important role when the current deviates from the Ohmic region. We assume no significant voltage drop in the enrichment receiver microchannel and consider a linear voltage drop along the nanochannel and also along the depletion source microchannel. Under these assumptions, we first focus on calculating the voltage at the end of the nanochannel. Using Eq. (1.24) and Eq. (1.29), and neglecting the diffusional flux, the limiting current (per unit width) along the  $x$ -direction for a symmetric monovalent electrolyte, with equal diffusivities relates to,

$$I_L = -\frac{F^2z^2DH_n}{RT} \frac{d\hat{\phi}}{dx} (\hat{c}_{n+} + \hat{c}_{n-}) \quad (1.30)$$

Integrating both sides along the length of the nanochannel (from  $x = x_s$  to  $x = x_e$ , where  $x_s$  is the coordinate where the nanochannel starts and  $x_e$  is the coordinate where the nanochannel ends) and substituting Eq. (1.28), we obtain an expression for the voltage at the end of the nanochannel (averaged over the nanochannel height) as,

$$\hat{\phi}_N = -I_L \left( \frac{RTL_n}{F^2 z^2 DH_n (\hat{c}_{n+} + \hat{c}_{n-})} \right) \quad (1.31)$$

We calculate the voltage at the end of the source microchannel, which is the desired first critical voltage ( $V_{LI}$ ), by considering a linear voltage drop in the anodic depletion microchannel. Following the above procedure, and assuming,  $\frac{d\hat{c}_+}{dx} = \frac{d\hat{c}_-}{dx} = \frac{d\hat{c}}{dx}$ , the limiting current per unit width in the anodic microchannel can be written as,

$$I_L = -\frac{F^2 z^2 DH_m}{RT} \frac{d\hat{\phi}}{dx} (\hat{c}_+ + \hat{c}_-) \quad (1.32)$$

It is important to note that, the ion concentration varies linearly in the microchannel unlike the ionic concentration inside the nanochannel. Upon integrating the limiting current along the anodic microchannel and assuming the concentration of the ions to be zero at the anodic nanochannel–microchannel interface along with the aforementioned conditions

$$V_{LI} = \hat{\phi}_N - I_L \left( \frac{RTL_m}{F^2 z^2 DH_m c_0} \right) \quad (1.33)$$

where  $\hat{\phi}_N$  is the voltage (averaged over the nanochannel height) at the end of the nanochannel given by Eq. (1.33). Substituting the dimensions of the geometry and all the system parameters used in the present simulation study, the magnitude of the normalized limiting current per unit width is 0.347 while the numerical solution is 0.3175. Further, the normalized first critical voltage, ( $V_{LI}^* = V_{LI} Fz/RT$ ) is 10.1225 and the numerical solution is 13.5394. The analytical expression slightly under predicts the first critical voltage. This is because, we assumed that the concentration of the ions is zero at the anodic micro–nanochannel interface. However, it is known from the detailed numerical simulations, that there is a non–zero ionic concentration at this interface resulting in an interfacial jump in the potential. This jump in the potential can be obtained using the Donnan

theory[Schoch et al.(2008)], by equating the chemical potential at this interface, provided the ionic concentration at this interface is known.

$$\hat{\phi}_N|_{x=x_{e+}} - \hat{\phi}_N|_{x=x_{e-}} = \frac{RT}{zF} \ln \left( \frac{\hat{c}_+|_{x=x_{e-}}}{\hat{c}_+|_{x=x_{e+}}} \right) \quad (1.34)$$

where  $\hat{\phi}_N|_{x=x_{e-}} (= \hat{\phi}_N)$  and  $\hat{c}_+|_{x=x_{e-}} (= \hat{c}_{n+})$  are the potential and cation concentration at the left end of the anodic micro–nanochannel interface (see Fig. 1.14), which can be obtained using Eq. (1.34), and Eq. (1.28), respectively. Knowing the cation concentration at the right end of the micro–nanochannel interface,  $\hat{c}_+|_{x=x_{e+}}$ , we obtain a modified expression for the first critical voltage.

$$V_{LI}|_{modified} = \hat{\phi}_N + \frac{RT}{zF} \ln \left( \frac{\hat{c}_+|_{x=x_{e-}}}{\hat{c}_+|_{x=x_{e+}}} \right) - I_L \left( \frac{RTL_m}{F^2 z^2 D H_m c_0} \right) \quad (1.35)$$

Note, the interfacial potential jump can also be obtained using the anion concentration at this interface by following the similar procedure. Upon substituting for  $\hat{c}_+|_{x=x_{e+}}$  from our numerical simulation, the modified normalized first critical voltage is found to be 13.8205 which compares reasonably well to the numerical simulation value.

## 1.8 Conclusions

Using a detailed 2–D nonlinear ion transport model, the large yet finite differential resistance in the limiting resistance region, and the transition to the overlimiting current region are explained. The regions are distinguished by analyzing the propagation of space charges and the behavior of the ionic concentration in the induced space charge region, developed at the depletion micro–nanochannel junction. The overlimiting current is predicted even without considering the effects of fluidic nonlinearities near the depletion junction. Furthermore, anomalous current rectification, resulting in an enhancement of the current, under combined AC/DC electric field is discussed. The necessary criteria to observe these rectification effects and some useful scaling relations are presented. We believe, the application of combined AC/DC electric field can offer a control on the current in the limiting resistance region, and can also be potentially used to understand and measure the space charge region, induced near the depletion micro–nanochannel interface. The anomalous current

characteristics may also find applications in the field of energy storage systems, supercapacitors, water desalination and selective species separation.

## 1.9 Tables

Table 1.1: Bulk concentration ( $c_0$ ) and corresponding dimensionless EDL thickness

$c_0$ ( $mM$ )	$\lambda_D$ ( $nm$ )	$\beta$ ( $\times 10^{-3}$ )
0.06	39.768	6.628
0.1	30.804	5.134
0.2	21.782	3.630
0.333	16.880	2.813

## 1.10 Figures

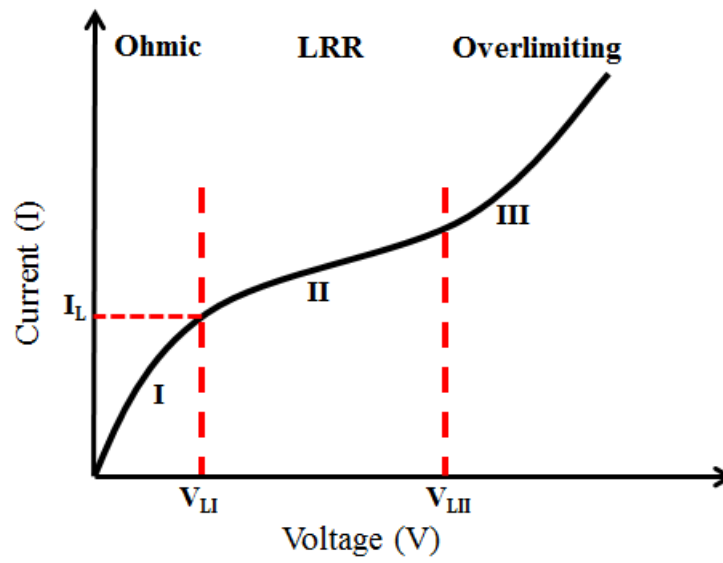


Figure 1.1: Schematic illustration of nonlinear current–voltage characteristics of a typical ion–selective nanochannel integrated with a microchannel. LRR represents limiting resistance region.

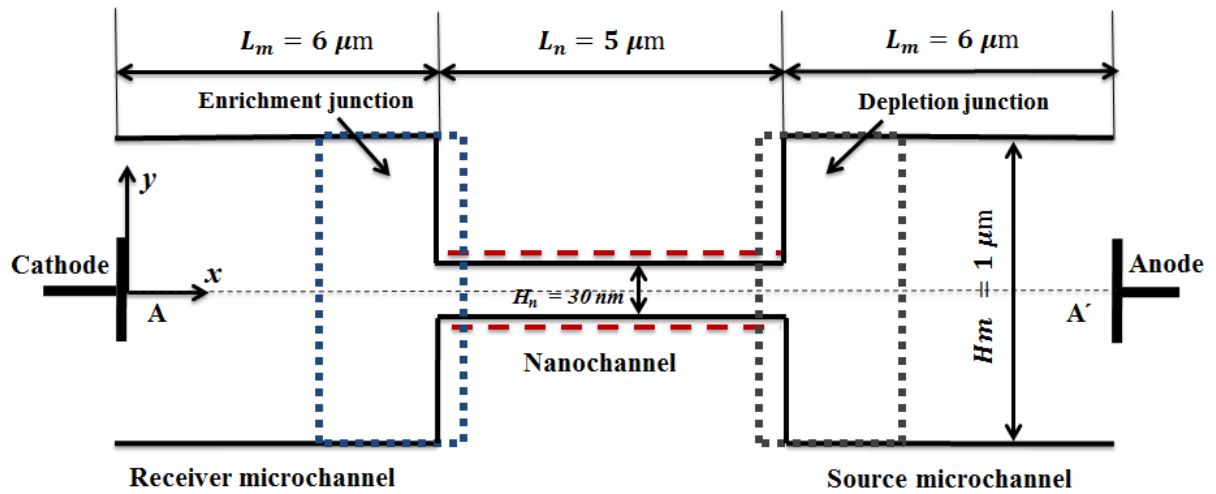


Figure 1.2: Simulation set-up (not drawn to scale), consisting of a negatively charged nanochannel connected to two microchannels.

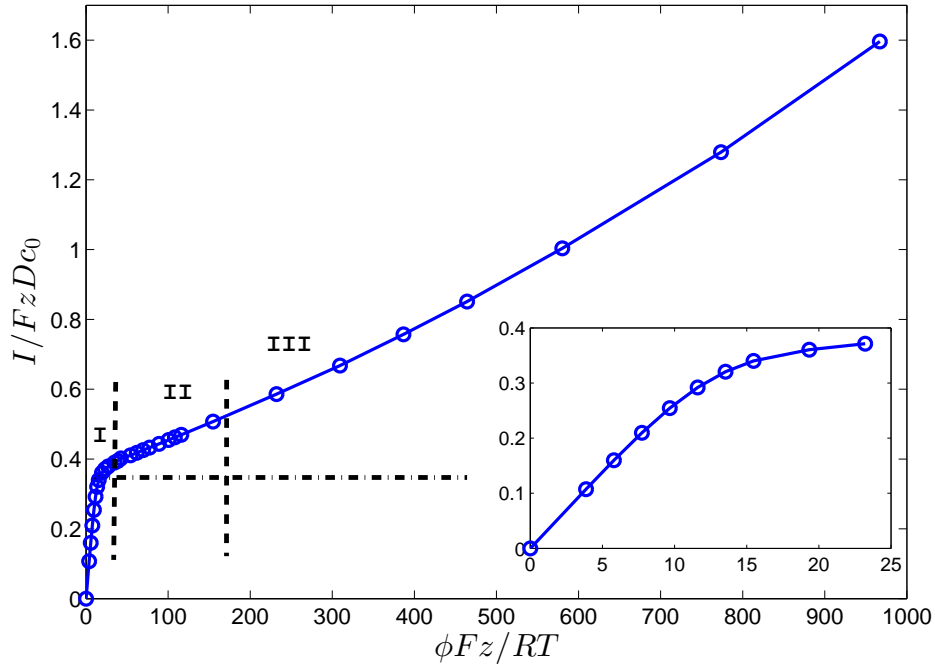
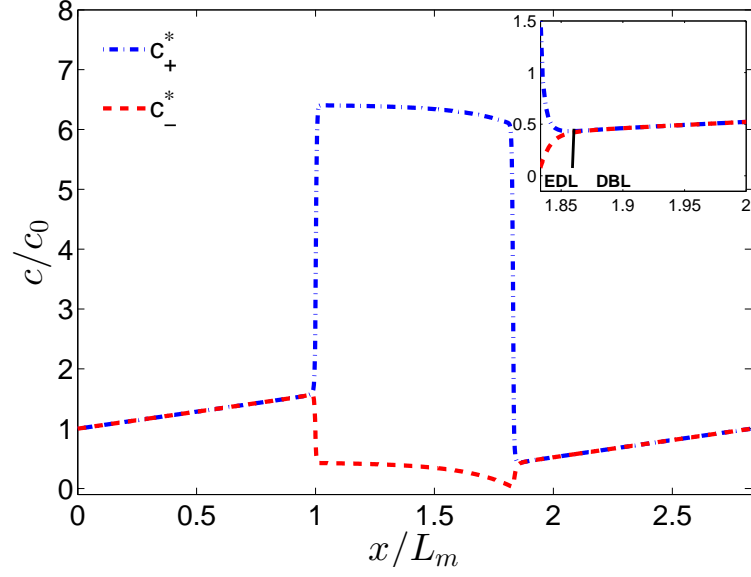
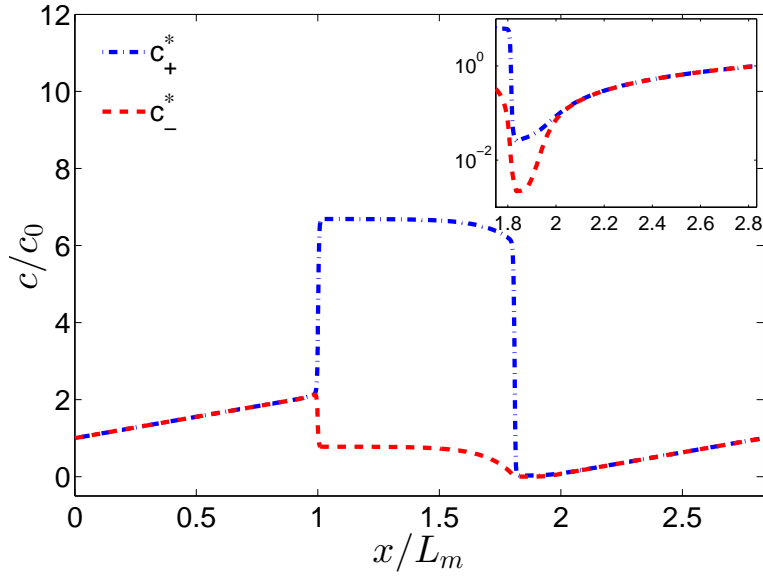


Figure 1.3: Normalized current–voltage characteristics (in magnitude) of a cation–selective nanochannel connected to two microchannels. The dashed dotted line shows the analytical value of the limiting current. Region I corresponds to the Ohmic region, II represents the limiting resistance region (LRR) and region III corresponds to the overlimiting region. The inset of the figure displays the transition from the Ohmic region to the limiting resistance region.



(a)



(b)

Figure 1.4: (a) Normalized ionic concentration along the axial direction, for  $\phi^{DC} Fz/RT = 7.7367$ , corresponding to the Ohmic region. The inset of the figure shows the thin quasi-equilibrium EDL region at the depletion micro/nanochannel interface. (b) Normalized ionic concentration along the axial direction, for  $\phi^{DC} Fz/RT = 77.3677$ , corresponding to the limiting resistance region. The inset of the figure shows the nonlinear concentration distribution due to the presence of induced space charges near the micro-nanochannel depletion interface. In all these cases  $\beta = 0.0051$ .

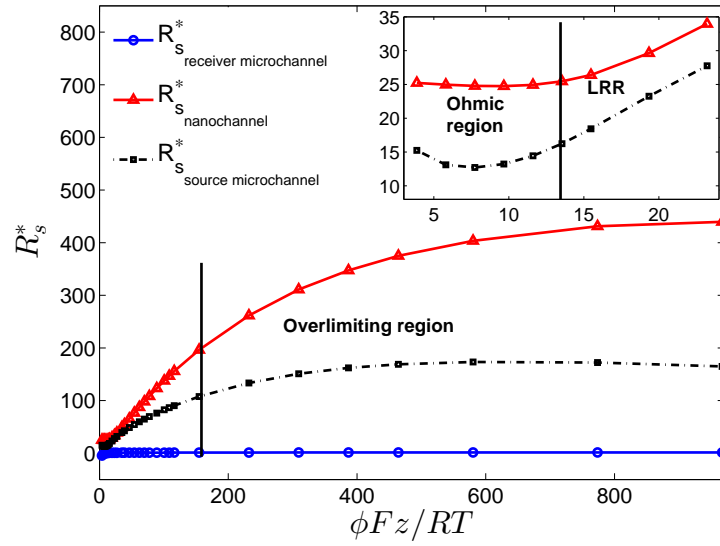
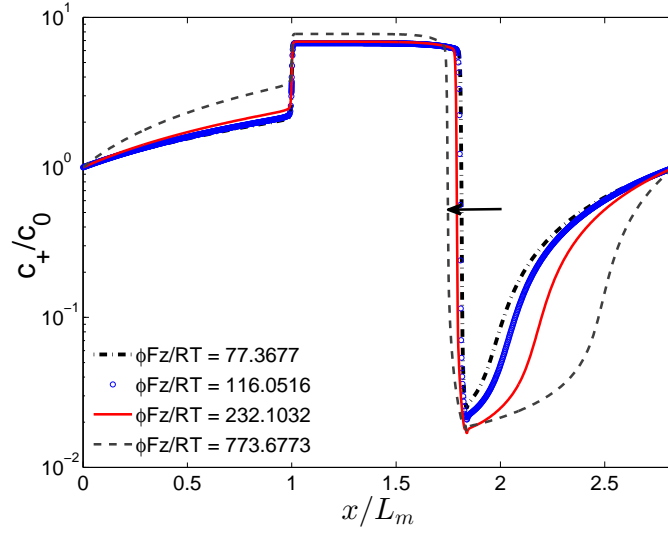
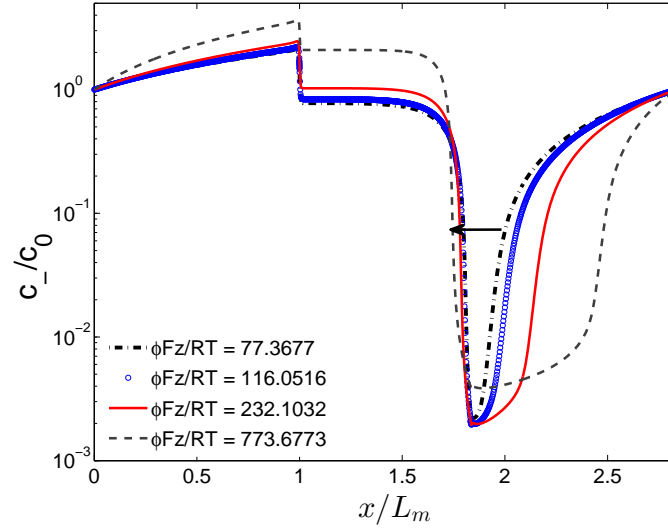


Figure 1.5: Variation of the normalized resistance as a function of the normalized DC voltage in different regions of the system. The bold line indicates the transition to the overlimiting region. The inset of the figure shows the variation of the normalized resistance in the Ohmic and limiting resistance region.



(a)



(b)

Figure 1.6: Normalized concentration along the axial direction of (a) cations (counter-ions) and (b) anions (co-ions) for various DC voltages, corresponding to the limiting resistance and overlimiting region. The solid arrow shows that, the induced space charge region, formed near the depletion source microchannel–nanochannel interface, propagates inside the nanochannel region under a large DC voltage,  $\phi^{DC} Fz/RT = 773.6773$ , corresponding to the overlimiting region.

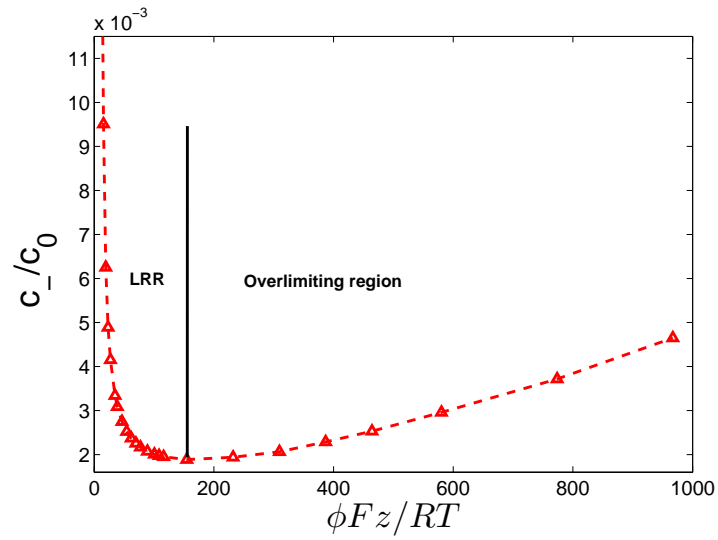


Figure 1.7: Variation of the minimum anion concentration (normalized) near the micro–nanochannel depletion interface for various normalized applied DC voltages corresponding to the limiting resistance (LRR) and overlimiting regions, respectively.

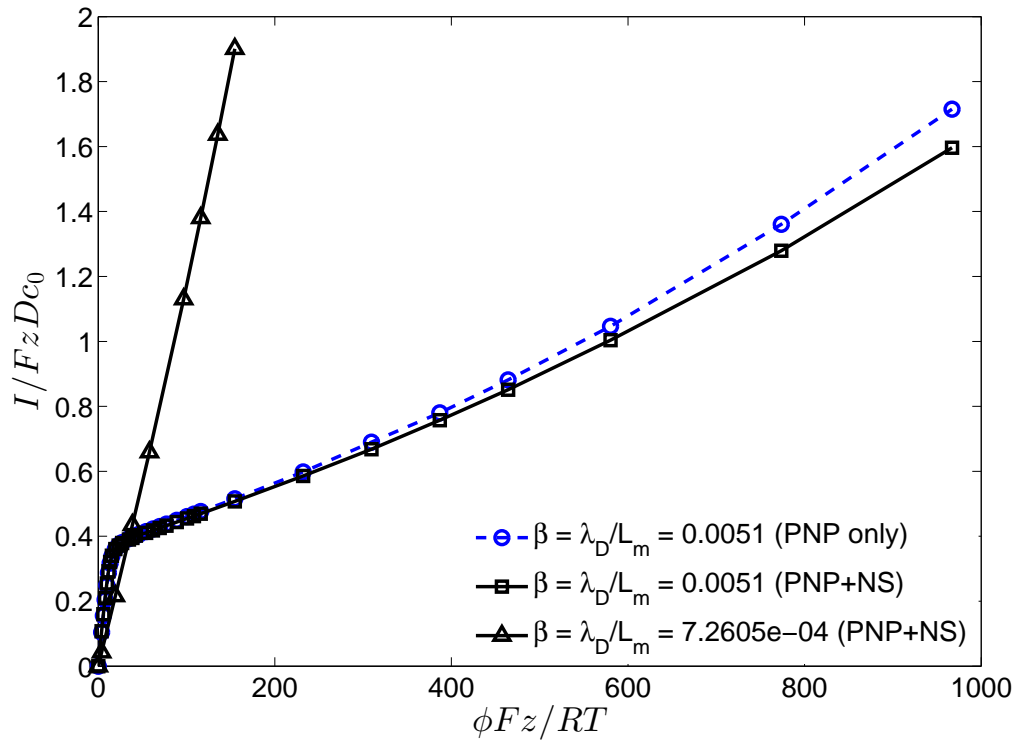


Figure 1.8: Effect of dimensionless EDL thickness ( $\beta = \lambda_D/L_m$ ) on the normalized current–voltage characteristics (in magnitude). Here  $\beta$  is varied by changing the bulk ionic concentration ( $c_0$ ) of the electrolyte.

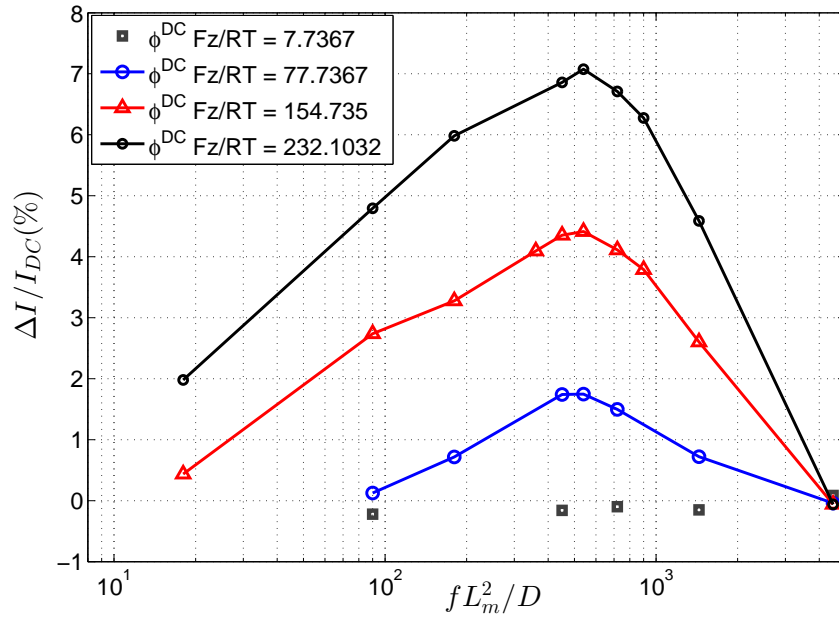


Figure 1.9: Relative current rectification as a function of nondimensional frequency ( $fL_m^2/D$ ) for various DC voltages, at a constant  $\alpha = \phi^{AC}/\phi^{DC} = 1.333$  and  $\beta = 0.0051$ .

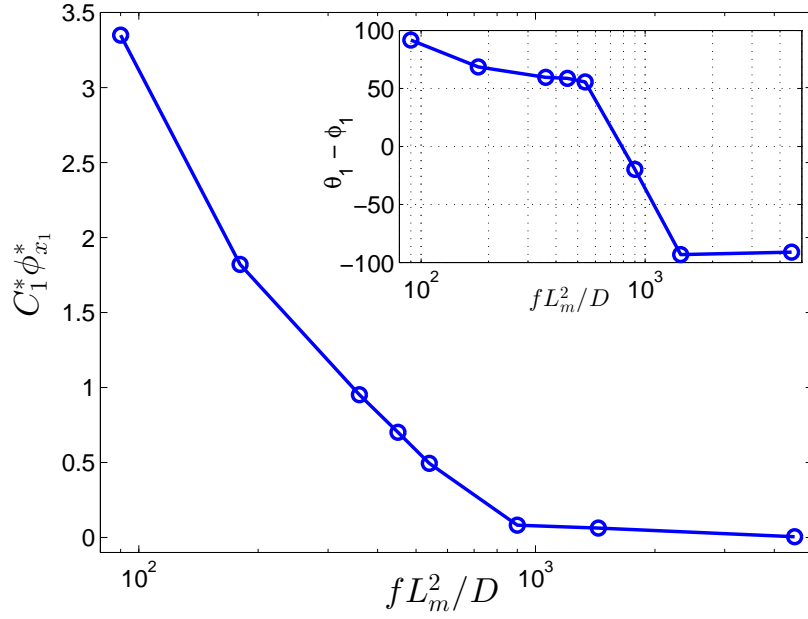


Figure 1.10: Numerically calculated normalized first harmonic contribution of total ionic concentration and field,  $(C_1^* \phi_{x_1}^*)$  in the induced space charge region at  $x/L_m = 2$ , as a function of nondimensional frequency ( $f L_m^2 / D$ ), at a constant DC voltage  $\phi^{DC} Fz / RT = 154.7354$ ,  $\alpha = 1.333$  and  $\beta = 0.0051$ . The inset of the figure shows the relative phase angle between  $C_1^*$  and  $\phi_{x_1}^*$  as a function of nondimensional frequency.

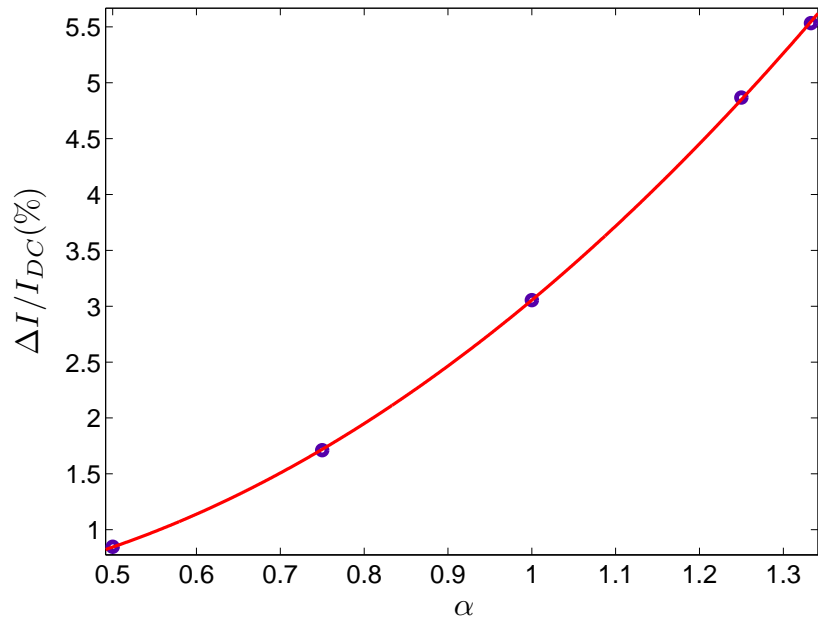


Figure 1.11: Relative current rectification as a function of  $\alpha$  at a constant DC voltage,  $\phi^{DC} Fz/RT = 154.7354$ ,  $fL_m^2/D = 450$  and  $\beta = 0.0051$ .

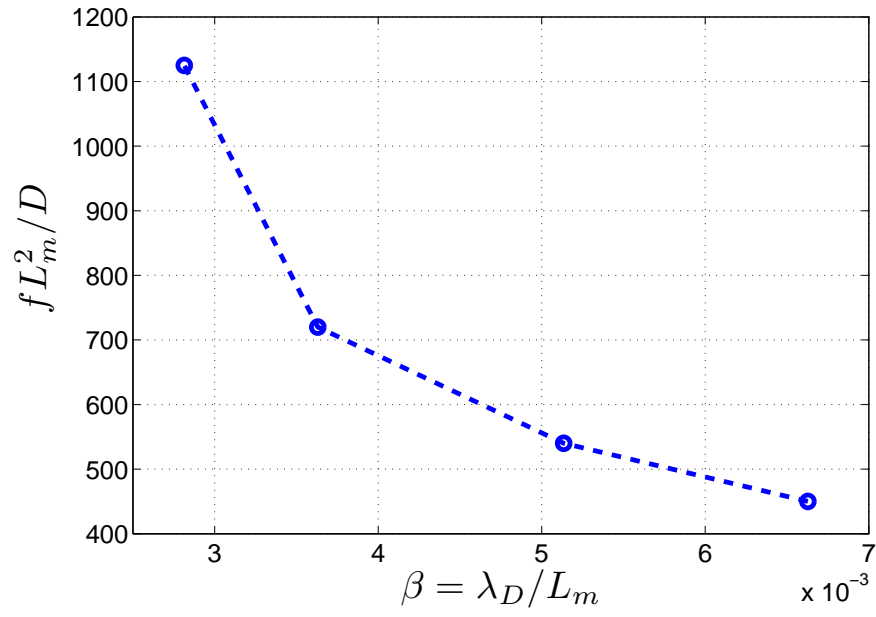


Figure 1.12: Dimensionless frequency (at which positive current rectification is maximum) as a function of nondimensional EDL thickness ( $\beta$ ) at a fixed DC voltage,  $\phi^{DC} Fz/RT = 154.7354$  and  $\alpha = 1.333$ .

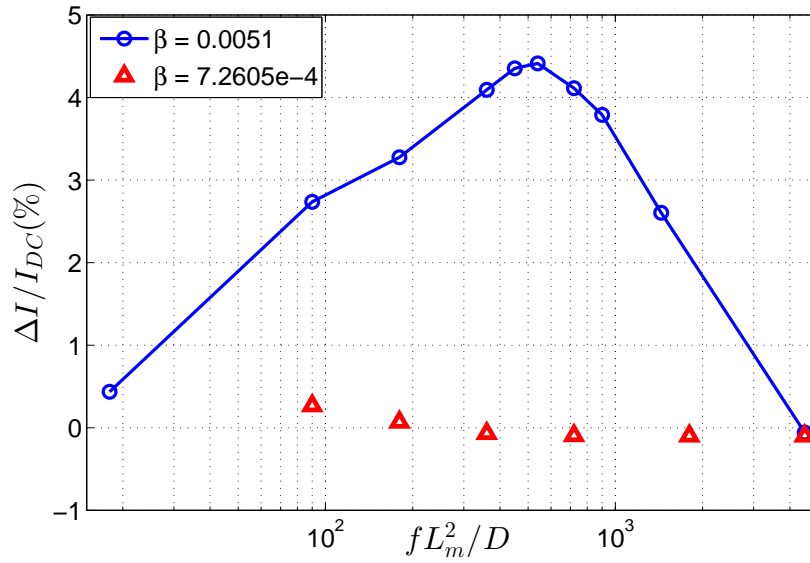


Figure 1.13: Effect of dimensionless EDL thickness ( $\beta$ ) and nondimensional frequency ( $fL_m^2/D$ ) on relative current rectification at a constant DC voltage,  $\phi^{DC}Fz/RT = 154.7354$  and  $\alpha = 1.333$ .

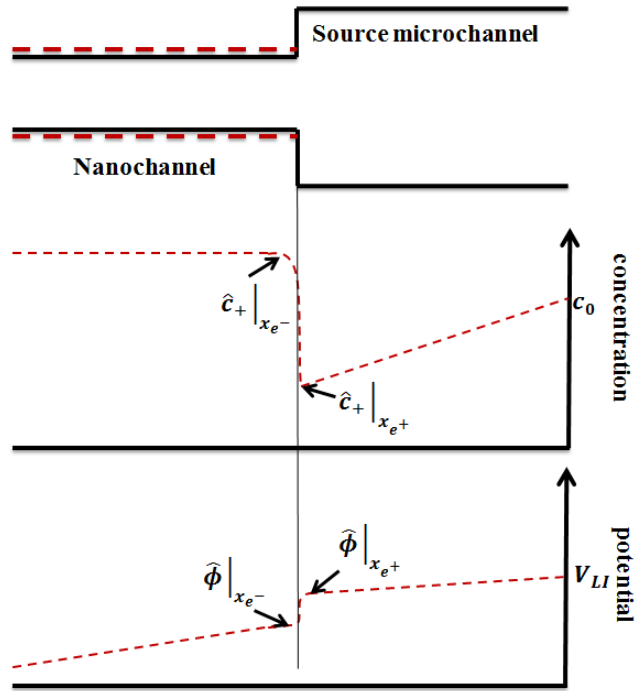


Figure 1.14: Schematic representation of a cation-selective nanochannel (top) illustrating the cation concentration (middle) and potential distribution (bottom) near the anodic micro-nanochannel interface under the application of first critical voltage, which results in the appearance of the limiting resistance region.

## 1.11 References

1. [Qiao and et al.(2005)] R. Qiao, et al., Colloid. Surface. A 267 (2005) 103109.
2. [Jin and et al.(2007)]X. Jin, et al., Langmuir 23 (2007) 1320913222.
3. [Mani and et al.(2009)]A. Mani, et al., Langmuir 25 (2009) 38983908.
4. [Postler and et al.(2008)]T. Postler, et al., J. Colloid Interface Sci. 320 (2008) 321332.
5. [Choi and et al.(2009)]Y. S. Choi, et al., J. Colloid Interface Sci. 333 (2009) 672678.
6. [Kim and et al.(2007)]S. J. Kim, et al., Phys. Rev. Lett. 99 (2007) 044501.
7. [Yossifon and et al.(2008)] G. Yossifon, et al., Phys. Rev. Lett. 101 (2008) 254501.
8. [Chang and et al.(2008)] G. Yossifon, et al., Phys. Rev. E 79 (2009) 046305.
9. [Rubinstein and et al.(2009)] I. Rubinstein, et al., Phys. Rev. E. 80 (2009) 021505.
10. [Rubinstein(1990)] I. Rubinstein, Electrodifusion of ions, SIAM, Philadelphia, 1990.
11. [Staude and et al.(1988)]I. Rubinstein, et al., Desalination 69 (1988) 101114.
12. [Hille(2001)]B. Hille, Ion Channels of Excitable Membranes, Sinauer Associates Inc., Sunderland, MA, 3rd edition, 2001.
13. [<http://www.openfoam.com/>(2011)] <http://www.openfoam.com/>, 2011.
14. [Toro(1999)] E. F. Toro, Riemann Solvers and Numerical Methods for Fluid Dynamics, SpringerVerlag, 1999.
15. [Schoch and et al.(2008)] R. B. Schoch, et al., Rev. Mod. Phys. 80 (2008) 839883.

# Chapter 2

## Characterization of electrochemical properties of a micro-nano channel integrated system using computational impedance spectroscopy (CIS)

### 2.1 Abstract

The integration of a microchannel with an ion-selective nanochannel exhibits nonlinear current–voltage characteristics owing to the concentration polarization effects. In this chapter, an efficient computational impedance spectroscopic technique (CIS) is developed for the first time using an area averaged multi-ion transport model (AAM). Using this technique, we investigate the ion transport dynamics in the Ohmic and non-Ohmic regions. Under no external DC bias and in the Ohmic regime, we observe two distinct arcs. The low frequency diffusional arc characterizes the diffusion–transport and the electrical double layer (EDL) charging effects at the interface of the micro–nanochannel, while the high frequency geometric arc characterizes the electric migration and displacement current effects inside the nanochannel and in the microchannel. Further, we observe an anomalous inductive arc at low frequencies ( $f L_m^2/D \leq 1$ ), in the overlimiting regime. This arc is primarily attributed to the phase effects between the first harmonic contribution of the total ionic concentration and the electric field in the induced space charge region. The microscopic diffusion boundary layer (DBL) lengths observed in the microchannel are also efficiently characterized from the impedance spectrum. Equivalent circuit models are designed to interpret the impedance response.

## 2.2 Introduction

Nanofluidic devices are being fabricated at a rapid rate in recent years[Dekker(2007)], as they are attracting tremendous interest from diverse fields including chemistry, physics, engineering and biological life sciences[Krems et al.(2010), Siwy et al.(2002) and Schoch et al.(2008)]. This stems from the fact that a nanopore can be used for a variety of applications, including single molecule/particle sensing[Howorka et al.(2009) and Saleh et al.(2003)], DNA sequencing[Chen et al.(2010), Kasianowicz et al.(1996) and Chang et al.(2004)], preconcentration of analytes using electric field focusing[Piruska et al.(2010)] and water desalination[Kim et al.(2010)]. In all these applications, the nanochannel is typically integrated with a microchannel on either side and a potential difference is applied between the ends of the microchannel[Piruska et al.(2010), Jin et al.(2007), Postler et al.(2008) and Choi et al.(2009)]. The microchannel influences the transport inside the ion-selective nanochannel under higher electric fields due to concentration polarization effects[Pu et al.(2004), Mani et al.(2009) and Zangle et al.(2009)]. The micro-nanochannel integrated electrochemical system (MNECS) displays current rectification behavior, resulting in three different regimes, namely, Ohmic, finite differential limiting resistance and overlimiting regimes[Kim et al.(2007), Yossifon et al.(2008) and Chang et al.(2009)].

Conductivity measurements obtained using DC voltammetry are useful in providing evidence for the interfacial double layer effects near the micro-nanochannel, and the electrostatic interactions near the nanochannel surface. However, fundamental knowledge regarding the phase sensitive capacitive and inductive effects in these systems is inaccessible through DC measurements. Impedance spectroscopy technique, which measures the complex impedance response of the system as a function of frequency[Barsoukov et al.(2005)] is currently being used to understand the ion transport dynamics in nanofluidic systems. As different frequency ranges can be selected, the phase sensitive information can be experimentally measured. Though there has been some recent experimental progress to understand the elec-

trochemical transport in nanopore geometry, there is inadequate theoretical/computational development to understand the impedance response of micro–nanochannel integrated systems. This is due to the computational challenges encountered in modeling the multi–domain and multi–phenomenon system. Hence an equivalent circuit modeling approach is preferred to fit the experimental observations. However, it is important to note that the same data can be modeled using different equivalent circuits which may not depict the exact physical nature of the problem.

In this chapter, we develop an area–averaged multi–ion transport model (AAM), considering the entire micro–nanochannel system. A computational impedance spectroscopic technique (CIS) is developed to characterize the electrochemical properties of the system. In this method, we apply a small amplitude periodic electric potential disturbance (AC) over a wide range of frequency spectrum along with a constant electric potential (DC). The technique is used to study the ion–transport dynamics in the Ohmic and non–Ohmic regimes. The model considers the effect of displacement current along with the conduction current contribution due to diffusion and electric migration processes.

In the Ohmic region, we observe multiple arcs in the impedance spectrum, which is attributed to the diffusion–transport near the micro–nanochannel interface, and the transport effects inside the nanochannel. In the limiting resistance region (LRR), an additional resistance–capacitance (RC) arc is observed. This is primarily due to the space charges induced near the micro–nanochannel depletion interface. Further, an anomalous inductive arc is observed in the overlimiting regime. The origin of this arc is discussed. Using the impedance spectra, we also highlight the important time scales at which negative and positive AC rectification effects are observed in the system.

## 2.3 Theory

### 2.3.1 Area-averaged multi-ion transport model (AAM)

In equilibrium and under the Ohmic regime, a typical micro-nanochannel integrated system (see Figure 2.1(a)) can be divided into 5 different regions including the ion-selective nanochannel. At both the interfaces of the micro-nanochannel, we observe a thin electrical double layer (EDL) region. An electroneutral enrichment and depletion diffusion boundary layers (DBL) are observed adjacent to the EDL region. The DBL region extends until the ends of the microchannel, where the concentration of the ionic solution is the bulk ionic concentration ( $c_0$ ). The EDL and DBL regions are formed outside the nanochannel owing to the concentration polarization effects [Pu et al.(2004)]. A schematic representation of all these regions is shown in Figure 2.1(a). Under the application of high electric fields, the integrated system experiences nonlinear current characteristics. Using a 2-D continuum based nonlinear ion-transport model, the transition from the limiting resistance region to a constant conductivity overlimiting behavior was attributed to the redistribution of the charges near the micro-nanochannel depletion interface. The fluidic nonlinearity was found to play a minimal role during this transition. However, the 2-D model offers computational challenges to study the impedance response of MNECS over a wide range of frequency spectrum. Hence, we propose a computationally efficient area averaged multi-ion transport model, considering the entire micro-nanochannel system. We neglect the fluidic effects in the model due to the aforementioned reasons. A systematic reduction of the 2-D nonlinear model into a dimensionless area-averaged model and the necessary boundary conditions are discussed in the supporting information.

From the governing equations, we obtain two important non-dimensional numbers,  $\beta = \lambda_D/L_m$  and  $\frac{\sigma^*}{h^*}$ . The former characterizes the effect of the electrolyte concentration in the system as the Debye length ( $\lambda_D = \sqrt{\epsilon_0\epsilon_r RT/2F^2 z^2 c_0}$ ) determines the thickness of the EDL.  $L_m$  is length of the microchannel.  $\frac{\sigma^*}{h^*}$  characterizes the effect of the ratio of wall surface charge

density to the channel cross–section. Variables with superscript “\*” are the dimensionless variables.  $h^*$  is the normalized height varying along the axial direction to represent the microchannel and the nanochannel, respectively.  $\epsilon_0$  is the permittivity of free space and  $\epsilon_r$  is the relative permittivity of the medium. The constants  $F$ ,  $R$ , and  $T$  represent Faraday’s constant, ideal gas constant and absolute thermodynamic temperature, respectively. In this work, a symmetric monovalent electrolyte ( $z_+ = -z_- = z$ ) like  $KCl$  is considered and we normalize the diffusion coefficient of each ionic species with the characteristic diffusion coefficient,  $D = 2 \times 10^{-9} m^2/s$ . New solvers for the area–averaged transport model are developed and implemented using the finite volume method in OpenFOAM (Open Field Operation and Manipulation) version 1.6[[http://www.openfoam.com/\(2011\)](http://www.openfoam.com/(2011))]. The model is validated with the 2–D model developed in the earlier chapter.

### 2.3.2 Computational impedance spectroscopy (CIS)

In order to study the ion transport dynamics in MNECS, the applied electric potential ( $\phi(t)$ ) and the output current per unit width ( $I(t)$ ) are expressed in complex form;

$$\phi(t) = \phi_{DC} + \phi_{AC} \sin(\omega t) = \phi_{DC} + \text{Re} (\phi_{AC} e^{j(\omega t + \theta_V)}) \quad (2.1)$$

$$I(t) = I_{DC} + \text{Re} (I_{AC} e^{j(\omega t + \theta_I)}) \quad (2.2)$$

where  $\phi_{DC}$  and  $I_{DC}$  are the DC component of the electric potential and current per unit width, respectively.  $\phi_{AC}$  and  $I_{AC}$  represent the amplitude of the perturbed AC electric potential and current per unit width, respectively.  $\omega$  is the applied angular frequency ( $\omega = 2\pi f$ ,  $f$  is the applied frequency) and  $\text{Re}$  is the operator “real part of”.  $\theta_V (= \frac{3\pi}{2})$  is the fixed phase angle of the applied harmonic electric potential,  $\theta_I$  represents the phase angle of the perturbing electric current. We would like to point out that the output current per unit width is calculated at the end of the source reservoir. It is then converted into frequency

domain using the fast Fourier transform (FFT) algorithm in Matlab[Frigo et al.(1998)] to obtain the amplitude and phase information. The details of the algorithm are presented in the section 2.6 information. The complex electrochemical impedance is given by  $Z(\omega) = |Z_0|e^{j\theta_z} = Re(Z) + jIm(Z)$ .  $|Z_0| = \frac{|\phi_{AC}^*|}{|I_{AC}^*|}$  is the magnitude of the normalized electrochemical impedance, considering the normalized perturbed potential,  $\phi_{AC}^* = \phi_{AC}Fz/RT$ , and the normalized perturbed current per unit width,  $I_{AC}^* = I_{AC}/FzDc_0$ .  $\theta_z = \theta_V - \theta_I$  is the relative phase difference between the applied harmonic electric potential and the perturbing current, and  $j = \sqrt{-1}$  is the imaginary unit. Knowing the magnitude and phase of the impedance, we calculate the normalized real ( $Re(Z) = |Z_0|\cos\theta_z$ ) and the imaginary ( $Im(Z) = |Z_0|\sin\theta_z$ ) part of the impedance, respectively. A flow chart to calculate the impedance response of MNECS is shown in Figure 2.1(b).

## 2.4 Simulation details

The simulated domain consists of a rectangular nanochannel of length  $L_n = 5 \mu m$  and half height  $H_n = 15 nm$  connected to two microchannels of length  $L_m = 6 \mu m$  and half height  $H_m = 500 nm$ , on either side of the nanochannel (see Figure 2.1(a)). The operating temperature is  $T = 300 K$ . The diffusivities of  $K^+$  and  $Cl^-$  are  $1.96 \times 10^{-9} m^2/s$  and  $2.03 \times 10^{-9} m^2/s$ , respectively. We assume the dielectric constant of the aqueous solution to be,  $\epsilon_r = 80$ [Hille(2001)]. We also assume zero surface charge density on the walls of the microchannel,  $\sigma_m = 0$ , as they are away from the nanochannel membrane to have an influence on the transport. In this study, we primarily focus our attention on understanding the EDL effects at the interface, and hence, assume a constant and a homogeneous surface charge density on the walls of the nanochannel,  $\sigma_n^*/h_n^* = -3.4548$ .

## 2.5 Results and discussion

### 2.5.1 Impedance characteristics under no DC bias

Figure 2.2(a) shows the normalized impedance spectrum in the form of a Nyquist plot (Imaginary( $Z$ ) vs Real( $Z$ )) under no external DC bias. The applied frequency,  $f$ , increases from the right to the left of the plot. In this case, we consider a low bulk ionic concentration,  $c_0 = 0.1 \text{ mM}$  (corresponding to a thick EDL regime,  $\beta = 5.1334 \times 10^{-3}$ ) and apply a small AC amplitude,  $\phi_{AC}Fz/RT = 3.8683$ . A frequency range from  $5 \text{ Hz}$  to  $5 \text{ MHz}$  is applied to understand the phase sensitive electrochemical properties. The spectrum reveals two distinct arcs. We define the arc in the low frequency regime as the diffusional arc. This is because this arc characterizes the diffusion–transport outside the nanochannel. In the diffusional arc, the Nyquist plot shows a linear behavior at its high frequency edge near the point of coincidence of the two arcs. This linear behavior is in accordance with the classical Warburg type impedance for semi–infinite oscillating diffusion [Barsoukov et al.(2005)]. However, the diffusional arc closes back on the real axis in an arc as the frequency approaches zero. The finite diffusion lengths are attributed to the breakdown of the Warburg impedance [Rubinstein et al.(2009)]. The characteristic diffusional arc can be represented by the diffusion (-O-) circuit element or also referred to as the open finite length diffusion circuit element ( $Z_D(\omega)$ )[Jacobsen et al.(1995)],

$$Z_D(\omega) = R_D \frac{\tanh[\sqrt{(j\omega\tau_D)}]}{\sqrt{(j\omega\tau_D)}}, \quad (2.3)$$

where  $R_D$  depicts the interfacial resistance contributed by both the EDLs and the resistance in the enrichment and depletion DBL due to the concentration gradients.  $\tau_D = \frac{L_{DBL}^2}{D}$ , is the diffusional relaxation time relating the length of the diffusion boundary layer ( $L_{DBL}$ ) and the diffusion coefficient of the ions in this layer. It is well known that the imaginary part of the impedance (with the negative sign) for the diffusion O element reaches a max-

imum when  $\omega\tau_D = 2.54$  [Diard et al.(1999)], i.e., at the characteristic frequency given by  $f_D = \frac{2.54D}{2\pi L_{DBL}^2}$ . From our simulations, Figure 2.2(a) shows that this frequency ( $f_D$ ) is around 20 Hz. Substituting in the aforementioned relation results in the estimation of the length of the electroneutral diffusion boundary layer which is approximately equal to the length of the microchannel. The result is consistent as the system is almost electroneutral through out the microchannel, when there is no external DC bias. We also note that in the diffusional arc, when the applied frequency is less than  $f_D$ , we do not observe any contribution from the displacement current (as the rate of change of electric displacement field is negligible at such low applied frequencies). Hence, there is no charging of the EDL at these frequencies and it can be assumed to be in equilibrium. However, for  $f > f_D$ , the inset of Figure 2.2(a) shows a higher  $-Im(Z)$  when the displacement current is considered compared to the case without considering them. The higher  $-Im(Z)$  indicates the charging of the EDL at frequencies beyond  $f_D$ . Thus, the impedance response in the EDL and DBL regions due to the combined diffusional and displacement current outside the nanochannel can be represented by considering a diffusion O element in parallel with an EDL capacitor.

In Figure 2.2(a) we define the second arc in the high frequency regime as a geometric arc. We observe a distorted hemicircle in this arc. In order to understand this we consider the electromigration processes in both the microchannels and inside the nanochannel. Also, under no external DC bias, the system symmetry is still restored. The solution resistance ( $R_m$ ) (owing to the migration process) and the corresponding capacitance ( $C_m$ ) (due to the displacement current) in both the microchannels are the same. Hence, the characteristic frequency can be estimated by considering the resistance and capacitance of a single microchannel. Here, we consider the depletion microchannel for the analysis. Further,  $R_m$  and  $C_m$  are both parallel to each other as they are contributed by two different currents which are additive. Assuming a symmetric monovalent electrolyte, with equal diffusivities ( $D_+ = D_- = D$ ) and neglecting the diffusional and displacement current, we obtain the

current per unit width ( $I$ ) in the  $x$ -direction inside the microchannel

$$I = -\frac{2F^2 z^2 D H_m}{RT} \frac{d\hat{\phi}}{dx} (\hat{c}_+ + \hat{c}_-) \quad (2.4)$$

Here  $\hat{\cdot}$  denotes the area averaged quantity considering the width of the system to be unity. Under no external DC bias, neglecting the EDL effects, local electroneutrality is maintained throughout the microchannel, and is equal to the bulk ionic concentration ( $\hat{c}_+ = \hat{c}_- = c_0$ ). Upon integrating Eq. 2.4 along the length of the source microchannel and substituting the above condition, the solution resistance of the microchannel is  $R_m = \frac{RTL_m}{4F^2 z^2 D H_m c_0}$ . The corresponding capacitance of the microchannel is  $C_m = 2\epsilon_0 \epsilon_r H_m / L_m$ . Using  $R_m$  and  $C_m$ , the characteristic frequency of the source microchannel is  $f_m = \frac{1}{2\pi R_m C_m} = \frac{D}{2\pi \lambda_D^2}$ . Following the above procedure, the current per unit width inside the nanochannel is  $I = -\frac{2F^2 z^2 D H_n}{RT} \frac{d\hat{\phi}}{dx} (\hat{c}_{n+} + \hat{c}_{n-})$ . Here  $\hat{c}_{n+}$  and  $\hat{c}_{n-}$  are the counter-ion and co-ion concentrations inside the nanochannel (averaged over the height of the nanochannel). The individual ionic concentrations inside the nanochannel can be approximately calculated using the Donnan equilibrium theory [Schoch and et al.(2008)] as  $\hat{c}_{n\pm} = \pm \frac{\bar{c}}{2} + \sqrt{\left(\frac{\bar{c}}{2}\right)^2 + c_0^2}$ .  $\bar{c} = \hat{c}_{n+} - \hat{c}_{n-} = -\frac{\sigma_n}{FzH_n}$ , is obtained from the electroneutrality condition inside the nanochannel, considering the nanochannel wall surface charge density effects. Substituting the above expressions and integrating the current per unit width along the length of the nanochannel, the resistance of the nanochannel is given by  $R_n = \frac{RTL_n}{2F^2 z^2 D H_n (\hat{c}_{n+} + \hat{c}_{n-})}$ . Knowing the nanochannel capacitance  $C_n = 2\epsilon_0 \epsilon_r H_n / L_n$ , the characteristic frequency of the nanochannel is  $f_n = \frac{1}{2\pi R_n C_n} = \frac{F^2 z^2 D (\hat{c}_{n+} + \hat{c}_{n-})}{2\pi RT \epsilon_0 \epsilon_r}$ .  $R_n$  and  $C_n$  are parallel to each other owing to the similar arguments discussed for the microchannel.

The impedance  $Z(\omega)$  for a simple resistor ( $R$ ) and capacitor ( $C$ ) in parallel is  $Z(\omega) = \left(\frac{1}{R} + j\omega C\right)^{-1}$ . Substituting the aforementioned expressions for  $R_m$ ,  $C_m$ ,  $R_n$ ,  $C_n$ , we calculate the individual impedance of the source microchannel ( $Z_m$ ) and nanochannel ( $Z_n$ ). Figure 2.2(b) shows the impedance response of the source microchannel, nanochannel and the total response ( $Z_m + Z_n$ ) in the form of a normalized Nyquist plot. The total impedance

response is obtained by considering  $Z_m$  and  $Z_n$  in series with each other. We observe that the imaginary part of the nanochannel impedance ( $-Im(Z)|_n$ ) is greater than the source microchannel ( $-Im(Z)|_m$ ). Also,  $f_m$ , related to the source microchannel, is smaller compared to the characteristic frequency of the nanochannel ( $f_n$ ). As the frequency increases beyond  $f_m$ ,  $-Im(Z)|_m$  reduces, and when the applied frequency approaches  $f_n$ , the imaginary part of the microchannel impedance is small. Hence, the sum  $-(Im(Z)|_m + Im(Z)|_n)$  is approximately equal to  $-Im(Z)|_n$ . Thus, the frequency related to the maximum of imaginary part of nanochannel + microchannel impedance is approximately closer to  $f_n$ . While at low frequencies, close to  $f_m$ , the contribution of  $-Im(Z)|_m$  in the sum is considerable that results in a deviation from a perfect hemicircle. From the above analysis, we also understand that when  $f_n \gg f_m$ , there would be two semicircles related separately to the nanochannel and the microchannel. We also observe another characteristic frequency " $f_I$ " where the diffusional and the geometric arc meet (see Figure 2.2(a)). This frequency approximately corresponds to the geometric mean of  $f_D(\propto D/L_{DBL}^2)$  and  $f_m(\propto D/\lambda_D^2)$ , which reveals that  $f_I$  is proportional to  $D/(\lambda_D L_{DBL})$ . When the applied frequency is between  $f_D$  and  $f_I$ , the charging of the EDL is observed resulting in a higher  $-Im(Z)$  compared to the case without considering the displacement current as shown in the inset of Figure 2.2(a). This reveals that the EDL capacitance is dominant at frequencies of the order of  $f_I$ . Further at frequencies greater than  $f_I$ , the capacitance of the nanochannel ( $C_n$ ) and the microchannel ( $C_m$ ) dominate compared to the EDL capacitance. From the preceding expressions for  $f_n$ ,  $f_m$  and  $f_I$ , we observe that these three characteristic frequencies are dependent on the bulk ionic concentration. In order to establish consistency in our hypothesis, we perform computations at different bulk electrolyte concentration,  $c_0 = 0.01 \text{ mM}$  (see Figure 2.3(a)), and  $1 \text{ mM}$  (see Figure 2.3(b)). This corresponds to  $\beta = 16.235 \times 10^{-3}$  and  $\beta = 1.6235 \times 10^{-3}$ , respectively.

Figure 2.3(a) reveals both the characteristic frequencies  $f_m$  and  $f_n$  in the geometric arc. When the bulk ionic concentration is reduced by an order of magnitude, the resistance of the microchannel ( $R_m$ ) increases by one order and  $C_m$  is independent of the concentra-

tion variation. The increase in the microchannel resistance decreases  $f_m$  by one order. The approximate analytical values of  $f_m$  ( $= 33.546$  kHz) and  $f_n$  ( $= 1.159$  MHz) are in close agreement with the numerical simulations. From the earlier discussion, as  $f_n \gg f_m$  it is possible to distinguish the two arcs corresponding to the migration processes inside the microchannel and the nanochannel. Further for the bulk concentration considered, the resistance of the microchannel is found to be greater than the nanochannel resistance. This results in a higher impedance of the microchannel arc compared to the nanochannel. Figure 2.3(a) shows that the diffusional arc in this case becomes predominant due to the thick electrical double layer formed at the interface of the micro–nanochannel. However, the frequency  $f_D$  is found to be independent of the electrolyte concentration (consistent with the expression obtained for  $f_D$ ), while  $f_m$ ,  $f_n$  and  $f_I$  were found to vary with the concentration. Similar characteristics are also observed at  $\beta = 1.6235 \times 10^{-3}$  as shown in Figure 2.3(b). However, we notice that, it is difficult to observe the diffusion arc at this concentration (see inset of Figure 2.3(b)). This can be understood from the fact that, at high concentration limit, the electrical double layer at the interface diminishes resulting in a decrease in the resistance  $R_D$ . To understand the contribution of diffusion–transport at the micro–nanochannel interface compared to the migration effects inside the nanochannel, for different bulk concentrations, we calculate the ratio of the imaginary part of the impedance corresponding to the diffusional and nanochannel characteristic frequencies  $\left(\chi = \frac{Im(Z)|_{f_D}}{Im(Z)|_{f_n}}\right)$ . Table 2.1 shows that at a very low bulk ionic concentration,  $\beta = 16.235 \times 10^{-3}$ , the diffusion–transport near the interface is nearly 2.4 times dominant compared to the migration effects inside the nanochannel. However, with increase in the ionic concentration, we observe a power law type decrease in  $\chi$ . The contribution of the diffusion–transport near the interface reduces to 6% compared to the transport effects inside the nanochannel for a high bulk electrolyte concentration,  $\beta = 1.6235 \times 10^{-3}$ . Figure 2.3(b)) also shows that the geometric arc is close to a perfect semicircle. This can be attributed to two reasons. First, the surface charge density on the walls of the nanochannel play a minimal role as the electrostatic interactions near the surface is screened by the ex-

cess ions. Second, the resistance and hence the impedance response of the microchannel is minimal due to the large bulk electrolyte concentration.

Additional simulations are performed by varying the microchannel geometry to ensure that the DBL length (obtained from  $f_D$ ) is characterized efficiently. The results are presented in the supporting information (see Figure 2.8).

## 2.5.2 Effect of DC potential bias

Figure 2.4(a) compares the spectra in the Ohmic–regime ( $\phi_{DC}Fz/RT = 3.8684$ ), with that of the no bias case. We note that under a DC bias, the diffusion boundary layer is polarized[Pu et al.(2004)]. The ionic concentration decreases from the bulk to the interface in the depletion microchannel and increases near the enrichment microchannel interface. The enrichment effects do not significantly contribute to the DBL resistance[Yossifon et al.(2009)]. However, the decrease in the concentration near the depletion interface increases the diffusional DBL resistance. Hence, we observe a slight increase in the impedance of the diffusional arc. Also for the applied DC bias, we observe negligible change in the electric migration process inside the microchannel and nanochannel, compared to the no bias case. Hence, the distorted geometric arc overlaps with the previous no bias case. The resistance due to the electromigration process in both the microchannels and the nanochannel can be estimated from the width of the geometric arc. The total width of the impedance spectrum gives the total resistance of the system, under DC bias. In spite of the presence of depletion and enrichment DBL regions, electroneutrality is maintained in the microchannel (beyond the EDL interface). Hence, the length of the DBL region is unaffected in the Ohmic regime, resulting in the same characteristic diffusion frequency ( $f_D$ ). The inset of the figure displays the Bode plot indicating the relative phase difference  $\left(\theta = -\tan^{-1}\frac{Im(Z)}{Re(Z)}\right)$  with respect to different normalized frequency. We observe a phase shift maximum corresponding to the characteristic diffusional frequency,  $f_D$ . A monotonic increase in the phase at frequencies greater than  $f_I$  is attributed to the capacitive effects of the microchannel and nanochannel

rather than that of the EDL.

A further increase in the DC bias,  $\phi_{DC}Fz/RT = 77.3677$  corresponding to the limiting resistance regime, results in the breakdown of the classical diffusional arc and the merging of the two characteristic arcs as shown in Figure 2.4(b). The merging is accompanied by an additional resistance-capacitance (RC) arc with a new characteristic frequency,  $f_m$ . We also observe an increase in the frequency,  $f_D$ . We attribute these effects to the space charges induced due to the strong electromigration effects near the micro–nanochannel depletion junction. To confirm this physics, we numerically calculate the total charge ( $Q_{SCR}$ ) per unit width in the induced space charge region (SCR), by integrating the space charge density ( $\hat{\rho}_e = Fz(\hat{c}_+ - \hat{c}_-)$ ), along the length of SCR. We also assume that the charges predominantly propagate towards the microchannel in the LRR regime. The charge propagation reduces the length of the electroneutral depletion DBL. Substituting the new diffusional frequency ( $f_D$ ) in the expression for  $f_D$ , we obtain the reduced DBL length ( $L_{DBL}^{new}$ ) and the corresponding length of the SCR,  $L_{SCR} = L_m - L_{DBL}^{new}$ . The total charge per unit width is  $Q_{SCR} = 2H_m \int_{x_e}^{L_{SCR}} \hat{\rho}_e dx$ .  $x_e$  is the coordinate where the nanochannel ends. We determine the capacitance inside the SCR ( $C_{SCR}$ ) by calculating the corresponding voltage drop ( $V_{SCR} = \hat{\phi}|_{L_{SCR}} - \hat{\phi}|_{x_e}$ );  $C_{SCR} = Q_{SCR}/V_{SCR}$ . Knowing the total current per unit width ( $I$ ), the new characteristic frequency in the SCR is calculated as  $f_m = \frac{1}{2\pi R_{SCR} C_{SCR}}$ . Here  $R_{SCR} = V_{SCR}/I$ . Substituting all the numerical values [ $L_{DBL}^{new} = 4.925 \mu m$ ,  $L_{SCR} = 1.0705 \mu m$ ,  $Q_{SCR} = 0.2656 nC/m$ ,  $V_{SCR} = 0.3163 V$ ,  $I = 8.6332 \mu A/m$ ,  $C_{SCR} = 0.8396 nF/m$ ,  $R_{SCR} = 36.643 k\Omega m$ ], the approximate characteristic frequency is  $5.1735 kHz$  which is in good agreement with the numerical simulation, and hence, confirming our hypothesis. The above analysis also helps us to understand that the impedance spectra can be used to measure the reduced microscopic DBL and new SCR lengths in the LRR regime without probing inside the microchannel. This is unlike the earlier probing techniques[Yossifon et al.(2009) and Rubinstein et al.(1988)], in which the thickness of the vortex array, developed due to the instabilities in the space charge region is measured to characterize the same. The inset of

the figure displays the Bode phase plot where we observe a second phase–shift maximum at a characteristic frequency,  $fL_m^2/D = 360$ , unlike the previous case. Similar characteristics are also observed for a higher DC bias ( $\phi_{DC}Fz/RT = 154.735$ ), corresponding to the LRR regime. This feature is observed even without considering the displacement current (see Figure 2.9) which illustrates that it is due to the strong electrophoretic interaction resulting in the induced space charges near the depletion interface. Finally, the third arc with characteristic frequency  $f_n$ , along with an increase in the phase ( $\theta$ ) at  $f \geq f_n$  (as shown in the Bode phase plot in the inset of Figure 2.4(b)) reveal the electric migration and capacitance effects of the nanochannel.

We now repeat the analysis, in the third regime at a DC bias ( $\phi_{DC}Fz/RT = 773.677$ ), corresponding to the overlimiting behavior, which results in a higher current in the I–V characteristics (see Figure 2.7). The overlimiting regime in a negatively charged nanochannel was characterized owing to the redistribution of the charges near the micro–nanochannel depletion interface. This redistribution is accompanied by an enhanced conductivity of the chloride ions near this interface, resulting in an enhanced current. Figure 2.4(c) shows the impedance spectrum in this regime. We observe an anomalous inductive arc at low frequencies,  $fL_m^2/D \leq 1$ , which is revealed by the change in the sign of the imaginary part of the impedance. In other words, at these frequencies, the applied electric potential leads the output current ( $\theta_I - \theta_V < 0$ ) as shown by the Bode phase plot in the inset of Figure 2.4(c). As the harmonic electric potential disturbance is applied at a constant phase angle ( $\theta_V = 3\pi/2$ ), the changes in the phase of the output current should result in the inductive behavior. In order to understand these changes, we calculate the electric migration current per unit width in the induced space charge region using Eq. 2.4. Under the application of combined AC and DC electric potential, we assume,  $(\hat{c}_+ + \hat{c}_-) = C_0 + C_1 \cos(\omega t + \theta_1)$  and  $\frac{d\hat{\phi}}{dx} = \phi_{x_0} + \phi_{x_1} \cos(\omega t + \phi_1)$ , neglecting the contribution of other higher harmonic components.  $C_0$ ,  $\phi_{x_0}$  are the DC component of the total ionic concentration and the field, respectively.  $C_1$ ,  $\phi_{x_1}$  are the respective first harmonic contributions of the ionic concentration and field.  $\theta_1$  and  $\phi_1$

are the corresponding phase angles of the former and latter terms, respectively. Substituting the aforementioned expressions into Eq. 2.4 and multiplying the resulting current by  $-1$  to be consistent with the output current obtained from the numerical simulations, the current per unit width due to the combined AC and DC bias is calculated as,

$$I(t) = \frac{2F^2 z^2 DH_m}{RT} [C_0 \phi_{x_0} + (C_0 \phi_{x_1} \cos \phi_1 + C_1 \phi_{x_0} \cos \theta_1) \cos \omega t] - \frac{2F^2 z^2 DH_m}{RT} [(C_0 \phi_{x_1} \sin \phi_1 + C_1 \phi_{x_0} \sin \theta_1) \sin \omega t] \quad (2.5)$$

Here we also assume  $C_1 \phi_{x_1} \ll C_0 \phi_{x_0}$ . Comparing Eq. 2.5 and Eq. 2.2, we obtain the phase angle of the output current,  $\theta_I = \tan^{-1} \left( \frac{b_1}{a_1} \right)$ , where  $a_1 = \frac{2F^2 z^2 DH_m}{RT} (C_0 \phi_{x_1} \cos \phi_1 + C_1 \phi_{x_0} \cos \theta_1)$  is the real part and  $b_1 = \frac{2F^2 z^2 DH_m}{RT} (C_0 \phi_{x_1} \sin \phi_1 + C_1 \phi_{x_0} \sin \theta_1)$  is the imaginary part of the harmonic output current per unit width.

All the above variables are numerically calculated in the induced space charge region at  $x/L_m = 1.9167$ , for a given DC bias of  $\phi^{DC} Fz/RT = 773.677$  and  $\phi^{DC} Fz/RT = 77.3677$ . The values corresponding to overlimiting regime are tabulated in Table 2.3 (see supporting information) while that corresponding to the LRR is shown in Table 2.4 (see supporting information). From Table 2.3, we observe that in the overlimiting regime, the total ionic concentration and field tend to be in-phase with each other (i.e.,  $|\theta_1 - \phi_1| < \pi/2$ ). Also, at low frequencies,  $fL_m^2/D \leq 1$ , the phase of the ionic concentration is less than  $3\pi/2$ , while that of the field is greater than  $3\pi/2$ . As the perturbed concentration marginally lags behind the field, we observe that the real part of the harmonic current becomes less than zero ( $a_1 < 0$ ), along with the imaginary component,  $b_1 < 0$ . As both the real and imaginary part of the current are negative the phase angle of the output current is in the third quadrant, i.e.,  $\pi \leq \theta_I \leq 3\pi/2$ . This implies that the output current is lagging behind the applied perturbed voltage (as  $\theta_V = 3\pi/2$ ), resulting in the inductive behavior. Further, we observe a maximum lag between the output current and applied voltage when there is a maximum lag between the perturbed concentration and the electric field. This occurs at  $fL_m^2/D = 0.36$ ,

corresponding to a dimensional frequency of  $f_0 = 20 \text{ Hz}$ . At higher frequencies,  $fL_m^2/D > 1$ , the perturbed concentration leads the field ( $\theta_1 > \phi_1 > 3\pi/2$ ) which results in a positive contribution in  $a_1$ , while  $b_1$  is still negative. Hence, the phase angle of the current is in the fourth quadrant, implying that the current leads the applied voltage. Thus, at high frequencies we observe capacitive arc in the impedance spectrum. These arguments also help us to conclude that the origin of the inductive arc is due to the migration of the charges near the induced space charge region, as we have neglected the diffusive and displacement currents in the analysis. Additional computations were performed for another DC voltage ( $\phi_{DC}Fz/RT = 580.258$ ) corresponding to the overlimiting regime to ensure consistency in the observation. We repeated our analysis in the LRR regime under similar range of harmonic excitations. Table 2.4 shows that even though the harmonic concentration lags behind the field, they are always out of phase with each other by more than  $\pi$ . Under these conditions,  $a_1$  and  $b_1$  was always found to be in the fourth quadrant. These effects result in the current leading the applied voltage at all the frequencies, and hence, we observe only capacitive type behavior. Figure 2.4(c)) also shows that the inductive arc is accompanied by three deformed hemicircle arcs. The width of the impedance spectrum in the second arc (above the inductive arc) is lower compared to the limiting resistance regime. The increased chloride ion conductivity near the micro–nanochannel depletion junction is attributed to this lower impedance. We also observe an increase in the width of the third arc compared to the LRR regime with a new characteristic frequency,  $f_3 = 10 \text{ kHz}$ . We attribute these results to the fact that with increase in the DC bias, the length of the space charge region near the depletion interface increases resulting in a higher voltage drop and charge density. We would like to point out that in the entire impedance analysis, the amplitude of the harmonic disturbance is ensured to be small so that they do not interfere with the impedance spectra. This was checked by performing additional simulations with different small AC amplitude (demarcated in Figure 2.10)).

### 2.5.3 Equivalent circuit model design

Under no external DC bias, considering all the five regions inside the integrated microchannel independently, we can understand the transport in each region using the following circuit elements. A finite length diffusion element ( $Z_D^s$ ) in parallel with an EDL capacitor ( $C_{EDL}^s$ ) is used to represent the diffusion–transport in the DBL, and the EDL charging effects. The superscript “ $s$ ” indicates the source microchannel. To understand the electric migration process and the capacitance effects in the source microchannel, a resistor,  $R_m^s$  in parallel with a capacitor,  $C_m^s$  is considered. The aforementioned circuit elements are also used to model the transport in the drain microchannel, which are distinguished from the former elements with a superscript “ $D$ ”. Finally, the migration process and the displacement effects inside the nanochannel can be characterized using a resistor,  $R_n$  in parallel with a capacitor,  $C_n$ . Figure 2.5(a)) shows a series representation of the discussed circuit elements to represent the AC impedance response of MNECS. Owing to the presence of multiple EDLs at the micro–nanochannel interface, it is almost impossible to determine the individual capacitance and also the impedance  $Z_D$  analytically. Also, it is difficult to fit them as there are many unknown parameters. Hence, we propose a modified equivalent circuit in which the migration and displacement effects in the nanochannel and microchannel are characterized using a resistor in parallel with a constant phase element (CPE)[Barsoukov et al.(2005)]. A CPE is used instead of an ideal capacitor, with an arbitrary factor  $n$  owing to the non–ideal behavior arising due to the EDL effects. We note that  $n$  can vary from  $-1$  to  $1$ , where the end values illustrate an ideal inductor and a capacitor, respectively. Further, we characterize the migration effects in both the microchannels using a single  $R||CPE$  element. A single finite length diffusion element, whose functional form is given by Eq. 2.6 is used to characterize the diffusion–transport in both the DBLs. Figure 2.5(b)) shows the modified equivalent circuit. Considering these elements in series, the functional form to characterize

the impedance spectra under no external DC bias is represented as,

$$Z(\omega) = \left( \frac{1}{R_1} + (j\omega)^{n_1} CPE_1 \right)^{-1} + \left( \frac{1}{R_2} + (j\omega)^{n_2} CPE_2 \right)^{-1} + R_D \frac{\tanh[\sqrt{(j\omega\tau_D)}]}{\sqrt{(j\omega\tau_D)}} \quad (2.6)$$

where  $R_1$ ,  $CPE_1$  represent the resistance, constant phase element of the nanochannel, respectively.  $R_2$ ,  $CPE_2$  represent the resistance, constant phase element of both the microchannels, respectively.  $n_1$ ,  $n_2$  are the arbitrary factors. To determine  $R_1$ ,  $CPE_1$ , and  $n_1$ , we neglect the microchannel and perform the simulations considering only a nanochannel of length  $L_n = 5 \mu m$  and  $H_n = 15 nm$  at a constant  $\beta = 5.1334 \times 10^{-3}$ . A perfect semicircle with a single characteristic frequency is observed in the impedance spectrum. The data is fitted to Eq. 2.6 (considering only the first term) using non-linear least squares method. The obtained values are tabulated in Table 2.2. Using these values, we characterize the impedance response for the entire micro-nanochannel integrated system, with the microchannel length  $L_m = 3 \mu m$  and  $H_m = 500 nm$ .  $R_D$  is obtained by measuring the width of the diffusional arc, while,  $R_2$ ,  $CPE_2$  and  $n_2$  are obtained by fitting the overall impedance spectrum. All the values are tabulated in Table 2.2. The values are substituted in Eq. 2.6 and is normalized with  $\left( \frac{RT}{F^2 z^2 D c_0} \right)$ . A comparison between the computational results (shown as circles) and the equivalent circuit model (shown as solid line) give fairly good agreement with each other as shown by the Nyquist plot (view Figure 2.5(c)) and the Bode phase plot (see Figure 2.5(d)). Also, the same model provides reasonably good match in the Ohmic regime. However, in the limiting resistance regime, owing to the presence of induced space charges the model fails to predict an additional resistance-capacitance arc. To overcome this, we considered an additional (R||CPE) circuit element in series with the previous model as shown in Figure 2.6(a) for a DC bias,  $\phi_{DC} Fz / RT = 77.3677$ . The new circuit model provides a reasonable agreement with the computational simulations as shown in Figure 2.6(b)). Furthermore, the multiple phase shift maximum at different frequencies is qualitatively captured as shown in Figure 2.6(c)). The relevant parameters used in the model are tabulated in Table 2.2.

An equivalent circuit to characterize the complex overlimiting behavior is beyond the scope of the present work. We provide the additional theoretical discussion and the supporting results in the following conjectured section.

## 2.6 Area-averaged multi-ion transport model

### (AAM)

We consider 2-D Poisson-Nernst-Planck equations to describe the nonlinear ionic transport in a micro-nanochannel interconnect system. We assume ideal non-polarizable electrodes and hence, neglect the Faradaic reactions that occur near the electrode in the present study. Further, we assume that the ions inside the Steric layer are rigidly held and do not contribute to the ionic current. We also assume an isotropic medium with a constant dielectric permittivity,  $\epsilon = \epsilon_0 \epsilon_r$ .  $\epsilon_0$  is the permittivity of free space and  $\epsilon_r$  is the relative permittivity of the medium. Under these assumptions, the mass transfer of each buffer species is given by,

$$\frac{\partial c_{\pm}}{\partial t} = -\nabla \cdot \mathbf{\Gamma}_{\pm} \quad (2.7)$$

where  $\mathbf{\Gamma}_{\pm}$  is the total flux of each species in the solution,

$$\mathbf{\Gamma}_{\pm} = -D_{\pm} \nabla c_{\pm} - \Omega_{\pm} z_{\pm} F c_{\pm} \nabla \phi \quad (2.8)$$

where  $D_{\pm}$ ,  $c_{\pm}$  and  $z_{\pm}$  denote the diffusion coefficient, molar concentration, and valence of cation and anion, respectively.  $\Omega_{\pm}$  is the ionic mobility which is related to the diffusion coefficient of the ionic species by Einstein's relation,  $\Omega_{\pm} = \frac{D_{\pm}}{RT}$ . The electric potential is represented by  $\phi$ . Other constants  $F$ ,  $R$ , and  $T$  represent Faraday's constant, ideal gas constant and absolute thermodynamic temperature, respectively. Integrating Eq. 2.7 over

the  $y$ -direction, the transport of cations in the axial direction can be calculated as,

$$\begin{aligned} \int_{-h/2}^{h/2} \left( \frac{\partial c_+}{\partial t} \right) dy &= \int_{-h/2}^{h/2} \left[ \frac{\partial}{\partial x} \left( D_+ \frac{\partial c_+}{\partial x} \right) + \frac{\partial}{\partial y} \left( D_+ \frac{\partial c_+}{\partial y} \right) \right] dy \\ &+ \int_{-h/2}^{h/2} \left[ \frac{\partial}{\partial x} \left( \frac{z_+ D_+ F}{RT} c_+ \frac{\partial \phi}{\partial x} \right) + \frac{\partial}{\partial y} \left( \frac{z_+ D_+ F}{RT} c_+ \frac{\partial \phi}{\partial y} \right) \right] dy \end{aligned} \quad (2.9)$$

$h$  is the height varying along the axial direction to represent the microchannel and the nanochannel, respectively. Considering there is no leakage of cationic current at the channel walls, the normal flux of cations on the channel walls is assumed to be zero,

$$\mathbf{n}_w \cdot \mathbf{\Gamma}_+ \Big|_{y=\pm \frac{h}{2}} = -D_+ \frac{\partial c_+}{\partial y} \Big|_{y=\pm \frac{h}{2}} - \left( \frac{z_+ D_+ F}{RT} c_+ \frac{\partial \phi}{\partial y} \right) \Big|_{y=\pm \frac{h}{2}} = 0 \quad (2.10)$$

where  $\mathbf{n}_w$  denotes the unit normal vector (pointing outwards) to the channel surface. Substituting the above condition in Eq. 2.9, we obtain the reduced transport equation for the cations,

$$h(x) \frac{\partial \hat{c}_+}{\partial t} = \frac{\partial}{\partial x} \left( h(x) D_+ \frac{\partial \hat{c}_+}{\partial x} \right) + \frac{\partial}{\partial x} \left( \frac{z_+ D_+ F}{RT} h(x) \hat{c}_+ \frac{\partial \hat{\phi}}{\partial x} \right) \quad (2.11)$$

where  $\hat{\cdot} = \frac{1}{h} \int_{-h/2}^{h/2} (\cdot) dy$  denotes the area averaged quantity considering the width of the system to be unity. Similar procedure is followed to obtain the reduced transport equation for the anions,

$$h(x) \frac{\partial \hat{c}_-}{\partial t} = \frac{\partial}{\partial x} \left( h(x) D_- \frac{\partial \hat{c}_-}{\partial x} \right) + \frac{\partial}{\partial x} \left( \frac{z_- D_- F}{RT} h(x) \hat{c}_- \frac{\partial \hat{\phi}}{\partial x} \right) \quad (2.12)$$

We now consider the 2-D Poisson equation for the electric field distribution,

$$\nabla \cdot (\epsilon_r \nabla \phi) = -\frac{F}{\epsilon_0} (z_+ c_+ + z_- c_-) \quad (2.13)$$

Applying the charge conservation at the walls leads to the following electrostatic boundary condition,

$$\mathbf{n} \cdot \nabla \phi = \frac{\sigma}{\epsilon} \quad (2.14)$$

where  $\mathbf{n}$  denotes the unit normal vector (pointing outwards) to the wall surface and  $\sigma$  is the surface charge density of the walls. Integrating Eq. 2.13 over the  $y$ -direction and substituting the preceding boundary condition, we obtain the following modified electrostatic equation,

$$\frac{\partial}{\partial x} \left( h(x) \frac{\partial \hat{\phi}}{\partial x} \right) = -\frac{Fh(x)}{\epsilon} \left( z_+ \hat{c}_+ + z_- \hat{c}_- + \frac{2\sigma}{Fh(x)} \right) \quad (2.15)$$

where  $\sigma$  is the assumed fixed surface charge density on the walls of the channel. The fixed wall surface charge density distribution,  $\sigma(x)$ , is given by:

$$\sigma(x) = \begin{cases} \sigma_m, & 0 \leq x \leq L_m \\ \sigma_n, & L_m < x \leq L_m + L_n \\ \sigma_m, & L_m + L_n < x \leq 2L_m + L_n \end{cases} \quad (2.16)$$

where  $\sigma_m$  and  $\sigma_n$  denote the homogeneous charge distribution on the walls of the microchannel and nanochannel, respectively.  $L_m$  and  $L_n$  refer to the length of the microchannel and nanochannel, respectively. We discuss the necessary boundary conditions for the closure of the problem. We consider the microchannel on the top (see Figure 2.1(a)), as the source and is given a harmonic excitation with an amplitude ( $\phi_{AC}$ ) and an angular frequency ( $\omega$ ), along with a constant electric potential ( $\phi_{DC}$ ). We would like to note that, the AC perturbations are applied after the system reaches a steady-state with the DC bias. The microchannel on the bottom is considered as the drain and is grounded. The concentration of both the ions at the ends of the microchannel is assumed to be equal to the bulk ionic concentration. Thus, the boundary conditions at the ends of the source (Eq. (2.17)) and drain (Eq. (2.18))

microchannels are specified as:

$$\phi = \phi_{DC} + \phi_{AC} \sin(\omega t), \quad c_+ = c_- = c_o \quad (2.17)$$

$$\phi = 0, \quad c_+ = c_- = c_o \quad (2.18)$$

The total current density ( $\hat{\Gamma}_{tot}$ ) through the channel is calculated as,

$$\hat{\Gamma}_{tot} = F \left( z_+ \hat{\Gamma}_+ + z_- \hat{\Gamma}_- \right) + \epsilon \frac{\partial \hat{\mathbf{E}}}{\partial t} \quad (2.19)$$

The first term on the right represents the current density due to the ionic conduction effects, and the second term represents the displacement current density due to the rate of change of electric displacement field. Here,  $\mathbf{E} = -\nabla\phi$ , is the electric field. Though, the displacement current density is negligible in the DC conductivity simulations, they play a significant role illustrating the EDL charging and micro- and nanochannel capacitive effects during the impedance analysis. Further,  $\hat{\Gamma}_{\pm} = -D_{\pm} \frac{\partial \hat{c}_{\pm}}{\partial x} - \frac{z_{\pm} F D_{\pm}}{RT} \hat{c}_{\pm} \frac{\partial \hat{\phi}}{\partial x}$  is the total flux of the ionic species, contributed by a diffusive component resulting from the concentration gradient, and an electric migration component due to the electric field interaction with the ionic concentration. It is important to note that the calculated current density should be multiplied with the cross-sectional area of the channel to determine the actual current.

We scale the distance with the length of the microchannel ( $L_m$ ), time with the diffusion time scale ( $L_m^2/D$ ), concentration of the cation ( $c_+$ ) and anion ( $c_-$ ) with the bulk concentration of the electrolyte solution ( $c_0$ ), electric potential ( $\phi$ ) with  $\phi_0 = RT/Fz$ , surface charge density ( $\sigma$ ) with  $\sigma_0 = Fz c_0 L_m$ , and total current density ( $\Gamma_{tot}$ ) with  $\Gamma_0 = Fz D c_0 / L_m$ . In this work, a symmetric monovalent electrolyte ( $z_+ = -z_- = z$ ) like *KCl* is considered and we normalize the diffusion coefficient of each ionic species with the characteristic diffusion coefficient,  $D = 2 \times 10^{-9} \text{ m}^2/\text{s}$ . Applying these scaling variables, the transport of cations

(+), anions (−) and the electric field distribution in the dimensionless form can be written as:

$$h^* \frac{\partial \hat{c}_{\pm}^*}{\partial t^*} = \frac{\partial}{\partial x^*} \left( h^* D_{\pm}^* \frac{\partial \hat{c}_{\pm}^*}{\partial x^*} \right) \pm \frac{\partial}{\partial x^*} \left( D_{\pm}^* h^* \hat{c}_{\pm}^* \frac{\partial \hat{\phi}^*}{\partial x^*} \right) \quad (2.20)$$

$$\frac{\partial}{\partial x^*} \left( h^* \frac{\partial \hat{\phi}^*}{\partial x^*} \right) = -\frac{h^*}{2\beta^2} \left( \hat{c}_+^* - \hat{c}_-^* + \frac{2\sigma^*}{h^*} \right) \quad (2.21)$$

The total area-averaged current density ( $\hat{\Gamma}_{tot}^*$ ) through the channel in dimensionless form is given as,

$$\hat{\Gamma}_{tot}^* = [\hat{\Gamma}_+^* - \hat{\Gamma}_-^*] + 2\beta^2 \frac{\partial \hat{\mathbf{E}}^*}{\partial t^*} \quad (2.22)$$

The first term on the right represents the normalized area-averaged ionic current density and the second term represents the normalized area-averaged displacement current density. In the preceding equations, variables with superscript “\*” are the dimensionless variables. Here  $\beta = \lambda_D/L_m$  characterizes the effect of the electrolyte concentration in the system as the Debye length ( $\lambda_D = \sqrt{\epsilon_0 \epsilon_r RT/2F^2 z^2 c_0}$ ) determines the thickness of the EDL.  $\frac{\sigma^*}{h^*}$  characterizes the effect of the ratio of wall surface charge density to the channel cross-section. The solvers for the AAM model are developed and implemented using the finite volume method in OpenFOAM (Open Field Operation and Manipulation) version 1.6[<http://www.openfoam.com/>(2011)]. The electrophoretic terms in the modified PNP equations are discretized using second-order bounded NVD schemes[Toro(1999)] to avoid artificial oscillations and to ensure that the solution is bounded. All the Laplacian terms are discretized using second-order central differencing scheme. Second-order implicit time differencing scheme is used to discretize the variables in time. A finer mesh is introduced near the walls, at the entrance and exit of the nanochannel to resolve the features of electrical double layer. In order to validate the area averaged model, we consider the MNECS system of  $L_n = 5 \mu m$ ,  $H_n = 15 nm$ ,  $L_m = 6 \mu m$  and  $H_m = 500 nm$ . The bulk ionic concentration, and nanochannel wall surface charge density considered are  $c_0 = 0.1 mM$  and  $\sigma_n = -1 mC/m^2$ , respectively. Figure 2.7 shows the magnitude of nor-

malized current–voltage characteristics illustrating three different regimes, namely, Ohmic, limiting resistance (LRR) and overlimiting behavior using the AAM model (shown as solid line with symbols).

We observe that the results are in good agreement with the complete 2–D model (shown as triangles). We would also like to point out that, for a DC simulation in the non–Ohmic regime, the 2–D model requires 60 processors and around 7 hours of computational resources, while the area–averaged model performs the same simulation using 1 processor in approximately 3 hours. Also, for a typical small AC amplitude perturbation, say for a harmonic excitation of 1 *kHz* and  $c_0 = 0.1 \text{ mM}$ , at  $\phi_{DC}Fz/RT = 154.735$ , the 2–D model requires around 60 processors and 72 hours, while the AAM model uses 1 processor and requires around 7 hours.

## 2.7 Impedance calculation

In this section, we provide details on the conventions followed and the algorithm to calculate the complex impedance from the time dependent current signals, obtained from the computations. First, to describe any phase angle, we assume that the angle is bounded between 0 and  $2\pi$ . Note, owing to the coordinate system, and the direction of the applied electric field, the output current is multiplied by -1, before converting it into frequency domain. The other steps for the algorithm are provided below.

**Step 1:** Represent applied electric potential in complex form;

$$\phi(t) = \phi_{DC} + \phi_{AC} \sin(\omega t) = \phi_{DC} + \text{Re}(\phi_{AC} e^{j(\omega t + \theta_V)}) \quad (2.23)$$

where all the variables are defined earlier. Note,  $\theta_V = \frac{3\pi}{2}$ , from the convention used to represent angle.

**Step 2:** Represent output current (after multiplying it with -1) into complex form;

$$I(t) = I_{DC} + Re \left( I_{AC} e^{j(\omega t + \theta_I)} \right) \quad (2.24)$$

**Step 3:** Take fast Fourier Transform (FFT) using Matlab, of the output current (per unit width) measured at the end of the microchannel after the transients die out.

$$I_{fft} = fftshift(fft(I(n_{data}))) \quad (2.25)$$

where  $n_{data}$  is the number of data points considered for the FFT.

**Step 4:** Sample the frequency

$$f_s = -\frac{(n_{data} - 1)}{2} : \frac{(n_{data} - 1)}{2} / (\Delta t * (n_{data} - 1)) \quad (2.26)$$

where  $\Delta t$  is the time step used in the simulation between each current recording. In this study, we used  $N = 100$  data points to represent one time period,  $T_p$  (from which  $\Delta t = T_p/N$  can be calculated) for all the frequency excitations. Further, we used 10 periods ( $n_{data} = 1001$ ) to perform the FFT. We checked that ensuring the same  $N$  and  $n_{data}$  for all the frequency cases, ensures the same error propagation and hence, would not affect the physics of the problem.

**Step 5:** Determine  $|I_{AC}|$ ,

$$|I_{AC}| = \left( abs(I_{fft}(a_0)) * \frac{2}{(n_{data} - 1)} \right) \quad (2.27)$$

where  $a_0 = \frac{(n_{data}-1)}{2} + 1 + (f * \Delta t * (n_{data} - 1))$  represents the data point corresponding to the applied harmonic frequency ( $f$ ). Note that, FFT in Matlab rescales the data. Hence a rescaling factor  $\left( \frac{2}{(n_{data}-1)} \right)$  based on the number of data points is used to calculate the actual magnitude of the perturbed current.

**Step 6:** Determine the phase angle  $\theta_I$ , using angle function in Matlab on the FFT signal.

$$\theta_I = (\text{angle}(I_{fft}(a_0))) \quad (2.28)$$

The angle returned is in radians between  $-\pi$  to  $\pi$ . Hence, in order to be consistent with our earlier convention for measuring angle, we rescale the angle based on the following criteria:

$$\begin{aligned} \text{If } (\theta_I \geq 0) \quad \theta_I &= \theta_I \\ \text{else} \quad \theta_I &= \theta_I + 2\pi \end{aligned} \quad (2.29)$$

**Step 7:** Using  $|I_{AC}|$  and  $\theta_I$ , calculate the complex impedance ( $Z(\omega)$ ) from the following expression:

$$Z(\omega) = |Z_0|e^{j\theta_z} \quad (2.30)$$

where  $|Z_0| = \frac{|\phi_{AC}^*|}{|I_{AC}^*|}$  is the magnitude of the normalized electrochemical impedance, considering the normalized perturbed potential,  $\phi_{AC}^* = \phi_{AC}Fz/RT$ , and the normalized perturbed current per unit width,  $I_{AC}^* = I_{AC}/FzDc_0$ .  $\theta_z = \theta_V - \theta_I$  is the relative phase difference between the applied electric potential and the perturbing current, and  $j = \sqrt{-1}$  is the imaginary unit.

## 2.8 Characterization of DBL thickness

Figure 2.8(a) shows the impedance spectrum when the microchannel geometry is not considered in the model. The impedance spectrum features a perfect semicircle illustrating a single relaxation time constant with characteristic frequency  $f_n$ , corresponding to the electric migration effects inside the nanochannel. The absence of the diffusion boundary layer outside the nanochannel results in the absence of the diffusional arc. The spectrum for a

3  $\mu m$  length microchannel is presented in Figure 2.8(b). The amplitude of the diffusional arc becomes significant compared to the former case, owing to the DBL effects. We observe a linear scaling of  $\chi = \frac{Im(Z)|_{f_D}}{Im(Z)|_{f_n}}$ , with respect to the increase in the microchannel length. Also, we observe that the diffusion frequency ( $f_D = 90 Hz$ ) has increased compared to the larger microchannel length of ( $L_m = 6 \mu m$ ) for the same concentration case. The results are consistent with the expression for  $f_D$  (refer main text) which shows an inverse quadratic scaling with the DBL length. These results further confirm that the DBL thickness can be accurately characterized from the impedance response.

The DC and first harmonic contribution of total concentration,  $C_0$  and  $C_1$  are normalized by the bulk ionic concentration  $c_0$ . Similarly the field,  $\phi_{x_0}$  and  $\phi_{x_1}$  are normalized by  $\phi_0/L_m$ .  $a_1$  and  $b_1$  are normalized by  $FzDc_0$ .  $\theta_I$  is calculated using ‘atan2’ function in Matlab, in order to ensure that the calculated angle represents the right quadrant,  $\theta_I = atan2(b1, a1)$ . The angle returned is in radians between  $-\pi$  to  $\pi$ . In order to be consistent with our earlier convention for measuring angle, we rescale the angle using Eq. 2.29.

## 2.9 AC rectification effects

We extend our study and probe the limiting resistance regime, with the magnitude of AC perturbation comparable to the DC bias, and briefly discuss the current characteristics. We understand the frequency effects for a constant applied DC bias,  $\phi_{DC}Fz/RT = 154.735$ , while the AC amplitude is  $\phi_{AC}Fz/RT = 232.1032$  at  $\beta = 5.1334 \times 10^{-3}$ . The effect of the combined AC/DC electric field on the current characteristics is investigated by time averaging the current (per unit width) measured at the end of the source microchannel over one time period ( $T_p$ ):

$$\langle \mathbf{I} \rangle = \frac{1}{T_p} \int_0^{T_p} \mathbf{I} dt \quad (2.31)$$

Figure 2.11 shows the relative current rectification behavior as a function of normalized frequency. The relative current rectification is calculated as:

$$\frac{\Delta \mathbf{I}}{\mathbf{I}_{DC}} = \frac{\langle \mathbf{I} \rangle - \mathbf{I}_{DC}}{\mathbf{I}_{DC}} \quad (2.32)$$

where  $\mathbf{I}_{DC}$  is the current (per unit width) obtained when only DC voltage is applied and  $\langle \mathbf{I} \rangle$  is the time averaged current (per unit width) under combined AC/DC electric field computed using Eq. (2.31). Figure 2.11 shows that at low frequencies the transport is suppressed resulting in a negative current rectification with the application of a harmonic field. However, with the increase in the frequency we observe anomalous positive current rectification with enhancements in the current. A maximum positive current rectification is observed at  $fL_m^2/D = 720$ , while a further increase in the frequency leads to a decrease in the rectification effect. Also, at a very high frequency ( $fL_m^2/D = 9000$ ), we again observe a negative current rectification effect. However the relative rectification is almost minimal at this frequency regime. The reason for these rectification effects and its scaling with the AC amplitude is discussed elsewhere. We briefly highlight the physical mechanism here. First, with the application of an AC amplitude, whose magnitude is comparable to the DC bias, we observe higher harmonic excitations in the output current. Figure 2.12(a) shows the harmonic oscillations of the output current signal for a normalized frequency  $fL_m^2/D = 0.36$ . The corresponding Fourier spectrum demonstrating the higher harmonic modes is shown in Figure 2.12(b). The current oscillations and its corresponding Fourier spectrum for a different frequency  $fL_m^2/D = 18$  is shown in Figure 2.12(c) and Figure 2.12(d), respectively. The presence of even and odd harmonic modes shown in the Fourier spectrum due to AC bias, introduces another symmetry breaking in the system, in addition to the symmetry breaking observed due to the DC bias. We define it as ‘‘AC symmetry breaking’’. Second, under different harmonic excitations, the relative phase difference between the harmonic contributions of the total ionic concentration and the electric field in the space charge region,

govern the electrophoretic interactions and hence, the averaged output conduction current.

Owing to the AC symmetry breaking, the impedance spectroscopy can not be used to observe the rectification effects. However, we would like to comment that the important time scales under which the positive and negative rectification may occur, can be predicted from the spectra. Figure 2.11 shows that under low frequencies the negative rectification effect reaches a maximum approximately at a characteristic frequency corresponding to diffusion frequency,  $f_D$  determined from the impedance spectra under the same DC bias (see Figure 2.4(b)). Also, the transition from the negative to positive rectification occurs approximately at frequencies greater than  $f_I$ . Finally, the frequency ( $fL_m^2/D = 18000$ ) at which the maximum negative rectification occurs in the high frequency regime is determined by the characteristic frequency ( $f_n$ ) governing the nanochannel transport.

## 2.10 Conclusions

To summarize, a computational impedance spectroscopic technique (CIS) is developed to characterize the fundamental electrochemical properties of a micro–nanochannel integrated system using an area–averaged multi–ion transport model. The technique is used to investigate the ion transport dynamics with and without the influence of external DC bias. Under no external DC bias and in the Ohmic regime, we observed two distinct arcs with four different characteristic frequencies. The low frequency diffusional arc characterizes the diffusion–transport and the EDL charging effects at the interface of the micro–nanochannel, while the high frequency geometric arc characterizes the electric migration and displacement current effects inside the microchannel and in the nanochannel. An additional resistance–capacitance (RC) arc with a new characteristic frequency  $f_m$  is observed in the LRR regime. The presence of induced space charges in the depletion microchannel was attributed to these effects. Further, an anomalous inductive arc at low frequencies ( $fL_m^2/D \leq 1$ ) was observed in the overlimiting regime. The origin of this arc was attributed to the phase effects between

the harmonic disturbance of the total ionic concentration and the electric field in the induced space charge region. The presence of an anomalous inductive arc provides an opportunity to distinguish the LRR and overlimiting region. Furthermore, in the Ohmic and in the LRR regimes, the impedance spectra helps us to characterize the microscopic length of the diffusion boundary layer (DBL) and the space charge region (SCR). Using the impedance spectra, we also highlight the important time scales at which negative and positive AC rectification effects are observed in the system. Finally, equivalent circuit models are designed to interpret the impedance response.

## 2.11 Tables

Table 2.1: Effect of bulk ionic concentration on the impedance spectra corresponding to diffusion and nanochannel characteristic frequencies,  $\chi = \frac{Im(Z)|_{f_D}}{Im(Z)|_{f_n}}$

$c_0$ (mM)	$\beta(\times 10^{-3})$	$\chi$
0.01	16.235	2.3787
0.1	5.1334	0.2408
1	1.6235	0.0623

Table 2.2: Fitting parameters for the circuit model under no external DC bias and under limiting resistance regime

<b>Parameters</b>	<b>No DC</b>	$\phi_{DC}Fz/RT = 77.3677$
$R_1 (k\Omega m)$	32.429	27
$R_2(k\Omega m)$	3.8	175
$R_3(k\Omega m)$	NA	120
$CPE_1$	4.482e-12	5.8086e-12
$CPE_2$	2.3611e-10	1.6e-10
$CPE_3$	NA	14e-9
$n_1$	1	1
$n_2$	0.97	1
$n_3$	NA	1
$R_D (k\Omega m)$	3.8	940
$\tau_D (ms)$	4.5	12.1

Table 2.3: Parameters of normalized DC and first harmonic contribution of total concentration and field, for a DC bias of  $\phi^{DC}Fz/RT = 773.677$ , corresponding to the overlimiting regime.

$fL_m^2/D$	$C_0^*$ ( $\times 10^{-2}$ )	$\phi_{x_0}^*$	$C_1^*$ ( $\times 10^{-5}$ )	$\phi_{x_1}^*$	$\theta_1$ (radians)	$\phi_1$ (radians)	$a_1^*$ ( $\times 10^{-4}$ )	$b_1^*$ ( $\times 10^{-3}$ )	$\theta_I$ (radians)
0.09	2.5	346.205	4.984	0.9566	4.627	4.7445	-1.189	-6.799	4.6949
0.18	2.5	346.205	4.685	0.9569	4.5327	4.745	-3.548	-6.595	4.6587
0.36	2.5	346.205	3.953	0.9576	4.4404	4.7456	-4.818	-6.135	4.634
0.9	2.5	346.205	2.839	0.9587	4.5866	4.7463	-0.7192	-5.568	4.6995
1.2	2.5	346.205	2.719	0.959	4.7152	4.7466	1.395	-5.512	4.7377
1.44	2.5	346.205	2.728	0.9593	4.8024	4.7469	2.775	-5.511	4.7627
3.6	2.5	346.205	3.583	0.9619	5.0637	4.7484	8.541	-5.896	4.856

Table 2.4: Parameters of normalized DC and first harmonic contribution of total concentration and field, for a DC bias of  $\phi^{DC} Fz/RT = 77.3677$ , corresponding to the LRR regime.

$fL_m^2/D$	$C_0^*$ ( $\times 10^{-2}$ )	$\phi_{x0}^*$	$C_1^*$ ( $\times 10^{-3}$ )	$\phi_{x1}^*$	$\theta_1$ (radians)	$\phi_1$ (radians)	$a_1^*$ ( $\times 10^{-3}$ )	$b_1^*$ ( $\times 10^{-3}$ )	$\theta_I$ (radians)
0.09	3.6	73.01	1.716	4.051	1.6349	4.7963	0.7014	-3.394	4.916
0.18	3.6	73.01	1.712	4.045	1.5412	4.7232	0.8779	-3.46	4.961
0.36	3.6	73.01	1.694	4.025	1.4803	4.7035	1.649	-3.629	5.139
0.9	3.6	73.01	1.578	3.911	1.3236	4.6575	3.409	-4.825	5.328
1.2	3.6	73.01	1.499	3.838	1.2596	4.6413	3.949	-5.612	5.326
1.44	3.6	73.01	1.438	3.783	1.2189	4.6322	4.214	-6.196	5.309
3.6	3.6	73.01	1.109	3.479	1.0308	4.6027	4.659	-9.162	5.183

## 2.12 Figures

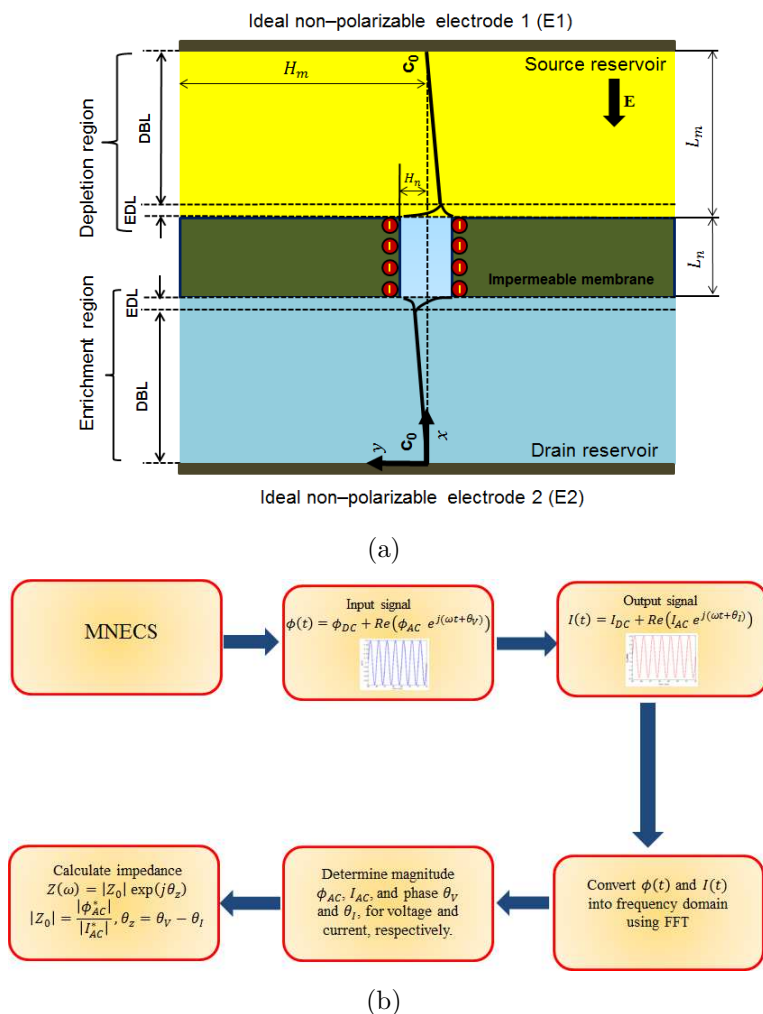


Figure 2.1: (a) A canonical hybrid micro–nanochannel integrated electrochemical system (MNECS). The bold line displays the ionic concentration distribution indicating the enrichment and depletion electroneutral diffusion boundary layer (DBL) under Ohmic regime. A thin quasi–equilibrium EDL developed on both sides near the micro–nanochannel interface is also shown.  $c_0$  refers to the bulk ionic concentration at the ends of the microchannel. (b) Flow chart to characterize the electrochemical properties of MNECS.

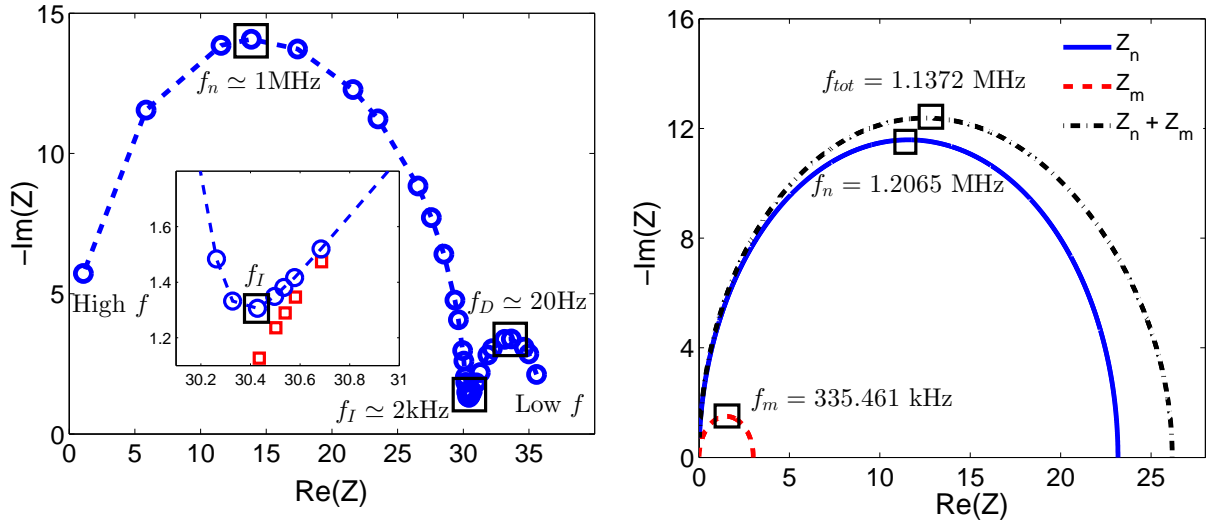


Figure 2.2: (a) Impedance spectra (Nyquist plot) for a bulk ionic concentration  $c_0 = 0.1\text{ mM}$ , corresponding to  $\beta = 5.1334 \times 10^{-3}$ , under no external DC bias. The inset of Figure 2.2(a) shows a comparison of impedance spectra with (dashed line with symbols) and without (open squares) the displacement current effects, near the characteristic frequency,  $f_I$ . (b) Analytical impedance response of a microchannel (dashed line), nanochannel (solid line) and their combined response (dash dot–line).

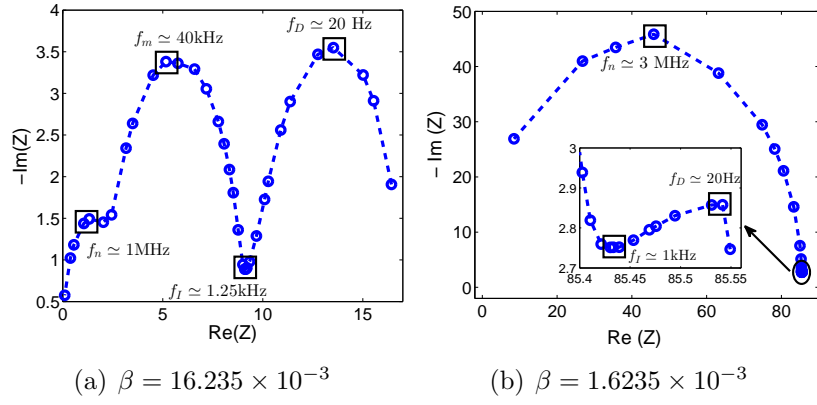
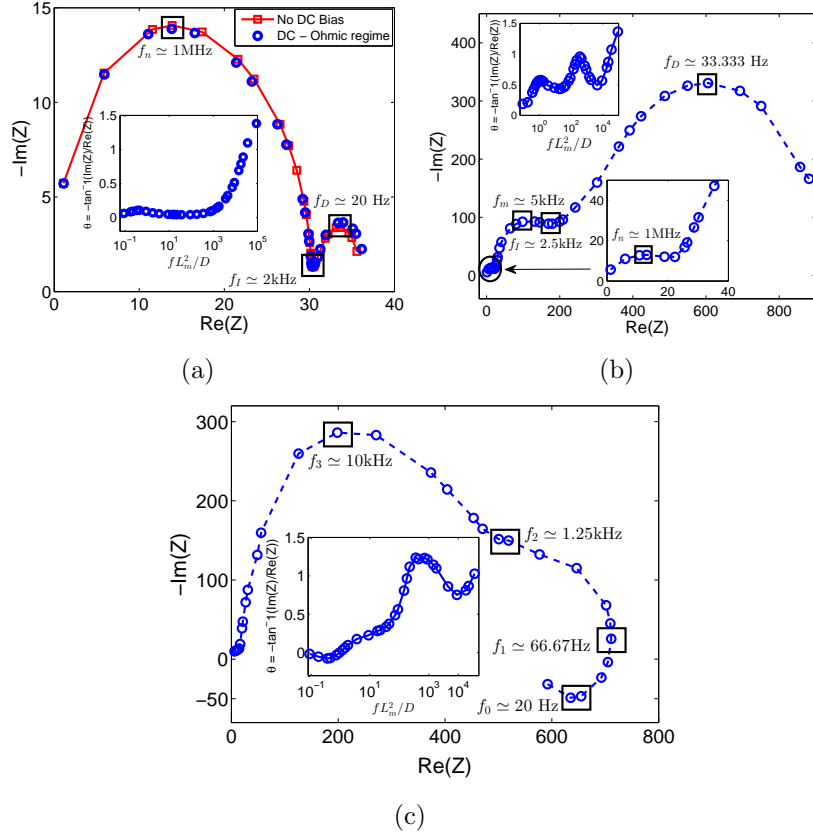


Figure 2.3: Impedance spectra (Nyquist plot) for different dimensionless electrolyte concentration ( $\beta$ ), under no external DC bias. The inset of Figure 2.3(b) shows the small diffusional arc in the low frequency regime.



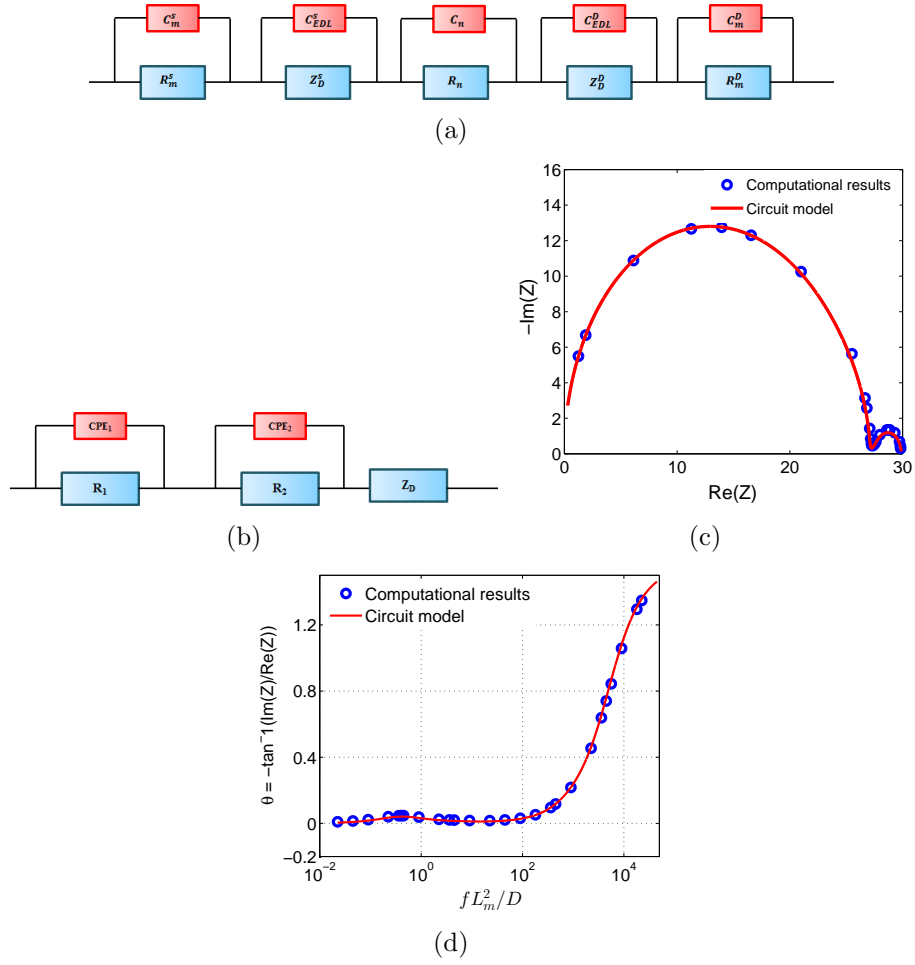


Figure 2.5: (a) A physically consistent equivalent circuit model. (b) modified circuit model. Comparison of (c) computational impedance spectra, (circles) and (d) Bode phase plot results, (circles) with the equivalent circuit model (solid line) under no external DC bias at  $\beta = 5.1334 \times 10^{-3}$ , and  $L_m = 3 \mu m$ .

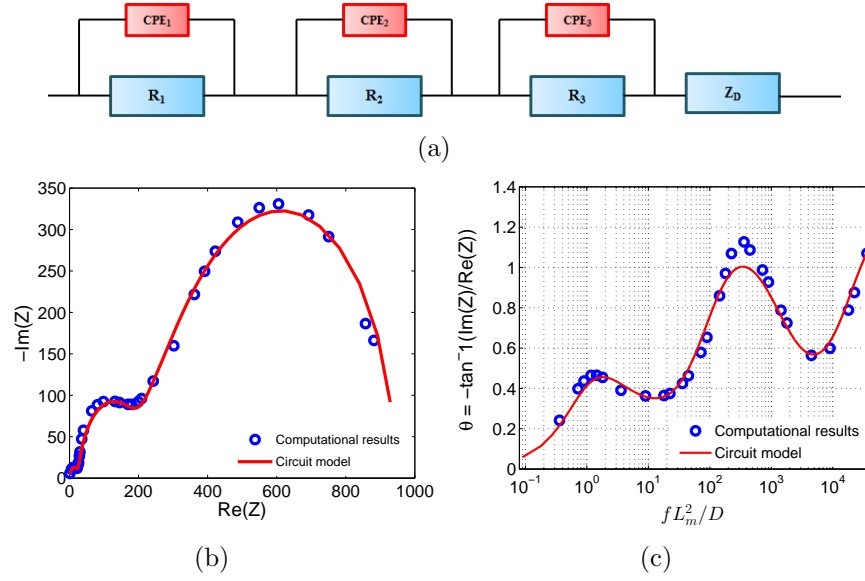


Figure 2.6: (a) An equivalent circuit model. Comparison of (b) computational impedance spectra, (circles) and (c) Bode phase plot results, (circles) with the equivalent circuit model (solid line) under limiting resistance regime ( $\phi_{DC}Fz/RT = 77.3677$ ) at  $\beta = 5.1334 \times 10^{-3}$ , and  $L_m = 6 \mu m$ .

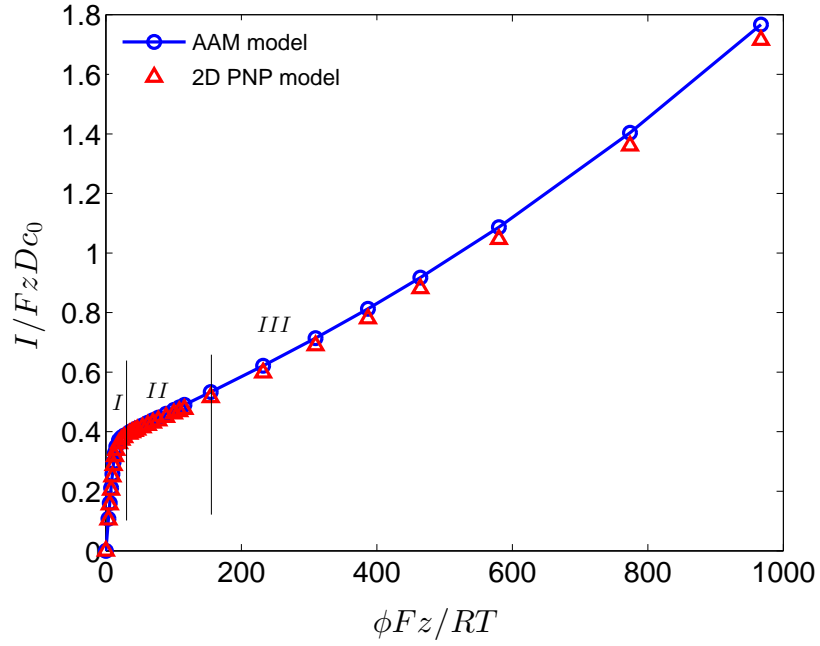


Figure 2.7: Comparison of normalized current–voltage characteristics (in magnitude) between AAM model (line with symbols) and 2–D PNP model (triangles) of a MNECS at  $\beta = 5.1334 \times 10^{-3}$ . Region I corresponds to the Ohmic region, II represents the limiting resistance region (LRR) and region III corresponds to the overlimiting region.

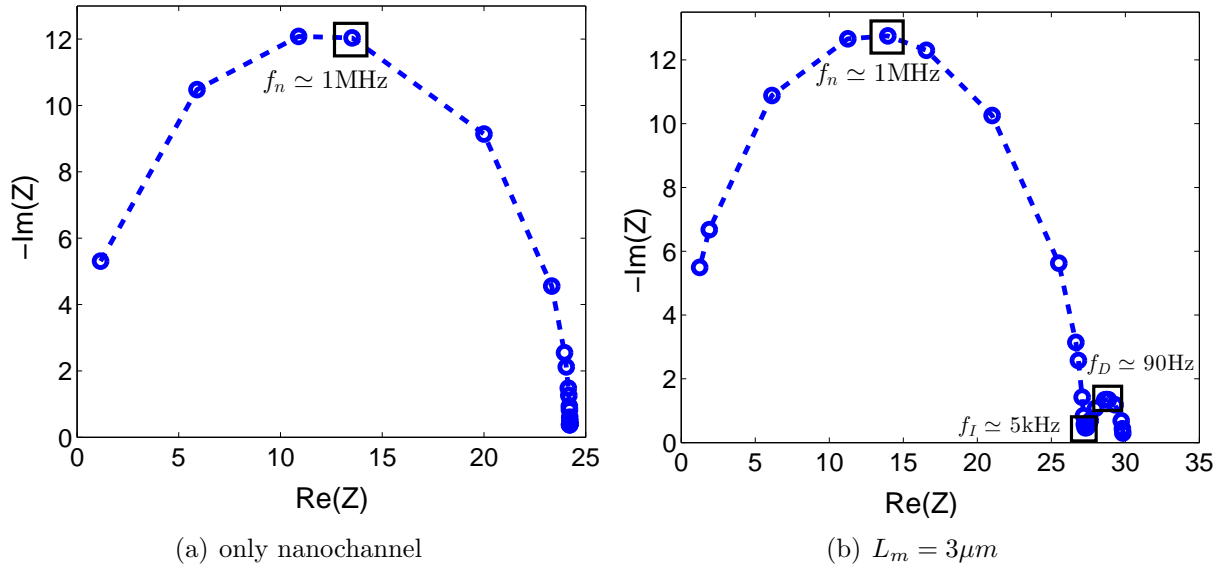


Figure 2.8: Impedance spectra for different length of the microchannel to illustrate the DBL effect at a constant  $\beta = 5.1334 \times 10^{-3}$  and under no external DC bias.

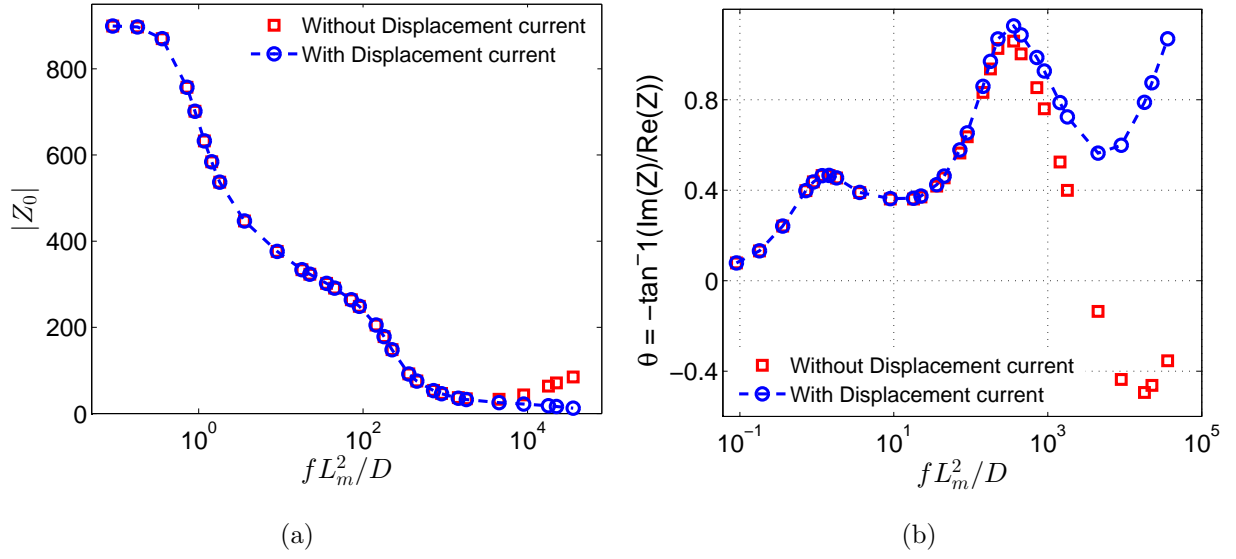


Figure 2.9: Comparison of (a) normalized Bode magnitude plot and (b) Bode phase plot with (line with symbols), and without (open squares) the displacement current density at a DC bias,  $\phi_{DC} Fz/RT = 154.735$ , corresponding to LRR.

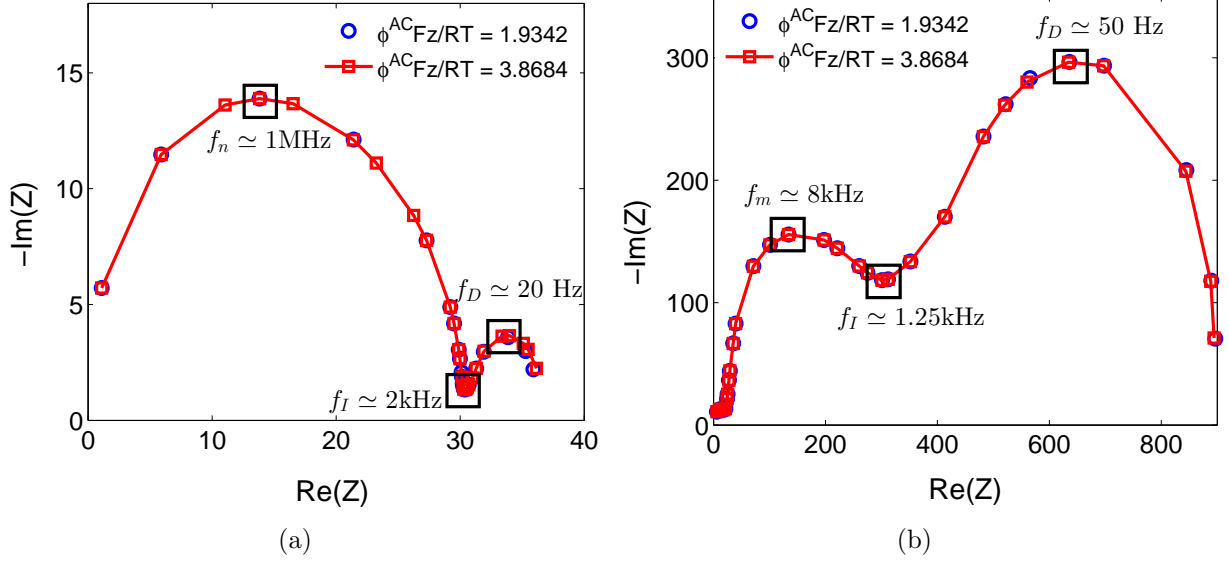


Figure 2.10: Impedance spectra for different small amplitude AC bias at  $\beta = 5.1334 \times 10^{-3}$ ,  $\phi_{AC} Fz/RT = 1.9342$  (circles) and  $\phi_{AC} Fz/RT = 3.8684$  (line with symbols) at DC bias (a)  $\phi_{DC} Fz/RT = 3.8684$ , corresponding to Ohmic regime, and (b)  $\phi_{DC} Fz/RT = 154.735$ , corresponding to LRR. The results ensure consistent impedance spectra independent of small amplitude AC perturbation.



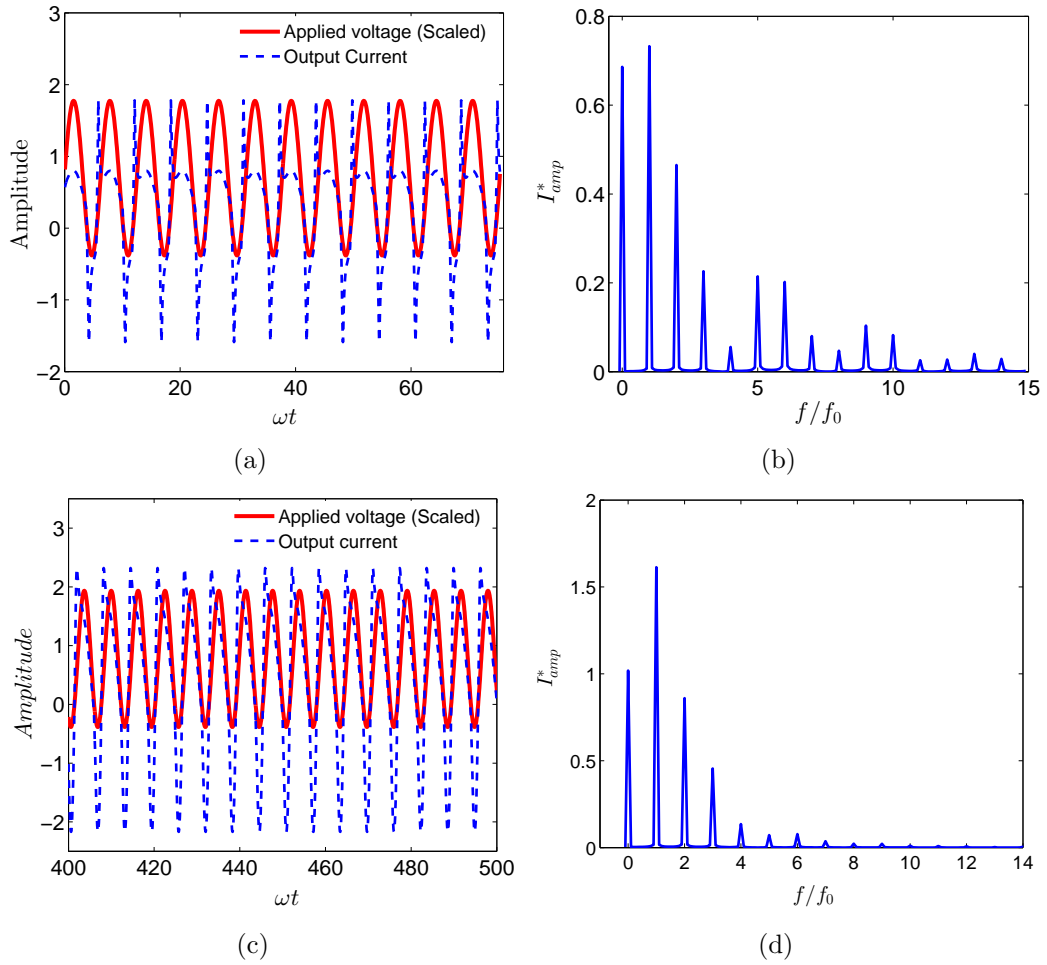


Figure 2.12: (a) Complex current oscillations (dashed line) and (b) corresponding Fourier spectrum at  $fL_m^2/D = 0.36$ . (c) Current oscillations (dashed line) and (d) corresponding Fourier spectrum, at  $fL_m^2/D = 18$ . Applied DC bias  $\phi_{DC}Fz/RT = 154.735$  and AC bias  $\phi_{AC}Fz/RT = 232.1032$  at  $\beta = 5.1334 \times 10^{-3}$ . The even and odd harmonic modes in the spectrum indicate AC symmetry breaking.

## 2.13 References

1. [Dekker(2007)] C. Dekker, *Nat. Nanotechnol.* 2 (2007) 209215.
2. [Krems and et al.(2010)] M. Krems, et al., *Nano Lett.* 10 (2010) 26742678.
3. [Siwy and et al.(2002)] Z. Siwy, et al., *Phys. Rev. Lett.* 89 (2002) 198103.
4. [Schoch and et al.(2008)] R. B. Schoch, et al., *Rev. Mod. Phys.* 80 (2008) 839883.
5. [Howorka and et al.(2009)] S. Howorka, et al., *Chem. Soc. Rev.* 38 (2009) 23602384
6. [Saleh and et al.(2003)] O. A. Saleh, et al., *Nano Lett.* 3 (2003) 3738.
7. [Chen and et al.(2010)] Z. Chen, et al., *Nat. Mater.* 9 (2010) 667675.
8. [Kasianowicz and et al.(1996)] J. J. Kasianowicz, et al., *Proc. Natl. Acad. Sci.* 93 (1996) 1377013773.
9. [Chang and et al.(2008)] G. Yossifon, et al., *Phys. Rev. E* 79 (2009) 046305.
10. [Piruska and et al.(2010)] A. Piruska, et al., *Chem. Soc. Rev.* 39 (2010) 10601072.
11. [Kim and et al.(2007)]S. J. Kim, et al., *Phys. Rev. Lett.* 99 (2007) 044501.
12. [Jin and et al.(2007)]X. Jin, et al., *Langmuir* 23 (2007) 1320913222.
13. [Postler and et al.(2008)]T. Postler, et al., *J. Colloid Interface Sci.* 320 (2008) 321332.
14. [Choi and et al.(2009)]Y. S. Choi, et al., *J. Colloid Interface Sci.* 333 (2009) 672678.
15. [Pu and et al.(2004)] Q. Pu, et al., *Nano Lett.* 4 (2004) 10991103.
16. [Mani and et al.(2009)]A. Mani, et al., *Langmuir* 25 (2009) 38983908.
17. [Zangle and et al.(2009)] T. A. Zangle, et al., *Langmuir* 25 (2009) 3909.
18. [Kim and et al.(2010)] S. J. Kim, et al., *Nat. Nanotechnol.* 5 (2010) 297301.

19. [Yossifon and et al.(2008)] G. Yossifon, et al., Phys. Rev. Lett. 101 (2008) 254501.
20. [Barsoukov and et al.(2005)] E. Barsoukov, et al., Impedance spectroscopy: Theory, Experiment and Applications, Wiley: Hoboken, New Jersey, NJ, 2nd edition, 2005.
21. [Frigo and et al.(1998)] M. Frigo, et al., Proceedings of the International Conference on Acoustics, Speech, and Signal Processing 3 (1998) 13811384.
22. [Hille(2001)]B. Hille, Ion Channels of Excitable Membranes, Sinauer Associates Inc., Sunderland, MA, 3rd edition, 2001.
23. [Rubinstein and et al.(2009)] I. Rubinstein, et al., Phys. Rev. E. 80 (2009) 021505.
24. [Jacobsen and et al.(1995)] T. Jacobsen, et al., Electrochimica Acta 40 (1995) 255262.
25. [Diard and et al.(1999)] J. P. Diard, et al., J. Electroanal. Chem. 471 (1999) 126131.
26. [Staude and et al.(1988)]I. Rubinstein, et al., Desalination 69 (1988) 101114.
27. [Toro(1999)] E. F. Toro, Riemann Solvers and Numerical Methods for Fluid Dynamics, SpringerVerlag, 1999.
28. [<http://www.openfoam.com/>(2011)] <http://www.openfoam.com/>, 2011.

# Chapter 3

## Controlling the Ionic Current Rectification Factor of a Nanofluidic/Microfluidic Interface with Symmetric Nanocapillary Interconnects

### 3.1 Abstract

The current rectification factor can be tailored by changing the degree of asymmetry between the fluidic channels on opposite sides of a nanocapillary membrane (NCM). A symmetric device with symmetric fluid baths connected to opposite sides of the NCM did not rectify ionic current; while a NCM connected between fluid baths with a 32-fold difference in cross-sectional area produced a rectification factor of 75. The data suggests that the primary mechanism for the current rectification is the change in cross-sectional area of the microchannels and the polarity dependent propagation of the enriched and depleted concentration polarization (CP) zones into these regions. Secondary contributions to the increasing rectification factor with increasing bath asymmetry appear to be a result of increased ionic density near the enriched micropore along with electroconvection in the macropore, with inside diameters (IDs) of 625 and 850 –  $\mu\text{m}$ . Evidence for electroconvection is provided by the power spectral density (PSD) analysis of the I-t data that reveals chaotic oscillations for devices with 625 and 850 –  $\mu\text{m}$  ID reservoirs. In the ON state, current rectification keeps ionic transport toward the NCM high, increasing the speed of processes like sample enrichment. A simple means is provided to fabricate fluidic diodes with tailored current rectification factors.

## 3.2 Introduction

Ionic current rectification is an important process in the function of biological ion pores, and it can provide enhanced functionality to microfluidic and nanofluidic systems. Ionic current rectification can be used to create diodes for fluidic circuits [Howorka et al.(2009)], Chen et al.(2010), Z. Chen et al.and Piruska et al.(2010)], and has been used in analyte enrichment [Pu et al.(2004), Yuan et al.(2007),] and desalination [Qiao et al.(2005)]. Current rectification produces a greater flow of current in one direction than in the opposite direction, and the current-voltage (I-V) plot of a rectifier exhibits a characteristic asymmetric shape. The current rectification factor is the ratio of the forward bias or ON state current to the reverse bias or OFF state current. Ionic current rectification in fluidic systems was initially observed with systems that are asymmetric at the nanoscale. More recently, devices with heterogeneous solutions on opposite sides of a membrane have achieved ionic current rectification using membranes with both nanoscale and microscale pores. Current rectification has also been observed in a fluidic system with the symmetric nanochannels filled with a homogeneous solution, providing evidence that current rectification can be achieved without nanoscale asymmetry or the use of heterogeneous solutions. Conical nanopores are an example of nanofluidic elements with asymmetric geometry that rectify ionic current. Typically, conically shaped pores have a diameter on the nanoscale on the narrow side (the tip) and a larger diameter on the wide side (the base). For a conical nanopore with a charged surface, counterion transport is enhanced in the tip to base direction, which forms the current rectification. The pioneering work on ionic current rectification is to characterize the ion transport through conical quartz nanopipettes. In addition, asymmetric nanochannels made like funnels also rectify ionic current, and the effect of the taper angle of the nanofluidic funnel to the current rectification ratio has been investigated. Several groups have focused on how to control the current rectification of the conical nanopore. It has been reported that the degree of current rectification can be affected by the diameter of the conical pore, and

ionic current rectification increases with decreasing tip diameter. The surface charge inside the nanopore plays a critical role in the ionic current rectification, and the effects of changing the solution have been investigated. Changing the sign of the surface charge from negative to positive, reverses the direction of the current rectification. Typically, layer-by-layer deposition of polyelectrolytes into a conical pore is set forth to tune the current rectification ratio. In a further refinement, a pH-responsive polymer brush was used to create a rectifier that can be controlled by the solution properties. In addition to using asymmetric geometry, nanochannels with asymmetric surface charge can rectify ionic current and form nanofluidic diodes. In this scenario, the nanochannel is postulated with asymmetric or discontinuous surface charge. In these devices, ON state currents are produced when a forward-bias produces an ion enriched zone in the nanochannel, and the OFF state currents are produced when a reverse-bias causes formation of an ion depletion zone in the nanochannel. To produce surface charge discontinuity, the nanochannel surface is diffusion limited patterned (DLP). Half of the nanochannel encapsulated with biotin, which imparts a neutral charge on the surface; while avidin is bound to the other half of the nanochannel, which imparts a positive charge. The other heterogeneous surface asymmetry configuration includes surface coatings with  $SiO_2/Al_2O_3$  heterostructured nanotubes to form nanofluidic diodes. In a related approach, photolithography can be put forth to create nanochannels with  $SiO_2$  and  $Al_2O_3$  that had a much sharper charge boundary than the DLP process to create triodes. To actively control the current rectification and ion transport in gated transistors, an external field was applied to change the local surface charge density of the nanofluidic diode. For example, a single asymmetrically placed gate electrode or dual split-gate electrodes onto the top of the nanochannel can be triggered to form the field-effect reconfigurable nanofluidic diodes. Aliter configuration manifests in geometrical modification of the nanopore (introducing conical nanopore) in combination with differential surface coatings to boost the current rectification factors. Ionic current rectification is projection in this chapter with the manifestation of cross-sectional asymmetry in the external microporous environment leveraged

with a symmetric nanopore architecture, confirming that ionic current rectification is not exclusively the result of nanoscale asymmetry. The system triggers asymmetric propagation of enriched and depletion induced charges at the micro-nanoporous junctions owing to concentration polarization (CP) modality. The asymmetry of the fluidic system is proposed to alter the length and stability of the CP depleted and enriched zones. The low current or OFF state is observed when the CP depleted zone is in the micropore and the high current or ON state is observed when the CP enriched zone is in the micropore. Although physically distinct, all of these systems produce ionic current rectification by creating a potential barrier that is caused by the formation of a CP ion depleted zone, yielding low off state currents. In the case of the conical nanopores and nanopores with asymmetric surface charge, the CP depleted zone forms inside the nanopore while the CP depleted zone forms at the nanocapillary/micropore interface (NMI) for the devices with asymmetric baths. Herein, the asymmetry of the NMI is systematically altered by varying the ID of the larger fluid bath or macropore, and the current rectification factor increases as the macropore ID increases. As the asymmetry in cross-sectional area of the micro- and macropores on opposite sides of the NCM increases, the difference in conductivity of these two regions increases, which in turn affects the current rectification factors. The combination of the different cross-sectional areas and the extension of the ion depleted and enriched CP zones into these regions plays an important role in creating the current rectification and in determining its magnitude. Additionally, as the ID of the macropore is increased the propensity for convection increases as well. Therefore, contributions to the current rectification by electroconvection [Kim et al.(2007), Yossifon et al.(2008), Chang et al.(2008) and Rubinstein et al.(2009)] are also considered, and the noise in the current-time signal is analyzed to provide evidence for the possible existence of convective processes. The data provides a new approach to tune the current rectification of NMIs and strengthen the fundamental knowledge of current rectification mechanism in these devices. It is anticipated that this knowledge will be applied to improve analyte enrichment, ionic purification processes, and the fabrication of simple

fluidic diodes.

### 3.3 Results and Discussion

Current rectification is confirmed in a NMI fabricated with a nanocapillary membrane (NCM) having symmetric nanocapillaries with symmetric and asymmetric microporous environments (view Figure 3.1). Current rectification is observed when there is asymmetry in the fluidic system to which the nanocapillaries are connected. For example, current rectification is observed when the nanocapillaries are connected to a micropore on one side, and a larger solution macropore reservoir on the opposite side of the NCM. To study the role of asymmetry in the fluidic system external to the nanocapillaries in the rectification of ionic current, the macropore ID is altered while the micropore dimensions are held constant. A first control uses an asymmetric microfluidic device with no NCM. This device provides an Ohmic response and, as expected, current rectification is not observed as shown in Figure 3.2. In this device, without the ion permselective NCM, CP enriched and depleted zones are not present. The second control uses a symmetric device with the NCM centered between two identical micropores as shown in Figure 3.1. In this case, Figure 3.2 shows that the current is greatly reduced compared to the system without the ion permselective NCM, as the presence of NCM results in the formation of CP depleted zone. Although the device is not completely symmetric, it is effectively symmetric, because the regions that the CP depleted and enriched zones extend into are symmetric. Additionally, the CP depleted and enriched zones do not extend into the reservoirs at the end of the microchannels and consequently the effect of asymmetry in the microchannel-reservoir connections is negligible. Also, no rectification is observed in this symmetric device as the CP depleted zone is identical in the micropore regardless of the bias of the applied voltage. As observed in Figure 3.2, increasing the macropore diameter increases the current rectification factor. The device with the least degree of asymmetry has a  $150\ \mu\text{m}$  ID macropore and yields a rectifi-

cation factor of 2.8. Although the macropore and the via both have an ID of  $150 \mu m$ , this device is asymmetric because the length of the macropore ( $1 cm$ ) is much greater than the length of the via ( $60 \mu m$ ) that forms the entrance to the micropore. As the macropore ID is increased to  $300 \mu m$ , the rectification factor increases to 6.7, and as the macropore ID is increased to  $625 \mu m$  the rectification factor increases to 43. The device with the largest macropore ( $850 \mu m$  ID) produced the largest rectification factor of 75. Two mechanisms are likely to contribute to the ionic current rectification, from the asymmetry of the larger macropore system: First, in the ON state a decrease in the depleted CP zone length is postulated in the macropore due to its large cross-sectional area. Second, we attribute an increase in electroconvection to the increase in the macropore ID. In the present system, three important fluidic regions exist: the micropore, the nanocapillaries, and the macropore. The resistance of each fluidic region is related to its cross-sectional area when it is filled with a homogenous solution by the following equation:  $R = L/A\sigma$  where R is the resistance, L is the channel or reservoir length, A is the cross-sectional area, and  $\sigma$  is the conductivity. The different regions of the fluidic system are in series, making the total resistance the sum of the resistances of different fluidic regions. If any region has a very large resistance, its resistance dominates the resistance of the complete system. The application of the voltage to the system, causes formation of CP enriched and depleted zones, as ionic current passes through the permselective nanocapillaries. As the depleted and enriched CP zones form, the solution is no longer homogeneous and the conductivity of each region is also determined by the concentration profile of the region. The ON state or forward bias is observed when the CP enriched zone forms in the micropore as shown in Figure 3.3. In this state, the micropore, which has a high resistance due to its small cross-sectional area and long length, is filled with the CP enriched zone, increasing its conductivity. Conversely, when the polarity is reversed, the CP depleted zone extends into the micropore (as shown in Figure 3.3), resulting in reduced ionic conductivity in the micropore, and consequently the greatly reduced OFF state current is observed. In addition to the changes in the cross-sectional area that

effect conductivity, the changes in the macropore ID can also affect convective processes. For the NMI systems presented here, the bulk flow through the macropore is negligible as only a very small volume of solution flows through the NCM. Viscous coupling with the stationary macropore walls suppresses convection. However, inhomogeneities in the electric field across the NCM surface can produce electroconvection. It is also expected that large velocity gradients will exist with high flow through the nanocapillaries that are scattered about the NCM surface that has  $\approx 0.2$  porosity. Also, convection is expected to increase as the macropore ID increases, in a manner analogous to a fluid moving through a tube. For a moving solution, the propensity for convection is known to increase as the channel ID increases, as described by the Reynolds number:

$$Re = \frac{d_c \rho \langle v \rangle}{\eta} \quad (3.1)$$

where  $d_c$  is the channel diameter,  $\rho$  is the fluid density,  $\langle v \rangle$  is the flow velocity, and  $\eta$  is the viscosity. If convective forces increase, it is important to consider how convection will affect the observed current rectification. During the ON state, the depleted CP zone is in the macropore. In the presence of electroconvection, this depleted CP zone is likely to be disrupted, which results in a decrease in the system resistance, increasing the ON state current and ionic current rectification. However, during the OFF state, the current is limited by the depleted CP zone in the micropore, which is unaffected by convection in the macropore. Furthermore, disruption of the enriched CP zone in the macropore due to convection has little effect on the OFF state current, because it is not a current limiting region in the OFF state. To elucidate the role of electroconvection, we systematically vary the electric field for each macropore diameter. Figure 3.4 indicates that the symmetric device,  $150 - \mu m$  ID macropore device, and  $300 - \mu m$  ID macropore devices show little dependence of the rectification factor on the voltage. These devices have slopes of  $8 \times 10^{-4}$ ,  $5.6 \times 10^{-3}$ , and  $-7.1 \times 10^{-3}$ , respectively. The slopes are calculated using linear regression analysis for

the points from  $10-V$  to  $150-V$ , omitting the point at which zero volts is applied. However, for the  $625 - \mu m$  ID and  $850 - \mu m$  ID devices, the rectification factor increases slowly as the voltage is increased and the slope is greatest for the  $850 - \mu m$  ID devices. We postulate the increase in ionic rectification with increase in the applied voltage for these two devices is due to electroconvective effects; which dominate at higher electric fields. Furthermore, we also postulate an increase in the ionic density near the enriched micropore/nanocapillary interface results in higher inertial forces that increase convection. Typically, evidence for the presence or absence of electroconvection is contained in the noise of the I-T plots (view Figure 3.5). Noise produced by electroconvection is typically chaotic in nature and gives rise to lower frequency current oscillations. The energy/power spectrum of such chaotic signals usually depicts a  $1/f$  scaling. Similarly, fluctuations in fluid transfer through nanocapillaries are known to cause  $1/f$  noise.[Rubinstein et al.(2009)] Highly chaotic oscillations are present in the current signal in the ON state for  $625 \mu m$  and  $850 \mu m$  ID macropores, while little noise was observed for smaller ID macropores at an applied voltage of  $150V$ . Also, the magnitude of the noise in the OFF state is not as significant at any reservoir diameter, compared to its ON state counterpart. The dynamics of the fluctuating current are apparent in the I-T plots, and characteristic segments of the I-T plots are shown in Figure 3.7. In our system, the power spectral density analysis revealed no interesting scaling for the OFF state as shown in Figure 3.5. In the ON state, for frequencies between  $0.01$  to  $0.05 - Hz$ , we observed only Brownian type noise spectra as the power spectral density scales approximately as  $1/f^{2.2}$  as shown in Figure 3.5. It should be noted that the low data acquisition rate ( $1-Hz$ ) prevents analysis of the spectral density above  $1Hz$ , as it leads to signal attenuation. In spite of this constraint, in the frequency range between  $0.05Hz$  to  $0.5Hz$ , PSD analysis revealed  $1/f^{1.1}$  type scaling for  $850\mu m$  device (as shown in Figure 3.6),  $1/f^{1.16}$  for  $625m$ ,  $1/f^{0.945}$  for  $300m$ ,  $1/f^{1.87}$  for  $150\mu m$  and  $1/f^{1.79}$  for the symmetric device. The scaling factors near one for large macropore diameters in the ON state are strong indicators of chaotic oscillations and electroconvection in the device. Therefore, the spectral density analysis of the noise supports

the hypothesis that electroconvection is present in the devices with larger macropores, and contributes to the high ON state currents and high rectification factors.

### 3.4 Conclusions

The current rectification factor can be tailored by controlling the asymmetry ratio between the reservoir baths that are connected to opposite sides of a NCM. As the asymmetry ratio of the micropore and macropore increases, the current rectification factor of the device increases as well. Therefore, the asymmetry ratio can be used to fabricate devices with specific rectification factors. The current rectification is a result of the polarity dependent extension of the CP depleted zones into the fluidic regions with different cross-sectional areas and critical dimensions. Chaotic oscillations in the measured current of the  $625 - \mu m$  and  $850 - \mu m$  devices indicate that electroconvection can contribute to the current rectification as well. However, current rectification is also observed in the devices with smaller macropores, indicating that electroconvection is a secondary contribution for current rectification.

### 3.5 Figures

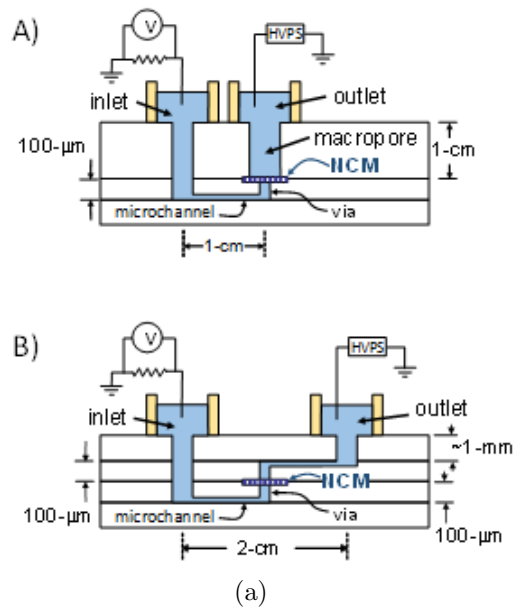
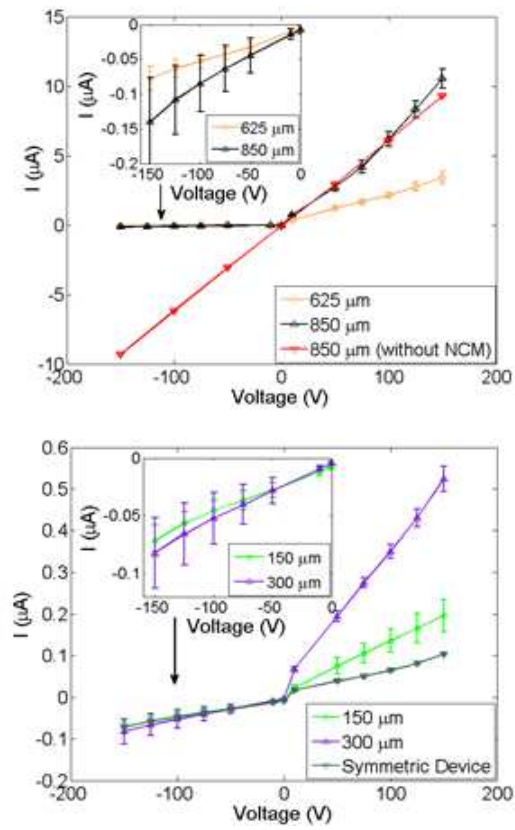
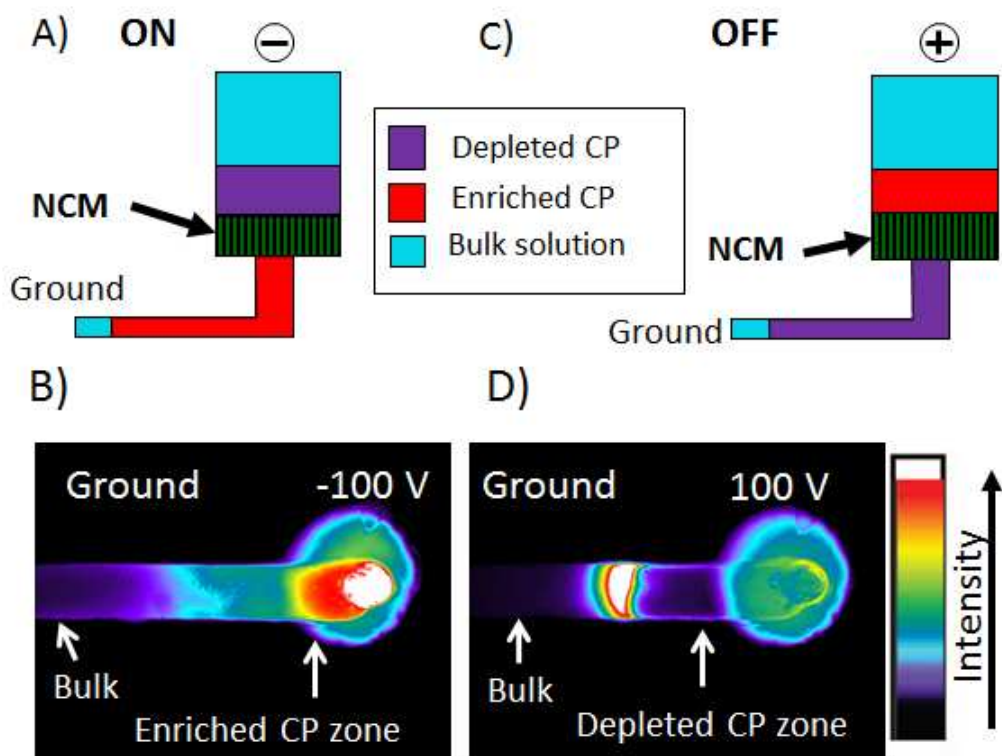


Figure 3.1: Schematics of the asymmetric device (A) and symmetric device (B) nanofluidic/microfluidic devices are shown. The NCM contains nanocapillaries with 10 nm IDs. Together the microchannel ( $40\mu m$  height) and the via ( $60\mu m$  height) are referred to as the micropore. For the asymmetric devices, the macropore IDs are 150, 300, 625, and  $850\mu m$ .



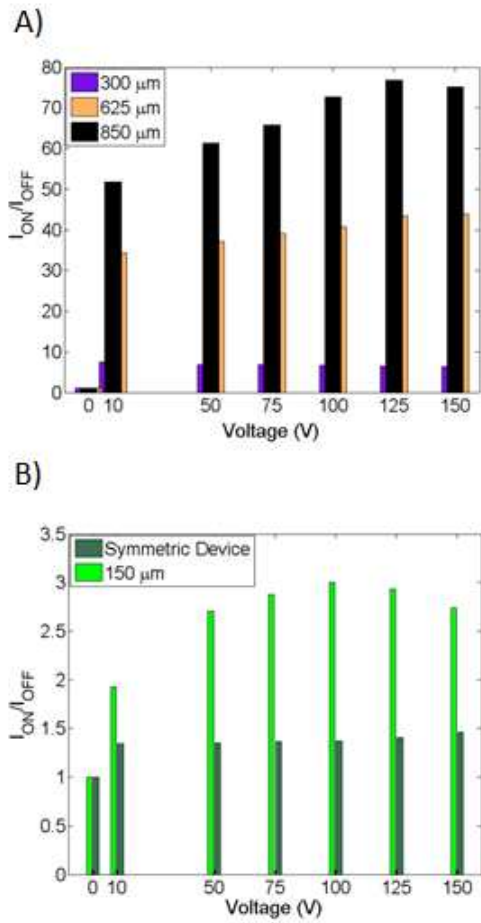
(a)

Figure 3.2: IV plots for the 625 and 850  $\mu\text{m}$  ID NMI devices and an 850- $\mu\text{m}$  ID device with no NCM are shown in Panel A. The IV plots for the symmetric, 150, and 300- $\mu\text{m}$  devices exhibit much lower currents as shown in Panel B.



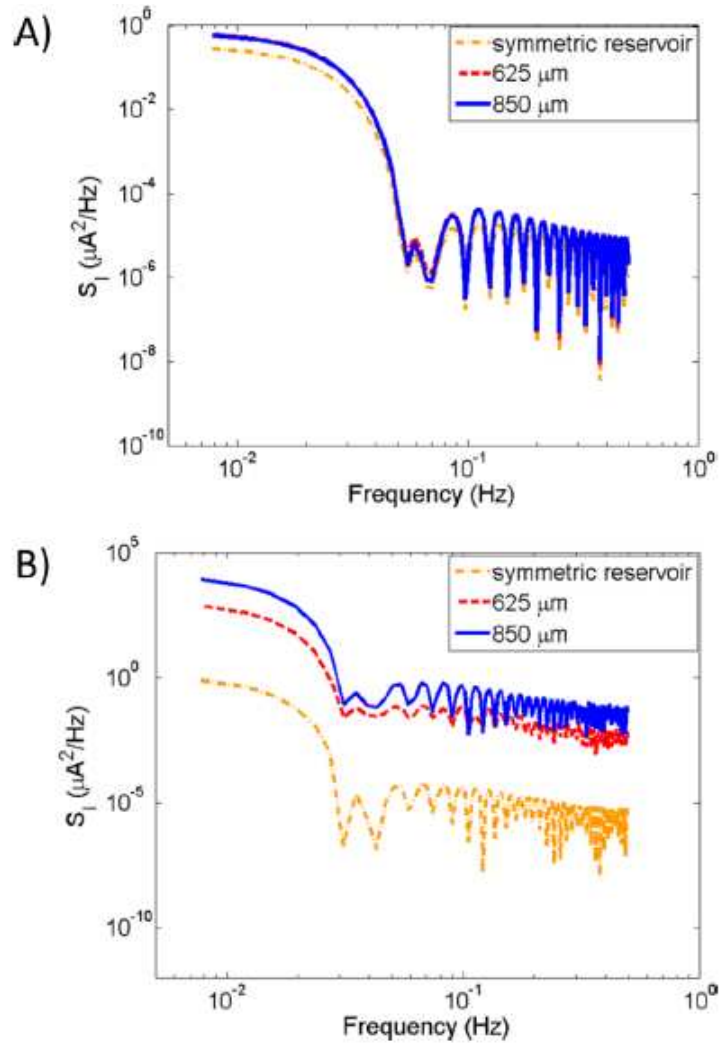
(a)

Figure 3.3: Schematics depicting a device (side view) show the location of the depleted and enriched CP zones during the ON (A) and OFF (C) states. The ON state is observed when the enriched CP zone forms in the micropore, and the OFF state is observed when the depleted CP zone forms in the micropore. An inverted fluorescent microscope is used to obtain images (bottom view) of enriched fluorescein in the micropore. In the On state (B), the enriched CP zone forms in the micropore. When the polarity is switched, the depleted CP zone forms in the micropore and the enriched CP zone forms in the macropore and the OFF state is observed. In (D), the depleted CP zone is extending into the micropore with a fluorescein band marking the end of the depleted CP zone. This fluorescein band forms from ions that have vacated the depleted CP zone, and it migrates away from the NCM. The enriched CP zone depicted in C) is not visible in the fluorescent image (D) because it is outside the field of view and above the PC-NCM. The intensity is encoded by a pseudocolor scale with black representing the lowest fluorescein concentration. The NCMs used in these studies have a negative surface charge and are cation permselective.



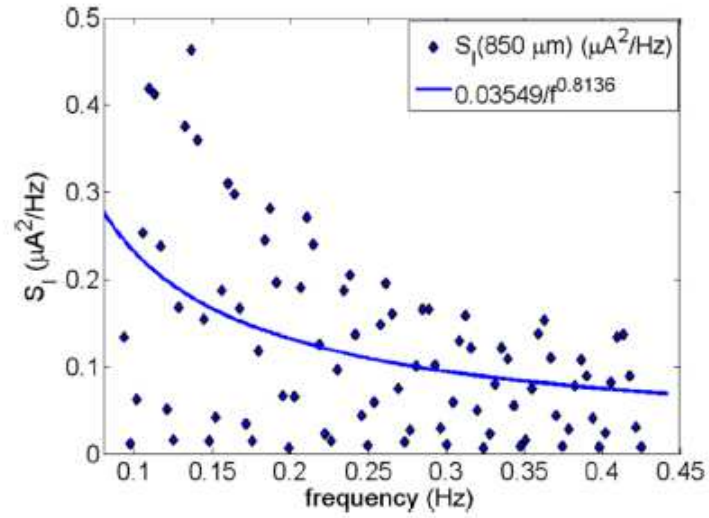
(a)

Figure 3.4: Current rectification factors are shown as a function of voltage for (A) 300, 625, and 850 $\mu\text{m}$  macropore devices (b)symmetric and 150 $\mu\text{m}$  macropore devices.



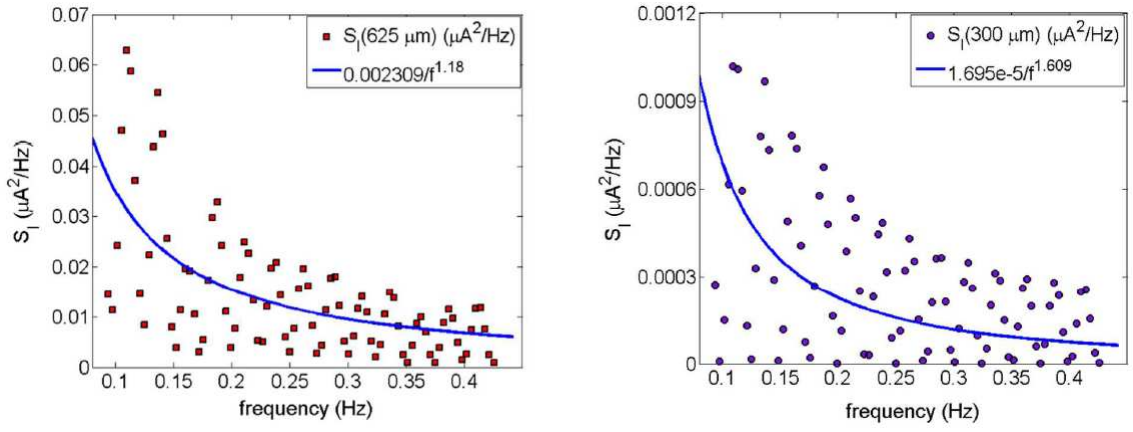
(a)

Figure 3.5: Noise in the current signal as a function of frequency is characterized using power spectra density (PSD) plots, for both (A) the OFF and (B) ON states at an applied voltage, 150 V.

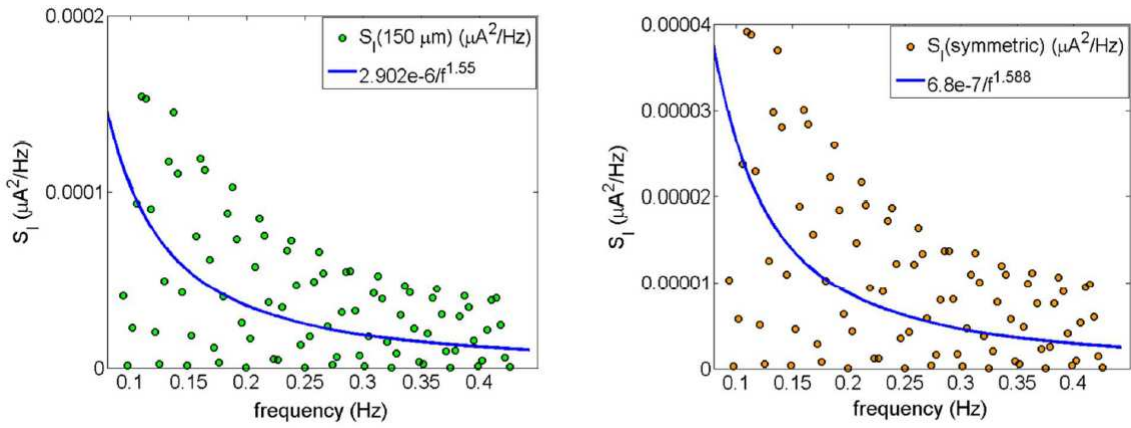


(a)

Figure 3.6: PSD fitting for the  $850\mu\text{m}$  device at 150 V ON state is shown with  $1/\text{frequency}$  scaling. Some white noise is present that does not scale as a function of frequency.



(a)



(b)

Figure 3.7: The power density spectra (PSD) analyses for the 625, 300, 150 μm, and symmetric devices are shown respectively in panels, (a) and (b).

## 3.6 References

1. [Pu and et al.(2004)] Q. Pu, et al., Nano Lett. 4 (2004) 10991103.
2. [Yuan and et al.(2007)] X. Yuan, et al., Int. J. Hydrogen Energy 32 (2007) 43654380.
3. [Howorka and et al.(2009)] S. Howorka, et al., Chem. Soc. Rev. 38 (2009) 23602384
4. [Chen and et al.(2010)] Z. Chen, et al., Nat. Mater. 9 (2010) 667675.
5. [Piruska and et al.(2010)] A. Piruska, et al., Chem. Soc. Rev. 39 (2010) 10601072.
6. [Kim and et al.(2007)]S. J. Kim, et al., Phys. Rev. Lett. 99 (2007) 044501.
7. [Yossifon and et al.(2008)] G. Yossifon, et al., Phys. Rev. Lett. 101 (2008) 254501.
8. [Chang and et al.(2008)] G. Yossifon, et al., Phys. Rev. E 79 (2009) 046305.
9. [Rubinstein and et al.(2009)] I. Rubinstein, et al., Phys. Rev. E. 80 (2009) 021505.
10. [Qiao and et al.(2005)] R. Qiao, et al., Colloid. Surface. A 267 (2005) 103109.

# Chapter 4

## Avalanche effects near nano-junctions

### 4.1 Abstract

In this article, we perform a numerical study of a nanopore connected across fluidic reservoirs of asymmetric geometries. The asymmetry between the reservoirs is achieved by changing the cross-sectional areas, and the reservoirs are designated as a micropore reservoir and a macropore reservoir. Under the action of an electric field directed from the macropore towards the micropore reservoir, we observe local nonequilibrium chaotic current oscillations. The current oscillations originate at the micro–nanopore interface owing to a novel dynamic clustering of ions. We term this phenomenon as “Avalanche effect”. We mathematically quantify chaos in terms of maximum Lyapunov exponent. The maximum Lyapunov exponent increases monotonically with an increase in the applied bias voltage and the macropore reservoir diameter. Finally, temporal power spectra maps of the chaotic currents depict a low frequency “ $1/f$ ” type dynamics for the voltage dominated chaos and “ $1/f^2$ ” type dynamics for the macropore reservoir dominated chaos. The physical insights into the current dynamics in asymmetric reservoir–nanopore systems provide avenues towards improved ionic diodes and fluidic pumps.

### 4.2 Introduction

Nanofluidic devices are currently being researched for myriad applications[Schoch et al.(2008) and Dekker(2007)], ranging from single molecule sensing[Howorka et al.(2009) and Saleh et al.(2003)], DNA sequencing [Chen et al.(2010) and Kasianowicz et al.(1996)] and water de-

salination[Kim et al.(2010)]. However, fabricating a single nanopore is often a challenging task and many pores are exposed to the fluidic reservoir filled with saline solution (see Fig. 4.1(a)). In this scenario, each pore is independently exposed to a small volume of reservoir of the order of a few hundreds of nanometers. The ionic solution is driven under the action of an electric field and ionic current measurements are recorded as an output. In the earlier chapter, ionic current can be rectified when a polycarbonate track etched nanoporous membrane is integrated with an asymmetric microfluidic reservoir geometry. These membranes were suggested as potential ionic diodes. The asymmetry between the reservoirs was achieved by changing their cross-sectional areas. The reservoir asymmetry along with the polarity dependent propagation of the enriched and depleted concentration polarization zones into these regions were identified as the fundamental mechanisms for current rectification. The primary advantage of these novel diodes from other ionic diodes[Siwy et al.(2002)] is avoiding to manipulate the geometry of the nanopore or the surface chemistry of the nanopore to rectify current. The latter two processes involve a lot of fabrication challenges owing to tuning the properties at the nanoscale level.

The diodes postulated using asymmetric cross-sectional microporous environment (discussed in the earlier chapter) also manifested in current oscillations in the output current upon systematic increase in the degree of asymmetry between the fluidic reservoirs and at larger bias voltages. The current oscillations were predominantly observed when the applied electric field is directed from the macropore towards the micropore reservoir. The exact physical mechanism behind the current oscillations in their experiments is still unclear. However, there are several mechanisms postulated for the nonequilibrium current fluctuations/oscillations in nanoporous membranes. In a recent publication by Powell et al., the current fluctuations were attributed to the intrinsic property of the nanoporous membrane, namely dynamical changes in the ionic diffusivity and its corresponding ionic mobility. Other mechanisms include nanopore wall surface charge fluctuations, conformational changes of the pore structural constituents, nanobubble formation inside the nanopore and water splitting.

Further, strong concentration polarization effects resulting in depletion of ions near the interfaces of micro–nanopore integrated systems have resulted in instability of ionic charges and correspondingly to its electro–osmotic flow near these interfaces. These instabilities were argued as the source of chaotic current oscillations[Kim et al.(2010)].

In this article, we perform numerical simulations of a single nanoporous membrane connected to asymmetric reservoirs of a few hundreds of nanometers. We distinguish the two asymmetric reservoir geometries as a micropore reservoir and a macropore reservoir. We report novel chaotic current oscillations, owing to the coupling between the electric field and the enriched concentration zone observed at the entrance of the drain micro–nanopore junction. The dynamical clustering of ions near the enriched micro-nanopore junction leads to temporal changes in the electric potential, which in turn results in unstable/chaotic currents. We demonstrate that the strong clustering of ions is due to the introduction of an asymmetry in the fluidic reservoir. We validate our hypothesis by calculating the growth rate quantified by the maximum Lyapunov exponent ( $\lambda^*$ ) from the simulated ionic current signals. We observe a positive Lyapunov exponent under all the applied voltages and under different macropore reservoir diameters. A positive  $\lambda^*$  indicates unstable ionic currents. Furthermore, we compute the temporal power spectra map of the simulated chaotic currents inside the nanopore for different voltages and macropore reservoir diameters. We draw conclusions on the dominant source of chaos from our PSD analysis. The diameter of the micropore reservoir geometry is fixed in the entire study.

## 4.3 Theory

### 4.3.1 Area–averaged multi–ion transport model (AAM)

To understand the ion transport dynamics in a micro–nano–macropore system, we numerically investigate the axial changes in the potential ( $\phi$ ) and individual ionic concentration ( $c_i$ ) after averaging the properties in the radial direction. A detailed derivation of the model

is discussed in one of the earlier chapters and in this section we present a concise summary of the model. We consider the 2-D Poisson–Nernst–Planck equations and assume ideal nonpolarizable electrodes and hence, neglect the Faradaic reactions that occur near the electrode. Further, we consider  $1mM$  of sodium monobasic and sodium dibasic ionic solution, and assume that the ions inside the Steric layer are rigidly held and do not contribute to the ionic current. We also assume an isotropic medium with a constant dielectric permittivity  $\epsilon = \epsilon_0\epsilon_r$ .  $\epsilon_0$  is the permittivity of free space and  $\epsilon_r$  is the relative permittivity of the medium. Under these assumptions, the mass transfer of each buffer species is given by,

$$\frac{\partial c_i}{\partial t} = -\nabla \cdot \mathbf{\Gamma}_i \quad (4.1)$$

where  $\mathbf{\Gamma}_i$  is the total flux of each species  $i$  in the solution,

$$\mathbf{\Gamma}_i = -D_i\nabla c_i - \Omega_i z_i F c_i \nabla \phi \quad (4.2)$$

where  $D_i$ ,  $c_i$  and  $z_i$  denote the diffusion coefficient, molar concentration, and valence of each ion, respectively.  $\Omega_i$  is the ionic mobility which is related to the diffusion coefficient of the ionic species by Einstein's relation,  $\Omega_i = \frac{D_i}{RT}$ .  $F$ ,  $R$ , and  $T$  represent Faraday's constant, ideal gas constant and absolute thermodynamic temperature, respectively. We assume,  $c_i$  and  $\phi$  are uniform in the  $\theta$ -direction. Integrating Eq. 4.1 over the  $(r, \theta)$  direction and dividing with the cross-sectional area  $A(x)$ , the transport of each ion,  $i$  in the axial direction can be calculated as,

$$\begin{aligned} \frac{1}{A(x)} \int_0^R \int_0^{2\pi} \left( \frac{\partial c_i}{\partial t} \right) r dr d\theta &= \int_0^R \int_0^{2\pi} \left[ \frac{\partial}{\partial x} \left( \frac{1}{A(x)} D_i \frac{\partial c_i}{\partial x} + \frac{1}{A(x)} \frac{D_i z_i F}{RT} c_i \frac{\partial \phi}{\partial x} \right) \right] r dr d\theta \\ &+ \frac{1}{A(x)} \int_0^R \int_0^{2\pi} \left[ \frac{1}{r} \frac{\partial}{\partial r} \left( D_i r \frac{\partial c_i}{\partial r} + \frac{D_i z_i F}{RT} r c_i \frac{\partial \phi}{\partial r} \right) \right] r dr d\theta \end{aligned} \quad (4.3)$$

$R$  is the radius of the pore, varying along the axial direction to represent the micropore, nanopore and macropore, respectively. Hence, the cross-sectional area,  $A(x)$  also varies along the axial direction. Since, there is no leakage of ionic current at the pore walls, the normal flux of each ion on the pore walls is assumed to be zero,

$$\mathbf{n}_w \cdot \mathbf{\Gamma}_i|_{r=R} = -D_i \frac{\partial c_i}{\partial r} \Big|_{r=R} - \left( \frac{z_i D_i F}{RT} c_i \frac{\partial \phi}{\partial r} \right) \Big|_{r=R} = 0 \quad (4.4)$$

where  $\mathbf{n}_w$  denotes the unit normal vector (pointing outwards) to the pore surface. Substituting the above condition in Eq. 4.3, we obtain the Area-Averaged transport equation for the ionic species,

$$A(x) \frac{\partial \hat{c}_i}{\partial t} = \frac{\partial}{\partial x} \left( A(x) D_i \frac{\partial \hat{c}_i}{\partial x} \right) + \frac{\partial}{\partial x} \left( \frac{z_i D_i F}{RT} A(x) \hat{c}_i \frac{\partial \hat{\phi}}{\partial x} \right) \quad (4.5)$$

$\hat{f} = \frac{1}{A} \int_0^r \int_0^{2\pi} (f(r, \theta)) r \, d\theta dr$  denotes the area-averaged quantity. The first term on the right hand side, denotes the ionic diffusive effects, while the second term denotes the electromigration effects inside the system.

We now consider the 2-D Poisson equation for the electric field distribution,

$$\nabla \cdot (\epsilon_r \nabla \phi) = -\frac{\rho_e}{\epsilon_0} \quad (4.6)$$

$\rho_e$  is the net space charge density of the ions defined as,  $\rho_e = F (\sum_{i=1}^n z_i c_i)$ , where  $n$  is the number of ionic species in the solution. Applying the charge conservation at the walls leads to the following electrostatic boundary condition,

$$\mathbf{n} \cdot \nabla \phi = \frac{\sigma}{\epsilon} \quad (4.7)$$

where  $\mathbf{n}$  denotes the unit normal vector (pointing outwards) to the wall surface and  $\sigma$  is the surface charge density of the walls. As before, we assume  $\phi$  is uniform in the  $\theta$ -direction.

Integrating Eq. 4.6 over the  $(r, \theta)$  and substituting the preceding boundary condition, we obtain radially averaged electrostatic potential in the axial direction,

$$\frac{\partial}{\partial x} \left( A(x) \frac{\partial \hat{\phi}}{\partial x} \right) = -\frac{A(x)}{\epsilon} \left( \hat{\rho}_e + \frac{4\sigma_s(x)}{d(x)} \right) \quad (4.8)$$

$\sigma_s(x)$  and  $d(x)$  are the fixed surface charge density and the diameter of the pore. Both these quantities vary axially to incorporate the surface and geometrical properties of the micropore, nanopore and macropore reservoirs. The fixed wall surface charge density distribution,  $\sigma_s(x)$ , is given by:

$$\sigma_s(x) = \begin{cases} \sigma_{mi}, & 0 \leq x \leq L_{mi} \\ \sigma_n, & L_{mi} < x \leq L_{mi} + L_n \\ \sigma_{ma}, & L_{mi} + L_n < x \leq L_{mi} + L_n + L_{ma} \end{cases} \quad (4.9)$$

where  $\sigma_{mi}$ ,  $\sigma_n$  and  $\sigma_{ma}$  denote the homogeneous charge distribution on the walls of the micropore, nanopore and macropore, respectively.  $L_{mi}$ ,  $L_n$  and  $L_{ma}$  refer to the length of the micropore, nanopore and macropore, respectively. The total ionic current,  $I(x)$  through the pore is calculated by summing the individual fluxes over the cross-sectional area, i.e.,

$$I(x) = FA(x) \sum_i^n z_i \Gamma_i \quad (4.10)$$

where  $\Gamma_i = -D_i \frac{\partial \hat{c}_i}{\partial x} - \frac{z_i F D_i}{RT} \hat{c}_i \frac{\partial \hat{\phi}}{\partial x}$  is the total area-averaged flux of each ionic species, contributed by a diffusive component resulting from the concentration gradient, and an electric migration component due to the electric field interaction with the ionic concentration. We discuss the necessary boundary conditions for the closure of the problem. We consider the macropore on the top (see Figure 4.1(a)) as the source and is given a constant electric potential ( $\phi_{DC}$ ) at the end of the macropore reservoir. The micropore on the bottom is considered as the drain and is grounded. The concentration of both the ions at the ends of the micro/macropore is assumed to be equal to the bulk ionic concentration,  $c_0$ .

The solvers for the AAM model are developed and implemented using the finite volume method in OpenFOAM (Open Field Operation and Manipulation) version 1.6. The electro-migration terms in the modified PNP equations are discretized using second–order bounded NVD schemes [Toro(1999)] to avoid artificial oscillations and to ensure that the solution is bounded. All the Laplacian terms are discretized using second–order central differencing scheme. Second–order implicit time differencing scheme[<http://www.openfoam.com/>(2011)] is used to discretize the variables in time. A finer mesh is introduced at the entrance and exit of the nanopore to resolve the features of the thin electrical double layer near these interfaces.

## 4.4 Simulation details

We consider a cylindrical nanopore of length  $L_n = 6\mu m$ , and diameter  $d_n = 10nm$ . The nanopore is connected to a micropore of length  $L_{mi} = 6\mu m$ , diameter  $d_{mi} = 50nm$ , and a macropore of length,  $L_{ma} = 2\mu m$ . The macropore diameter ( $d_{ma}$ ) is systematically varied from  $50nm$  to  $1\mu m$ . In the former case, the ratio of macro to micropore reservoir diameter ( $R = d_{ma}/d_{mi}$ ) is 1 while in the latter case, we ensure a 20 fold difference between the two reservoir diameters. We would like to note that though the reservoir diameters are in the range of nanometers, we designate them as micro and macropore to distinguish the reservoir geometry. The voltage is systematically varied from  $5V$  to  $100V$  and is always driven from the macropore towards the micropore. Phosphate buffer of constant concentration ( $0.39mM$  of  $NaH_2PO_4$  and  $0.61mM$  of  $Na_2HPO_4$ ) is used in all the simulations. The simulated temperature is  $T = 300K$ . The diffusivities of  $Na^+$ ,  $H_2PO_4^-$  and  $HPO_4^{2-}$  are  $1.33 \times 10^{-9}m^2/s$ ,  $0.879 \times 10^{-9}m^2/s$ , and  $0.439 \times 10^{-9}m^2/s$ , respectively. We assume the dielectric constant of the aqueous solution to be,  $\epsilon_r = 80$ . The nanopore is modeled with a negative surface charge density,  $\sigma_n = -3mC/m^2$ , which is a typical surface charge density of a poly carbonate track etched (PCTE) membrane, when an electrolyte concentration of  $1mM$  is used. We assume,

the surface charge density on the walls of the micropore and macropore reservoirs are zero, ( $\sigma_{mi} = \sigma_{ma} = 0$ ), as they are far away from the nanopore to have an influence on the ion transport.

## 4.5 Results and Discussion

### 4.5.1 Current-time dynamics

A schematic illustration of the micro–nano–macropore simulation set–up is shown in Figure 4.1(b). Further, we calculate the conductive currents at 4 different locations, namely in the bulk micropore reservoir,  $B_{micro}$  at  $x = 1\mu m$ , at the micro/nanopore junction,  $NJ$ ,  $x = 6.5\mu m$  (which is  $0.5\mu m$  from the entrance of the micro/nanopore), center of the nanopore,  $NP$ ,  $x = 9\mu m$ , and at the bulk macropore reservoir,  $B_{macro}$ ,  $x = 13.5\mu m$  (see Fig. 4.1(b)). Fig. 4.2(a) shows that the micro–nano–macropore system exhibits a non–Ohmic current–voltage characteristic. The magnitude of the output current,  $|\langle I \rangle|$  is calculated at the center of the nanopore, (NP region) and is averaged over  $4ms$  time interval after the current reaches a steady-state. Here the ratio of macropore diameter to micropore diameter is 4. Recent experimental studies by Kim et al.[Kim et al.(2007)] and Yossifon et al.[Yossifon et al.(2008) and Chang et al.(2009)] have also observed similar non–Ohmic current–voltage characteristics in a micro–nanopore integrated system. In our earlier work, we highlighted the mechanism behind these non–Ohmic current characteristics to the concentration polarization effects developed near the micro–nanojunctions. The current–voltage characteristics reveal the average transport properties of the pore. In order to understand the dynamic characteristics of the current, we analyze the current-time signals. We would like to highlight that the slowest process in the system is the diffusive process, whose characteristic time is  $(L_{nano}^2/2D_{ion})$ , where  $L_{nano} = 6\mu m$  is the length of the nanopore and  $D_{ion}$  corresponds to  $D_{(HPO_4^{2-})}$  as it has the smallest diffusion coefficient,  $D_{(HPO_4^{2-})} = 0.439 \times 10^{-9}m^2/s$ . Thus, it takes approximately  $41ms$  for the system to relax

and reach a steady-state. To characterize the long time dynamics of the system, we run the simulations for each voltage case, at least till  $48ms$ , with a sampling frequency of  $100MHz$  to ensure that the current oscillates about a steady mean.

Fig. 4.2(b) shows current–time dynamics from  $46ms–48ms$  for an applied voltage of  $5V$ , corresponding to the quasi–equilibrium regime, and also for  $100V$ , corresponding to a highly non–equilibrium regime. The current trace was analyzed at the region NP. We observe weak oscillations in the current trace for the low bias voltage, while there is a high degree of oscillations in the current signal for the  $100V$  case. To quantify the differences between these signals, Fig. 4.2(c) shows the current histogram. We notice a peak in the histogram at  $15.36pA$ , with a spread of  $0.2pA$  for the quasi–equilibrium voltage of  $5V$ , while  $100V$  case results in  $3–4pA$  increase in the width of the current histogram (see Fig. 4.2(c)). To mathematically quantify the non–equilibrium current oscillations, we calculate the growth rate given by the maximum Lyapunov exponent ( $\lambda^*$ ) for each voltage. The mathematical details of the implementation of  $\lambda^*$  is discussed in the appendix.  $\lambda^*$  is normalized as we consider the time scale in the units of time index of measurements and not the real time units. We use TISEAN software package to calculate  $\lambda^*$ . Fig. 4.2(d) reveals a positive Lyapunov exponent for all voltages considered. A positive Lyapunov exponent indicates a positive growth rate revealing the unstable current dynamics inside the nanopore system.  $\lambda^*$  is  $0.003 \pm 0.001$  for  $5V$  and it monotonically increases with voltage, reaching a value of  $0.055 \pm 0.006$  at  $100V$ . We postulate the monotonic increase in  $\lambda^*$  to the monotonic increase in the standard deviation of the current signal ( $I_{SD}$ ) with voltage (see inset of Fig. 4.2(a)). The exact correlation between  $I_{SD}$  and  $\lambda^*$  is still unclear and is subject of subsequent study.

To ensure that  $\lambda^*$  calculations are accurate for low bias voltage, and the current dynamics are indeed unstable and not a numerical oscillation, we considered a simple Gaussian random noise signal and calculated the maximum Lyapunov exponent using TISEAN software on this signal.  $\lambda^*$  was found to oscillate randomly and didn't yield a growth rate, unlike a chaotic signal.

Next, we understand the effect of  $R(= d_{ma}/d_{mi})$  on the output current. To vary  $R$ , we increase the macropore reservoir diameter keeping the micropore reservoir diameter and nanopore diameter fixed in our numerical simulations. Fig. 4.3(b) shows that the magnitude of the average output current varies non-monotonically with  $R$  and reaches a maximum at  $R = 4$ . The output current,  $|\langle I \rangle|$  is calculated at the center of the nanopore, (NP region) and is averaged over  $4ms$  time interval after the current reaches a steady-state. This result is indeed interesting as one would expect a monotonic increase in current  $I$  with area. However, our simulations revealed that the concentration of ions inside the nanopore vary non-monotonically with  $R$  affecting the current characteristics. A maximum concentration of  $Na^+$  ions inside the nanopore was observed for  $R = 4$  at a fixed low bias voltage of  $5V$ , where the current was found to be maximum. Fig. 4.3(b) shows the current–time dynamics, for  $R = 2$  and  $R = 20$ . For  $R = 20$ , we observe high degree of current oscillations of the order of  $0.8pA$ , while weak oscillations of the order of  $0.025pA$  was observed for  $R = 2$  (see Fig. 4.3(c)). The high degree of current oscillations for large  $R$  is quite surprising as a low bias voltage of  $5V$  is applied in this case. In order to ensure that these results are physical, we calculated the maximum Lyapunov exponent. Fig. 4.3(d) reveals a positive Lyapunov exponent for all  $R$ .  $\lambda^*$  is  $0.0024$  for  $R = 2$  and it monotonically increases with  $R$ , reaching  $0.02 \pm 0.004$  at  $R = 20$ . We again postulate the monotonic increase in the maximum Lyapunov exponent to the monotonic increase in the standard deviation of the current  $I_{SD}$  with  $R$  (see inset of Fig. 4.3(a)). The analysis helps us to conclude that asymmetric nature of the fluidic reservoir plays a vital role compared to the voltage applied in observing large current oscillations in the nanopore systems.

Before highlighting the mechanism behind the current oscillations observed in our study, we briefly discuss different sources of current oscillations postulated in the literature. The source of chaos was inferred from the dynamical changes in the ion diffusion coefficient and its corresponding ionic mobility. The other major source was identified as the dynamical change in the surface charge density on the pore walls due to constant protonation and deprotonation

reactions. In this study, we used a constant surface charge density in our numerical model. Further, a time-independent diffusion coefficient was used for all the ions. Hence, we rule out the above postulations for the source of current oscillations observed in our study.

### 4.5.2 Dynamic clustering of ions

In order to reveal the mechanism, we investigate the ionic concentration distribution along the entire micro-nano-macropore system. For a symmetric reservoir, ( $R = 1$ ), under the action of an applied voltage from the source reservoir to the drain reservoir (see Fig. 4.4(a)), the co-ions (anions in this case) are repelled from the source-nanopore interface and are attracted towards the anode. In order to maintain neutrality, the cations are also repelled at this interface. Hence an ion depletion zone is created at the source-nanopore interface. Further, the co-ions are repelled from both the cathode and from the nanopore (as the pore is negatively charged) and they get accumulated near the drain-nanopore interface. In order to maintain electroneutrality, the cations (counter-ions) also get accumulated at this interface. Thus the ions are polarized near both the interfaces. For a symmetric reservoir case, the accumulation/enrichment of ions is relatively weak. However, when the sizes of the reservoirs are asymmetric, we observe a high clustering of ions in the ion enrichment zone. We call this region as ‘‘Avalanche zone’’ (see Fig. 4.4(b)).

Fig. 4.4(c) shows the sodium ion concentration distribution along the symmetric reservoir system. In the case of symmetric reservoir at  $1mM$  bulk concentration, for a low bias voltage of  $5V$  and for  $R = 1$ , we observe around 15 fold enrichment near the drain micro-nanopore interface. Furthermore, the long time dynamics reveal weak oscillations of ionic concentration distribution under the low bias voltage, near the enriched drain micro-nanopore interface. However, for an asymmetric reservoir, when we introduce a 20 fold difference in the reservoir diameter ( $R = 20$ ), we observe 30 times enrichment of ionic concentration near the drain micro-nanopore interface resulting in large concentration gradients and clustering of ions as shown in Fig. 4.4(d). The interaction of electric field with the high concentra-

tion gradients disrupts the ion flow inside the nanopore resulting in dynamical changes in the ion concentration inside the pore as shown in Fig. 4.4(d). Furthermore, we observe inhomogeneous distribution of sodium ions near the micro–nanopore interface (see inset of Fig. 4.4(d)). Fig. 4.4(e) shows the sodium ion concentration distribution for a low bias voltage of  $5V$  and for  $R = 4$ . In this scenario, we observe 43 times enrichment of ionic concentration near the drain-nanopore interface compared to the bulk reservoir. Also, the enrichment of ions is 1.4 times higher than  $R = 20$ . This suggests that concentration distribution inside the nanopore varies non-monotonically with  $R$  resulting in non-monotonic current dependence with  $R$  as discussed before. Further, the depletion of ions for  $R = 20$  is relatively weaker than for  $R = 4$  under the same bias voltage conditions. Also, the degree of oscillations of ions near the enriched interface is weaker for  $R = 4$  (see inset of Fig. 4.4(e)) compared to  $R = 20$  case, resulting in higher current oscillations for the latter. Furthermore, our simulations reveal that the oscillations in the enriched zone becomes stronger on the application of high bias voltage of  $100V$  for  $R = 4$  (see inset of Fig. 4.4(f)). This is because, the high electric field strongly interacts with the enriched concentration gradients disrupting the ion dynamics near this interface. We observe 80 fold enrichment of ions near the drain-nanopore interface for an applied voltage of  $100V$ .

We would like to highlight that chaotic current oscillations in ion-selective membranes have been observed before by Mani et al along with other researchers[Kim et al.(2007), Yossifon et al.(2009), Rubinstein et al.(2009)]. The fundamental mechanism behind the chaotic current oscillations discussed in most of the earlier works is convective instability, which are of two types. Firstly, convective instability due to hydrodynamic flow[Kim et al.(2007)]. In this scenario, we observe depletion of ions near one of the interfaces of an ion-selective membrane, resulting in a finite net space charge density region at this interface. Further, the electric field is non-uniform near this interface. The non-uniform electric field interacts with the net space charge density, resulting in a nonequilibrium electroosmotic flow. Under the action of a large applied bias, the electroosmotic flow becomes unstable resulting

in a chaotic flow dynamics[Kim et al.(2007)]. In our numerical simulation, we do not include the hydrodynamic term as we had identified from our earlier work that the contribution of electroosmotic flow is small in the calculation of the total electric current in micro–nanopore integrated systems. Hence, convective instability due to hydrodynamic flow is absent in our model.

The second convective instability that is highlighted in an ion-selective system is electroconvective instability[Yossifon et al.(2009), Rubinstein et al.(2009)]. Such an instability also occurs due to the depletion of ions developed at one of the interfaces of an ion-selective membrane. The depletion region results in high concentration gradients. Further, under a large bias, the electroneutrality in the depletion region breaks resulting in a net space charge density region. On further increase in the applied voltage, the space charge density in the depletion region becomes unstable, resulting in chaotic oscillations of electric current.

In this work, ion depletion occurs at the nano-macropore reservoir. However, the depletion region is very weak at this interface owing to the large macropore reservoir diameter. Hence, we observe a very small net space charge density at this interface even under the action of a large applied bias. Furthermore, we do not observe any instability in the net space charge density at this interface. However, there is an instability of charges near the drain micro-nanojunction where the ions are enriched. This charge instability owing to the clustering of ions, propagates into the nanopore and disrupts the charge distribution inside the nanopore. Thus, our simulation results illustrate that electroconvective instability due to depletion of ions is not the origin of chaos in asymmetric micro-nano-macropore systems, while dynamic clustering of ions at the drain micro-nano junction is the origin. We believe this is indeed a novel phenomenon in the field of ion-selective membranes, as often-times the enriched region is considered inconsequential in predicting the dynamics of ionic current. Furthermore, Wang and his colleagues also experimentally observed current oscillations in nanoporous membranes integrated to asymmetric fluidic reservoirs. The origin of the current oscillations was postulated to be electroconvective instability in the depleted

macropore. However, concrete evidence of this mechanism was not postulated due to the lack of experimental data. We believe the present article reveals the actual mechanism in current oscillations in such asymmetric reservoir systems. We further highlight that the instabilities in current are local in nature, i.e., the oscillations are strong in the vicinity of the enriched micro–nanopore interface (see Fig. 4.5(b)) and to an extent inside the nanopore (see Fig. 4.5(c)). Away from the micro–nano interface, near the bulk micropore region, the oscillations die out (see Fig. 4.5(a)). Also, in the bulk macropore region, the current has steady-state characteristics (see Fig. 4.5(d)), owing to the absence of clustering of ions at these regions. The electric potential at each time instant can be related to the concentration by Eq. 4.8. We observe an unstable point in the electric potential distribution near the drain micro–nanopore interface as shown in Fig. 4.6(a). Fig. 4.6(b) shows the oscillating behavior of the unstable potential near the drain micro–nanopore interface (at  $x = 6200nm$ ). A combination of dynamic clustering of ions near the drain micro–nanopore interface and the presence of unstable potential regions at this interface results in unstable current oscillations.

### 4.5.3 Power spectral density (PSD)

We further analyze our simulated current traces by calculating its power spectral density ( $S_I$ ) in the frequency range between 0 to  $50MHz$ . The power spectral density is computed using the Welch method. We considered  $6ms$  current trace (ensuring that the current oscillates about a steady mean) to calculate the spectra. The current signal is divided into longest possible sections to obtain close to but not to exceed 8 segments, with 50% overlap. Each section is windowed with a Hamming window. The signal is sampled with a sampling frequency ( $f_s$ ) of  $100MHz$ . The modified periodograms are averaged to obtain the spectral estimate for a frequency range  $[0 - f_s/2]$ . Fig. 4.7(a) shows power spectra of chaotic current trace for  $100V$  and for  $R = 4$ . The power spectra reveals a power–law dependence,  $1/f^\alpha$  scaling in the low frequency range between  $100kHz$  to  $10MHz$ . The exponent  $\alpha$  is found to be close to 1 for the  $100V$  current signal. The inset of the figure reveals  $S_I$  for a lower voltage

of  $70V$  and for  $R = 4$ . The power spectra is similar to the  $100V$  results and the spectra scales close to  $1/f$  in the same frequency range. However, Fig. 4.7(b) shows the power spectra of the simulated current–time signal for a macropore diameter of  $1\mu m$  ( $R = 20$ ). The power spectra for this chaotic current signal scales as  $1/f^\alpha$  with  $\alpha$  close to 2, in the low frequency range between  $10kHz$  to  $1MHz$ . The inset of the figure reveals the spectral estimate for macropore diameter of  $0.5\mu m$  ( $R = 10$ ). The power spectra is similar to the  $1\mu m$  case. A low bias voltage of  $\phi_{DC} = 5V$  is applied for the aforementioned simulations which could result in the deviation from  $1/f$  type dynamics as we observed systematic  $1/f^2$  type dynamics for other macropore reservoir diameters under low bias voltage of  $5V$ . Thus, we believe the power spectral density analysis helps us to understand if the system is voltage dominant chaos or macropore reservoir dominant chaos. The mathematical analysis of the calculation of maximum Lyapunov exponent is highlighted in section 4.6.

## 4.6 Calculation of maximum Lyapunov exponent

Given the scalar time series data of the current measurements,  $I_n$ , we convert the scalar measurements into state vectors by the method of delays. A delay reconstruction in  $m$  dimensions is formed by the vectors  $\mathbf{I}_n$ , given as

$$\mathbf{I}_n = (I_{n-(m-1)\tau}, I_{n-(m-2)\tau}, \dots, I_{n-\tau}, I_n). \quad (4.11)$$

The time difference in number of samples,  $\tau$  between adjacent components of the delay vector is referred to as the lag or the delay time. We create a vector for every scalar observation,  $I_n$ , with  $n > (m - 1)\tau$ . Taken's embedding theorem states that an optimal choice of  $m$  and  $\tau$ , would ensure that the geometrical object formed by the vector  $\mathbf{I}_n$ , is equivalent to the original current trajectory,  $I_n$ . Further, the above argument is guaranteed if  $m$  is larger than twice the box counting dimension,  $D_F$  number of active degrees of freedom, regardless of

how high the dimensionality of the true state space is. However, when we start to analyze the time series data, we neither know the box counting dimension, and hence,  $m$ , nor do we have any idea about the time lag  $\tau$ .

### 4.6.1 Mutual Information analysis

In order to determine the optimal time lag  $\tau$ , we use the time delayed mutual information analysis suggested by Fraser and Swinney. The mutual information takes into account the nonlinear correlations unlike the autocorrelation function. In this case we compute

$$S = - \sum_{ij} p_{ij}(\tau) \ln \frac{p_{ij}(\tau)}{p_i p_j} \quad (4.12)$$

where for some partition on the real numbers,  $p_i$  is the probability to find a time series in the  $i^{th}$  interval,  $p_{ij}$  is the joint probability that the observation falls into the  $i^{th}$  interval and the observation time  $\tau$  later falls into the  $j^{th}$ . Now, the first minima of the time delayed mutual information gives the optimal time delay  $\tau$ . There is no mathematical proof associated with this statement. We use TISEAN software package to calculate the time lag  $\tau$ . We found  $\tau$  to be 1 using the current trace for an applied voltage of 100V and  $R = 4$ . A 10ns data sampling was considered and 5ms – 48ms current signal was analyzed.

### 4.6.2 Embedding dimension

We now try to optimize the embedding dimension ( $m$ ). To calculate the embedding dimension, we need to first find the correlation dimension,  $D$ . The notion of constructing a geometrical object from a finite sample of data points is called correlation dimension. To calculate correlation dimension, we compute the correlation sum

$$C(\epsilon) = \frac{1}{N_{pairs}} \sum_{j=m}^N \sum_{k < j-w} \Theta(\epsilon - |I_j - I_k|) \quad (4.13)$$

where  $\mathbf{I}_i$  are  $m$  dimensional delay vectors.  $N_{pairs} = (N - m + 1)(N - m - w + 1)/2$  is the number of pairs of points covered by the sum.  $\Theta$  is the Heaviside step function.  $\epsilon$  is the order of resolution of the measurements. In the limit of an infinite amount of data ( $N \rightarrow \infty$ ), and for small  $\epsilon$ , we can expect  $C$  to scale like a power law,  $C(\epsilon) \propto \epsilon^D$  and we can define the correlation dimension  $D$  by,

$$d(N, \epsilon) = \frac{\partial \ln(C(\epsilon, N))}{\partial \ln \epsilon} \quad (4.14)$$

$$D(\epsilon, m) = \lim_{\epsilon \rightarrow 0} \lim_{N \rightarrow \infty} d(N, \epsilon) \quad (4.15)$$

To determine,  $D$ , we check for the convergence of  $D$  for different values of  $m$ . We need to be careful in excluding the temporally correlated points from the pair counting by using a Theiler window,  $w$ . In order to calculate the correlation integral accurately, the correlation sum should cover random sample of points drawn independently. However, successive elements of a time series are not usually independent, but sometimes highly correlated. Theiler suggested to remove this effect by ignoring all pairs of points in Eq. 4.13 whose time indices differ by less than  $w$ , where  $w$  is chosen at will and  $w \ll N$ . We found  $D$  to be  $2.96 \pm 0.05$  using the current trace for an applied voltage of  $100V$  and  $R = 4$ . The correlation dimension was analyzed for  $\epsilon$  between  $3.17e-14$  and  $5.17e-13$ . The correlation dimension was ensured to be converged for different values of  $m$  ( $m = 20 - 40$ ). The embedding dimension  $m$  is typically greater than  $2D + 1$ . Hence, the embedding dimension ( $m$ ) for the current signal considered is nearly greater than 7. The optimal values of  $\tau$  and  $m$  now can be used to construct the state vector from the scalar current measurements and these values are used to calculate the maximum lyapunov exponent.

It is important to note that one can determine as many different Lyapunov exponents for a dynamical system as there are phase space dimensions. In this study, we restrict ourselves to the calculation of the maximum Lyapunov exponent,  $\lambda^*$ . Let  $\mathbf{I}_{n_1}$  and  $\mathbf{I}_{n_2}$  be two current measurements in the state space with distance  $\|\mathbf{I}_{n_1} - \mathbf{I}_{n_2}\| = \delta_0 \ll 1$ . Let  $\delta_{\Delta n}$  be the distance some time  $\Delta n$  ahead between the two trajectories which are emerging from these

points.

$$\delta_{\Delta n} = \|\mathbf{I}_{n_1+\Delta n} - \mathbf{I}_{n_2+\Delta n}\| \quad (4.16)$$

Then  $\lambda^*$  is given by  $\delta_{\Delta n} \approx \delta_0 e^{\lambda^* \Delta n}$ ;  $\delta_{\Delta n} \ll 1$  and  $\Delta n \gg 1$ . If  $\lambda^*$  is positive, then we observe an exponential divergence of nearby trajectories, resulting in chaos. To calculate  $\lambda^*$ , we choose a point  $\mathbf{I}_{n_0}$  of the time series data in the embedding space and select all neighbours with distance smaller than  $\epsilon$ , which is the order of resolution of the measurements. We compute the average over the distance of all neighbours to the reference part of the trajectory as a function of relative time. The logarithm of the average distance at time  $\Delta n$  gives the expansion rate over the time span  $\Delta n$ . We repeat this procedure for different values of  $n_0$  so that the fluctuations of expansion rate  $\lambda^*$  will average out. Thus, we compute

$$S(\Delta n) = \frac{1}{N} \sum_{n_0=1}^N \ln \left( \frac{1}{|U(\mathbf{I}_{n_0})|} \sum_{\mathbf{I}_n \in U(\mathbf{I}_{n_0})} |I_{n_0+\Delta n} - I_{n+\Delta n}| \right) \quad (4.17)$$

where  $\mathbf{I}_{n_0}$  are embedding vectors;  $U(\mathbf{I}_{n_0})$  is the neighbourhood of  $\mathbf{I}_{n_0}$  with diameter  $\epsilon$ . Since, we do not know a priori both the embedding dimension  $m$  and optimal distance  $\epsilon$ , we compute  $S(\Delta n)$  for both values. However, we know the lower limit of  $m$  from the correlation dimension  $D$ , which is calculated before. Further, we choose a large enough  $\epsilon$  such that on average each reference point has at least few neighbours. The slope of  $S(\Delta n)$  vs  $\Delta n$  gives the maximum Lyapunov exponent. We found  $\lambda^*$  to be  $0.055 \pm 0.006$  using the current trace for an applied voltage of  $100V$  and  $R = 4$ . A  $100ns$  data sampling was considered. Positive  $\lambda^*$  indicates an exponential divergence of the current trace, resulting in a chaotic signal. We repeat the analysis for different values of  $m > 7$  and the maximum Lyapunov exponent converges with  $m$ .  $\lambda^*$  is normalized as we consider the time scale in the units of time index of measurements and not the real time units. We use TISEAN software package to calculate  $\lambda^*$ .

## 4.7 Conclusions

In conclusion, we presented a numerical study of a nanopore connected to fluidic reservoirs of asymmetric geometries. This system exhibits local non-equilibrium chaotic motion of ions under the action of an applied electric field. We revealed the mechanism for chaotic currents to the dynamic clustering of ions, resulting in the creation of an avalanche zone near the drain micro-nanopore interface. Further, we correlated the  $1/f$  type dynamics in the power spectral density to the voltage dominant chaos and  $1/f^2$  type dynamics in the PSD analysis to the macropore reservoir dominant chaos. Further, we quantified chaos by calculating the growth rate of current dynamics in terms of the maximum Lyapunov exponent. Finally, our simulations revealed that reservoir asymmetry plays a pivotal role compared to the magnitude of the applied voltage to observe chaos in nanoporous systems. We believe, the origin of current dynamics discussed in this chapter would help improve the design of ionic diodes and electroosmotic pumps using asymmetric reservoir-nanopore systems.

## 4.8 Figures

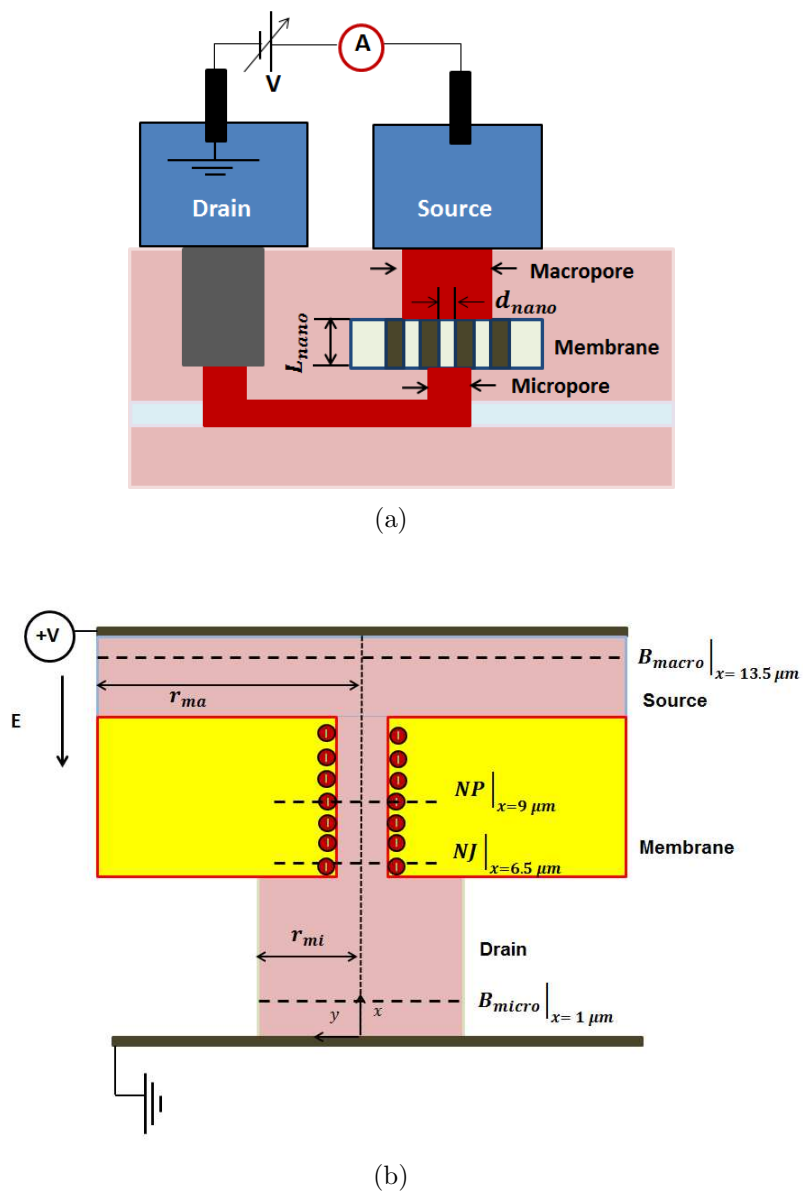


Figure 4.1: (a) Schematic illustration of multiple nanopores interacting with asymmetric fluidic reservoirs (b) Simulation set-up of a single micro-nano-macropore system. The electric field is applied from macropore to micropore reservoir. Ionic current is calculated at four different regions, namely at bulk micropore reservoir ( $B_{micro}$ ,  $x = 1 \mu m$  from the origin), nanopore junction ( $NJ$ ) at a distance of  $0.5 \mu m$  from the micro/nanopore entrance, center of the nanopore ( $NP$ ,  $x = 9 \mu m$  from the origin) and bulk macropore reservoir ( $B_{macro}$ ,  $x = 13.5 \mu m$ ).

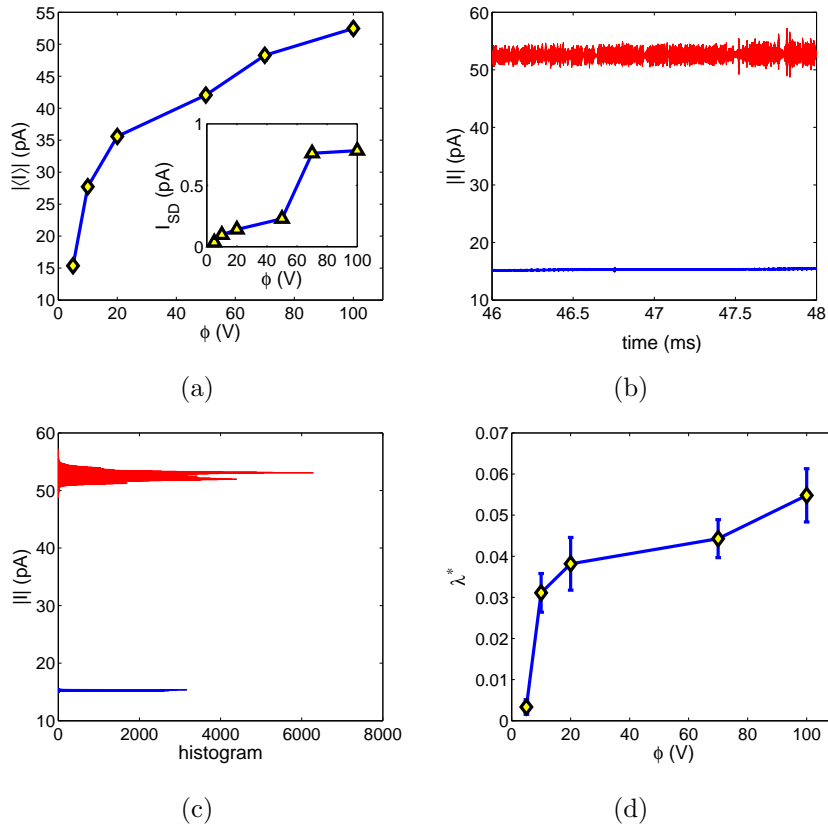


Figure 4.2: Variation of output current (in magnitude) at the center of the nanopore with (a) applied voltage (current is averaged over  $4ms$  time interval for each voltage); inset shows the variation of the standard deviation of the current, over the time interval considered for each voltage (b) time (data collected for last  $2ms$ ) and (c) its corresponding histogram for  $5V$  (solid blue line) and  $100V$  (solid red line), respectively. (d) Variation of maximum Lyapunov exponent with applied voltage. The ratio of macropore to micropore reservoir diameter is 4 in Fig. 4.2(a) to Fig. 4.2(d).

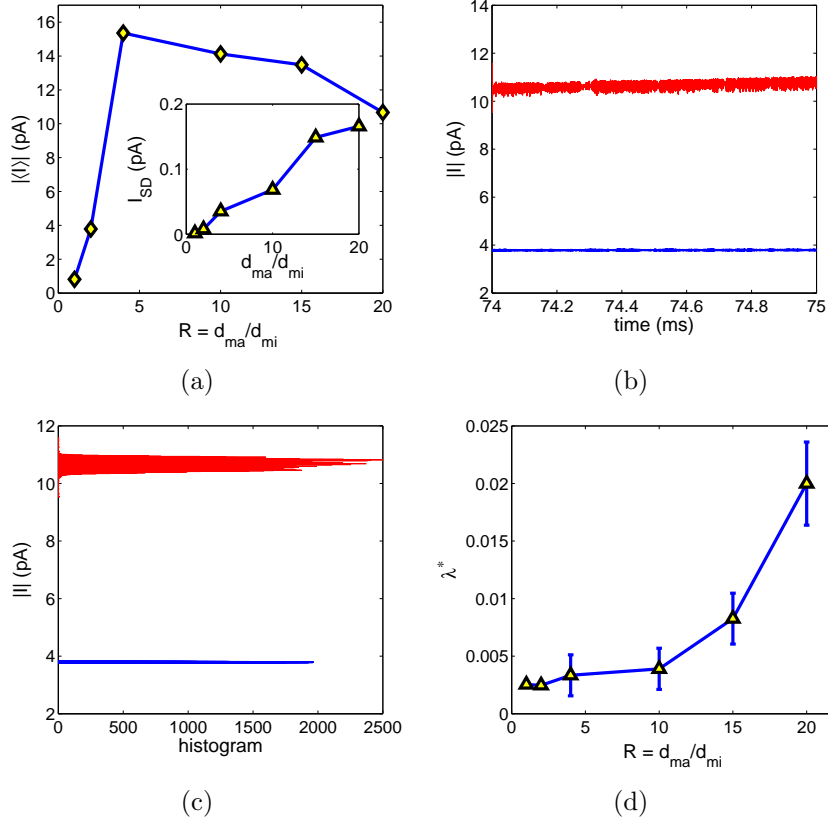


Figure 4.3: Variation of output current (in magnitude) with (a) macropore to micropore radius ( $R = d_{ma}/d_{mi}$ ), current is averaged over  $4ms$  time interval for each  $R$ ); inset shows the variation of the standard deviation of the current, over the time interval considered for each  $R$  (b) time (data collected for last  $1ms$ ) and (c) its corresponding histogram for  $R = 2$  (solid blue line) and  $R = 20$  (solid red line), respectively.(d)Variation of maximum Lyapunov exponent with  $R$ . The applied voltage is  $5V$  and the micropore reservoir diameter is  $0.05\mu m$  in Fig. 4.3(a) to Fig. 4.3(d).

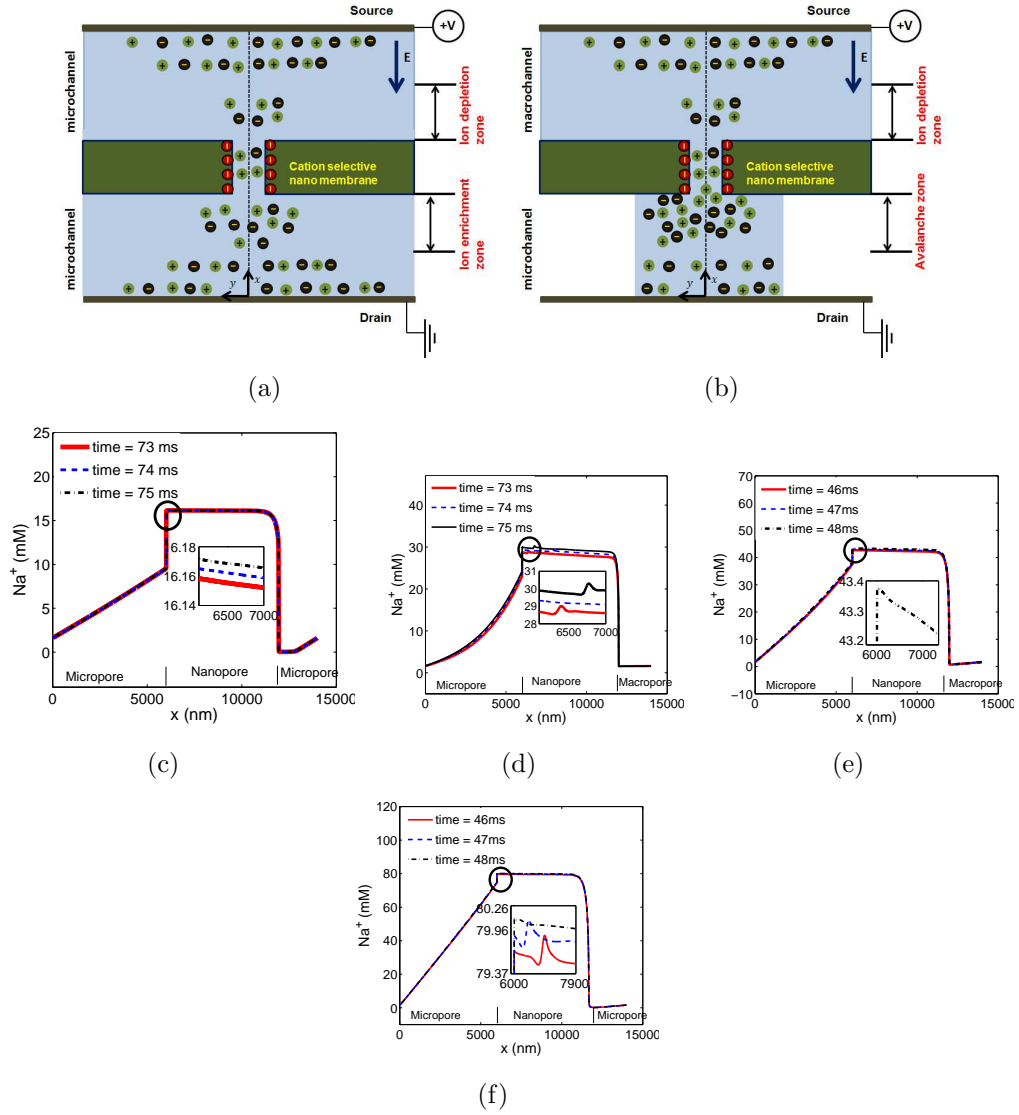


Figure 4.4: Avalanche effect mechanism for (a) a symmetric reservoir ( $R = 1$ ), ions are enriched near the drain micro–nanopore interface and an ion depletion zone is developed near the source micro–nanopore interface. (b) an asymmetric reservoir ( $R > 1$ ), cluster of ions accumulate near the micro–nanopore interface, an “Avalanche zone” is created, and a relatively weak ion depletion zone is developed near the nano–macropore interface. Concentration distribution of sodium ions (counter–ions) along the source–nanopore–drain reservoir system for (c) 5V and  $R = 1$ , inset reveals distribution of an ion enriched zone, (d) 5V and  $R = 20$ , inset reveals dynamic clustering of ions near micro–nanopore interface (e) 5V and  $R = 4$ , inset reveals weak oscillation of ions near the enriched zone and (f) 100V and  $R = 4$ , inset reveals strong enrichment of ions and an inhomogeneous distribution of ions near the enriched micro–nanopore interface.

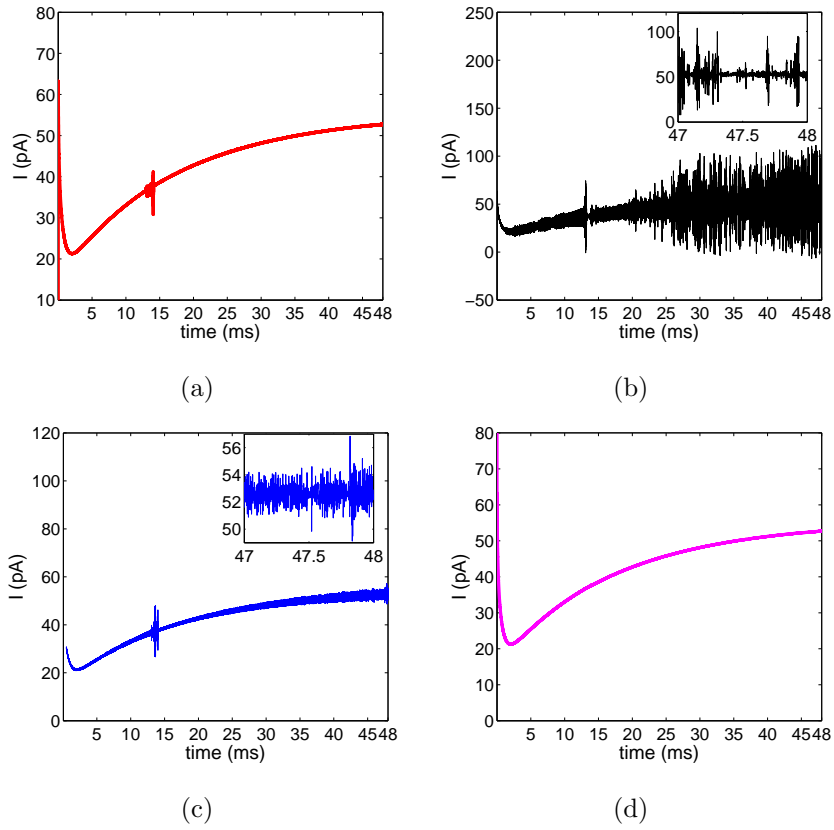


Figure 4.5: Current–time dynamics at (a) bulk micropore ( $x = 1\mu m$ ) (b) nano-junction ( $x = 6.5\mu m$ ) (c) center of nanopore ( $x = 9\mu m$ ) (d) bulk macropore ( $x = 13.5\mu m$ ). The macropore reservoir diameter is  $0.2\mu m$ , micropore reservoir diameter is  $0.05\mu m$ . Ratio of macropore to micropore reservoir is 4. The applied voltage is  $100V$ .

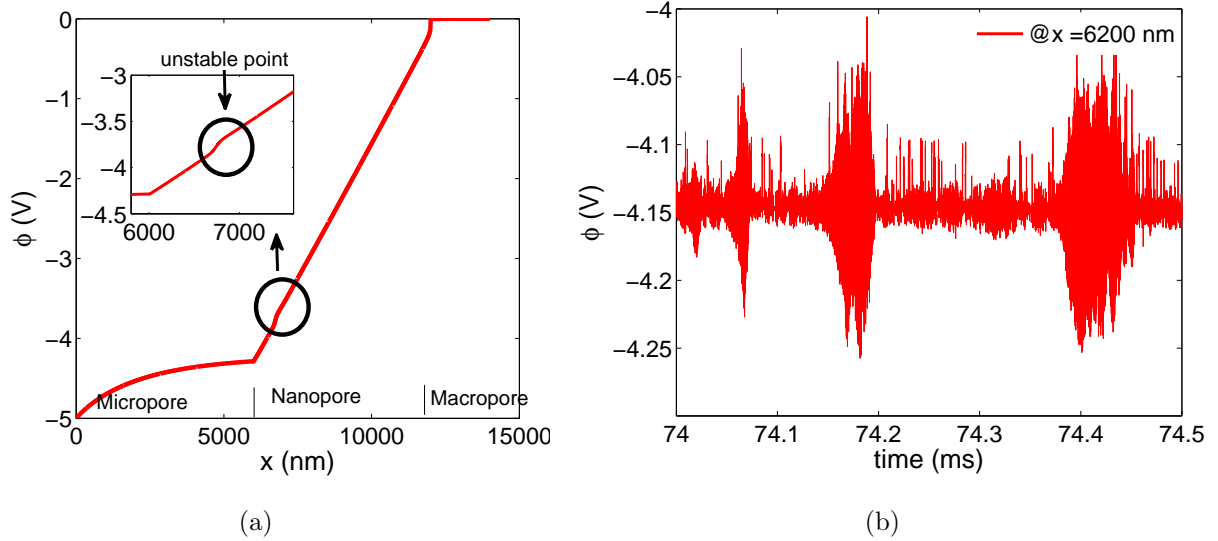
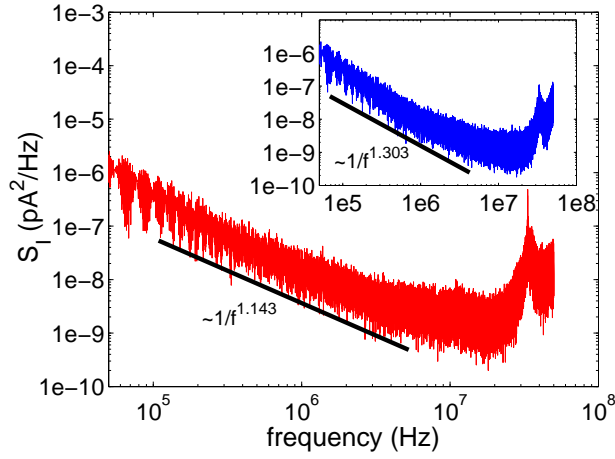
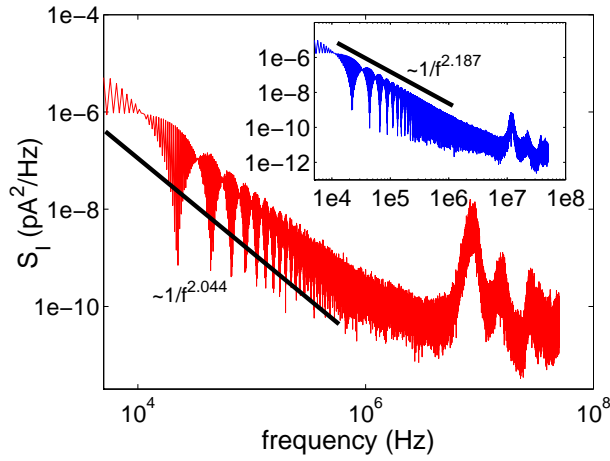


Figure 4.6: Variation of potential (a) along the micro–nano–macropore system. The inset reveals the unstable potential distribution near the enriched micro–nanopore interface (b) with time near the enriched micro–nanopore interface. The macropore reservoir diameter is  $1\mu m$ , micropore reservoir diameter is  $0.05\mu m$ . Ratio of macropore to micropore reservoir is 20. The applied voltage is  $5V$ .



(a)



(b)

Figure 4.7: Power spectral density (PSD) analysis for (a) an applied voltage of 100V, inset shows PSD for 70V,  $R = 4$  is used for both the applied voltages (b) a macropore diameter of  $1\mu m$ , inset reveals PSD for  $0.5\mu m$ . The applied voltage is 5V.

## 4.9 References

1. [Schoch and et al.(2008)] R. B. Schoch, et al., Rev. Mod. Phys. 80 (2008) 839883.
2. [Dekker(2007)] C. Dekker, Nat. Nanotechnol. 2 (2007) 209215.
3. [Chen and et al.(2010)] Z. Chen, et al., Nat. Mater. 9 (2010) 667675.
4. [Kasianowicz and et al.(1996)] J. J. Kasianowicz, et al., Proc. Natl. Acad. Sci. 93 (1996) 1377013773.
5. [Kim and et al.(2007)] S. J. Kim, et al., Phys. Rev. Lett. 99 (2007) 044501.
6. [Siwy and et al.(2002)] Z. Siwy, et al., Phys. Rev. Lett. 89 (2002) 198103.
7. [Toro(1999)] E. F. Toro, Riemann Solvers and Numerical Methods for Fluid Dynamics, SpringerVerlag, 1999.
8. [<http://www.openfoam.com/>(2011)] <http://www.openfoam.com/>, 2011.
9. [Yossifon and et al.(2008)] G. Yossifon, et al., Phys. Rev. Lett. 101 (2008) 254501.
10. [Chang and et al.(2008)] G. Yossifon, et al., Phys. Rev. E 79 (2009) 046305.
11. [Rubinstein and et al.(2009)] I. Rubinstein, et al., Phys. Rev. E. 80 (2009) 021505.

# Chapter 5

## Unraveling the physics of nonequilibrium $1/f$ dynamics in nano-porous membranes

### 5.1 Abstract

In this letter, we numerically investigate the ion transport dynamics inside a near-ideal ion-selective nanoporous membrane connected to microfluidic reservoirs. At high Dukhin number ( $Du \gg 1$ ) and under the action of electric field, we observe, a transition from the stable ionic current to the unstable/chaotic current oscillations inside the nanopore conjecturing to surface effects. The chaotic current response is quantified by calculating the growth rate in terms of the maximum Lyapunov exponent. The maximum Lyapunov exponent monotonically increases with the Dukhin number and is independent of the applied voltage. The current oscillations are due to the propagation of the ion depletion region from the microfluidic reservoir towards the nanopore owing to the nonequilibrium instability in the potential. The potential instability triggers bidirectional ion hopping, corroborating in chaotic motion of the ions. We establish a correlation between the temporal power spectral density and the chaotic current oscillations and thus hypothesize a new mechanism for  $1/f$  type dynamics in nanoporous membranes.

Investigating the dynamics of ion transport in nanoporous membranes is important because the current-time signal is the main detection mechanism in single molecule analysis[Howorka et al.(2009)and Saleh et al.(2003)],DNA-sequencing[Chen et al.(2010),Chang et al.(2004) and Heng et al.(2004)] and in the investigation of local structures along single-bound

proteins[Kasianowicz et al.(1996)]. However, in the recent literature, the ion dynamics are often correlated to equilibrium or non–equilibrium noise inside the nanoporous membranes[Kim et al.(2007), Yossifon et al.(2008), Chang et al.(2008) and Siwy et al.(2002)]. This suggests that the ion fluctuations are usually considered to be stochastic in origin. Further, the temporal power spectra map of the ionic fluctuations has a  $1/f$  type noise characteristics in the low frequency regime. The physical origin of the  $1/f$  type dynamics is still unclear. In a recent publication, The  $1/f$  type of noise is attributed to the inherent dynamic properties of the solution, i.e., to the fluctuations of the ionic diffusivity and its corresponding ionic mobility. Another possible mechanism correlates to the nanopore wall surface charge fluctuations. Other mechanisms include conformational changes of the pore structural constituents and the formation of a nanobubble inside the nanopore.

In this chapter, we discuss a new route for “ $1/f$ ” dynamics which could have an alternative origin. We present a single nanoporous membrane connected to microfluidic reservoirs typically considered for single molecule sensing and DNA sequencing applications. For a near ideal cation–selective nanopore, i.e., when the cation transference number (given by the ratio of the cationic current to the total ionic current) is near unity ( $t_+ = \frac{I_+}{I_{total}} \approx 1$ ), we numerically observe novel chaotic current oscillations. The near ideal ion–selective nanopore is achieved at a high Dukhin number ( $Du \gg 1$ ), when the surface charge density is higher than the bulk density,  $Du = \frac{2|\sigma_s|}{Fc_0r_n}$ .  $\sigma_s$  is the surface charge density on the walls of the nanopore,  $c_0$  is the bulk concentration of the ions,  $r_n$  is the radius of the nanopore and  $F$  is Faraday constant. At a high Dukhin number ( $Du > 40$ ), the ions near the anode micro–nano junction are depleted and the depletion region propagates inside the nanopore. This leads to a non–homogenous distribution of ionic concentration, thereby resulting in a nonequilibrium instability in potential. The ions hop between these potential wells resulting in chaotic current oscillations.

We present a numerical model of a single cylindrical nanopore connected to a microfluidic reservoir of a few hundreds of nanometers in diameter. We investigate the axial changes in

the potential ( $\phi$ ) and individual ionic concentration ( $c_i$ ) by averaging the effects in the radial direction. We discuss the details of the mathematical model in our earlier work. We briefly highlight the model in this manuscript.

The mass transfer of each buffer species is,

$$A(x)\frac{\partial \hat{c}_i}{\partial t} = \frac{\partial}{\partial x} \left( A(x)D_i \frac{\partial \hat{c}_i}{\partial x} \right) + \frac{\partial}{\partial x} \left( \frac{z_i D_i F}{RT} A(x) \hat{c}_i \frac{\partial \hat{\phi}}{\partial x} \right) \quad (5.1)$$

where,  $A(x)$  is the cross-sectional area, which is a function of the axial direction.  $D_i$ ,  $\hat{c}_i$  and  $z_i$ , denote the diffusion coefficient, molar concentration, and valence of each ion, respectively.  $R$  is the ideal gas constant and  $T$  is the thermodynamic temperature.  $\hat{f} = \frac{1}{A} \int_0^r \int_0^{2\pi} (f(r, \theta)) r \, d\theta dr$  denotes the area-averaged quantity. The first term on the right hand side accounts for the ionic diffusive effects, while the second term accounts for the electromigration/electroconvective effects inside the system. The electrostatic potential ( $\hat{\phi}$ ) in the axial direction is,

$$\frac{\partial}{\partial x} \left( A(x) \frac{\partial \hat{\phi}}{\partial x} \right) = -\frac{FA(x)}{\epsilon} \left( \sum_{i=1}^n z_i \hat{c}_i + \frac{4\sigma_s(x)}{Fd(x)} \right) \quad (5.2)$$

where  $n$  is the number of ionic species in the solution and  $d(x)$  is the diameter of the pore, varying in the axial direction.  $\sigma_s(x)$  denotes the wall surface charge density, corresponding to the nanopore. Furthermore, the model assumes an ideal nonpolarizable electrode and hence, we neglect the Faradaic reactions that occur near the electrode. We consider sodium monobasic and sodium dibasic ionic solution, and assume that the ions inside the Steric layer are rigidly held and do not contribute to the ionic current[Rubinstein et al.(2009)]. We consider an isotropic medium with a constant dielectric permittivity  $\epsilon = \epsilon_0 \epsilon_r$ .  $\epsilon_0$  is the permittivity of free space and  $\epsilon_r$  is the relative permittivity of the medium. Under these assumptions, the total current density ( $\hat{\Gamma}_{tot}$ ), through the pore is  $\hat{\Gamma}_{tot} = F \sum_{i=1}^n z_i \Gamma_i$ , where  $\Gamma_i = -D_i \frac{\partial \hat{c}_i}{\partial x} - \frac{z_i F D_i}{RT} \hat{c}_i \frac{\partial \hat{\phi}}{\partial x}$  is the total flux of each ionic species, contributed by a diffusive

component resulting from the concentration gradient, and an electric migration component due to the electric field interaction with the ionic concentration.

We numerically simulate a cylindrical nanopore of length  $L_n = 500nm$ , and diameter  $d_n = 10nm$ . The nanopore is connected to two micropore reservoirs of length  $L_{mi} = 4\mu m$ , diameter  $d_{mi} = 500nm$ . The voltage is systematically varied from  $0V$  to  $100V$  and the direction of the electric field is shown in Fig. 5.1. Phosphate buffer of constant concentration ( $0.39mM$  of  $NaH_2PO_4$  and  $0.61mM$  of  $Na_2HPO_4$ ) is used in all the simulations and the temperature is,  $T = 300K$ . The diffusivities of  $Na^+$ ,  $H_2PO_4^-$  and  $HPO_4^{2-}$  are  $1.33 \times 10^{-9}m^2/s$ ,  $0.879 \times 10^{-9}m^2/s$ , and  $0.439 \times 10^{-9}m^2/s$ , respectively. We assume the dielectric constant of the aqueous solution to be,  $\epsilon_r = 80$ . The surface charge density on the walls of the micropore is assumed to be zero,  $(\sigma_s(x)|_{micropore} = 0)$ . Dukhin number is varied from 0 to 124.37 by varying the nanopore wall surface charge density.

Fig. 5.2(a) shows the variation of current at the center of the nanopore with systematic increase in the Dukhin number. The output current,  $\langle I \rangle$  is averaged over  $5ms$ . At low Dukhin number, the current is primarily dominated by the bulk motion of both co-ions (anions) and counter-ions (cations) as the cation transference number is around 0.6 (see inset of Fig. 5.2(a)). With increase in the Dukhin number, i.e., as the surface charge density increases, the cation transference number reaches unity, resulting in a near-ideal nanoporous membrane. Further, owing to the dominance of surface conductivity, the total current decreases at high  $Du$ . In order to understand the current dynamics, we investigate the numerical current-time data. We simulate the long time current dynamics for  $13ms$  with a time step of  $10ns$ . At  $Du = 0$ , we observe a steady distribution of the current signal at the center of the nanopore (Fig. 5.2(b)). However, at high  $Du$ , we observe non-equilibrium current oscillations. Fig. 5.2(b) reveals that the current oscillates between  $77pA$  and  $-34pA$  indicating that the ions switch their direction dynamically inside the nanopore. In order to quantify the non-equilibrium current oscillations, we calculate the growth rate quantified by the maximum Lyapunov exponent ( $\lambda^*$ ). The sign of the maximum Lyapunov exponent

determines the stability of the signal. Fig. 5.2(c) reveals a negative Lyapunov exponent (negative growth rate) for low  $Du$  illustrating a steady and stable current signal. However, at high  $Du$ , we observe a transition from negative to positive Lyapunov exponent, indicating unstable/chaotic current signal. The magnitude of stable and unstable currents with  $Du$  is highlighted in Fig. 5.2(a).

We examine the effect of the applied electric potential,  $\phi^*$  on the current at a fixed  $Du$ ; when the cation transference number is near unity. The average current is independent of the applied voltage(see Fig. 5.2(d)) owing to the ideal nature of the membrane, due to the fixed concentration of the counter-ions inside the nanopore. Fig. 5.2(e) reveals current oscillations at an applied non-equilibrium potential,  $\phi^*$ . We calculate the maximum Lyapunov exponent for each applied voltage, and we observe a positive ( $\lambda^*$ ) for non-zero potentials. Furthermore, the maximum Lyapunov exponent is independent of the applied voltage in agreement to the applied current. We use TISEAN software package to calculate  $\lambda^*$ .

In order to reveal the mechanism behind the non-equilibrium current oscillations, we probe into the potential and concentration distribution along the micro-nanopore system. At a low Dukhin number, and under non-equilibrium potential, Fig. 5.3(a) shows that the majority of the voltage drops linearly inside the nanopore and the potential does not change dynamically. The linear voltage drop results in a constant electric force acting on the ions and hence, we observe a steady transport of ions. This results in a stable ionic current. However, at large Dukhin number, and when the system is in equilibrium, Fig. 5.3(b) shows a double potential well inside the nanopore with a barrier of 0.004 times the thermal voltage. At this state, majority of the ions tend to reside at the two stable potential wells and also the potential does not change with time. The unstable potential barrier at equilibrium suggests that a small electric perturbation whose magnitude is greater than the barrier would result in non-equilibrium instability in the potential, with a net transport of ions. Furthermore, under this instability, Fig. 5.3(c) shows that the potential dynamically changes resulting in

bi-directional hopping of the ions, thereby changing the directionality of the currents.

Next, we probe into the concentration distribution along the micro-nanopore system (see Fig. 5.3(d) and Fig. 5.3(e)). At high  $Du$ , the co-ions are attracted towards the anode and are repelled from the ideal cation-selective nanopore, resulting in a depletion of these ions at the anode micro-nanojunction. In order to maintain electroneutrality, the counter-ions are depleted at this junction. However, the co-ions and the counter-ions get accumulated near the cathode micro-nanojunction owing to the concentration polarization effects. In the non-equilibrium regime, the depletion region propagates inside the nanopore (the solid arrow in Fig. 5.3(d) shows the direction of propagation of the ions) resulting in a non-homogeneous distribution of the ionic concentration, which is more evident from Fig. 5.3(e). The non-equilibrium instability in the potential manifests in this result. The instability in the potential and the corresponding concentration distribution together results in non-equilibrium chaotic current oscillations at high  $Du$ . A schematic illustration of this mechanism is highlighted in Fig. 5.3(f).

We probe into the unstable current-time signal by analyzing the power spectra. Temporal power spectral density is analyzed between a frequency range of 0 to 50 MHz. The power spectral density ( $S_I$ ) is computed using the Welch method. We considered 6ms current-time data. The current signal is divided into longest sections to obtain close to but not to exceed 8 segments, with 50% overlap. Each section is windowed with a Hamming window. The signal is sampled with a sampling frequency ( $f_s$ ) of 100MHz. The spectral estimate is then calculated by averaging the modified periodograms for a frequency range  $[0 - f_s/2]$ . Fig. 5.4(a) shows the power spectra map for different  $Du$ . The power spectral density follows a power law dependence ( $1/f^\alpha$ ) with respect to frequency, in the low frequency range from 70.2kHz to 1MHz. The exponent  $\alpha$  is close to 1 in this frequency range. Furthermore, we observe similar  $1/f$  type dynamics, under the action of electric field, at  $Du = 124.37$  as shown in Fig. 5.4(b). Our results help us to postulate that there is a strong correlation between nonequilibrium chaotic current dynamics to  $1/f$  type dynamics in nanoporous membranes.

The findings help us to conclude that  $1/f$  type dynamics can have a deterministic origin unlike earlier theories.

In conclusion, we numerically investigate the ion transport dynamics in nanoporous membranes connected to microfluidic reservoirs. We observe a clear transition from stable and steady ion transport to unstable/chaotic current oscillations as the cation transference number reaches unity (under near-ideal nanoporous membrane), upon systematic variation of the Dukhin number. We postulate the mechanism behind the chaotic current oscillations to the propagation of depletion region inside the nanopore, and the non-homogeneous distribution of the ions owing to the nonequilibrium instability in the potential. This instability also manifests in bi-directional hopping of the ions, thereby changing the directionality of the currents. Furthermore, we confirm the chaotic current oscillations in terms of the maximum Lyapunov exponent, revealing a positive growth rate. Finally, we establish a correlation between the low frequency  $1/f$  type dynamics to the chaotic current, and postulate a new mechanism for nonequilibrium  $1/f$  type dynamics.

## 5.2 Figures

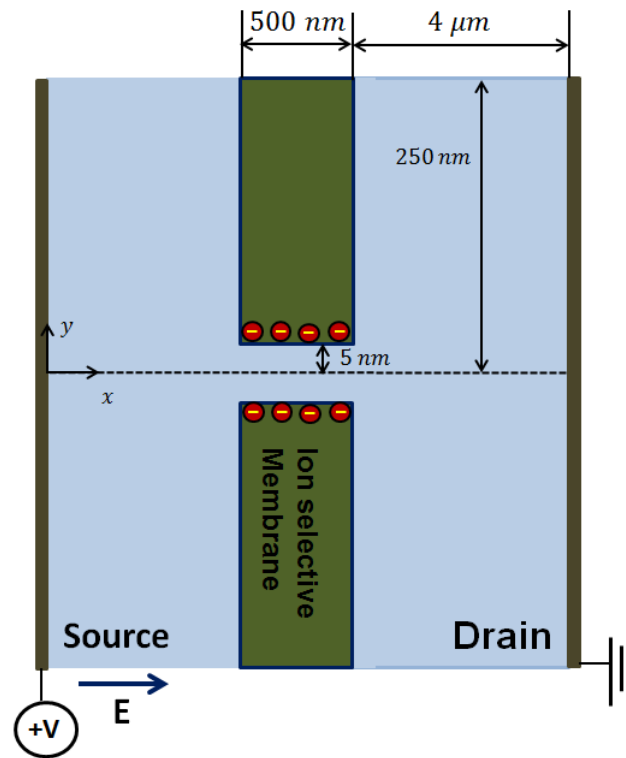


Figure 5.1: A schematic representation of a micro–nanopore simulation set up. The electric field is directed from the source to the drain reservoir.

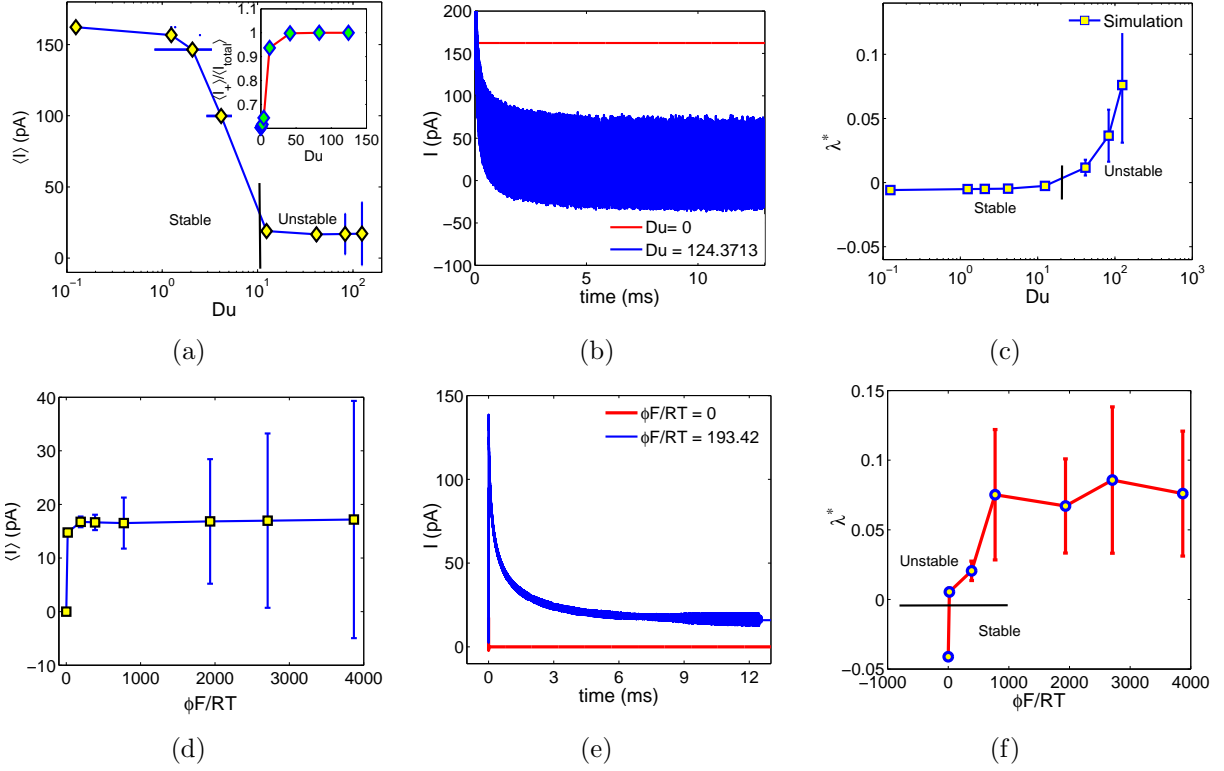


Figure 5.2: (a) Variation of the numerical current with the Dukhin number at an applied voltage of  $\phi^* = 3868.387$ . The inset reveals the cation transference number dependence on the  $Du$ . (b) Current–time signal at low (red line) and at high  $Du$  (blue line). (c) Simulation results of the variation of the maximum Lyapunov exponent ( $\lambda^*$ ) with the  $Du$ .  $\lambda^*$  is normalized as we consider the time scale in the units of time index of measurements. (d) Variation of the current with the applied voltage at  $Du = 124.37$ . (e) Current–time response at equilibrium (red line) and non–equilibrium potential,  $\phi^* = 193.42$  (blue line). (f) Variation of the maximum Lyapunov exponent with the applied voltage. The current is averaged over  $5ms$  time interval for all data.

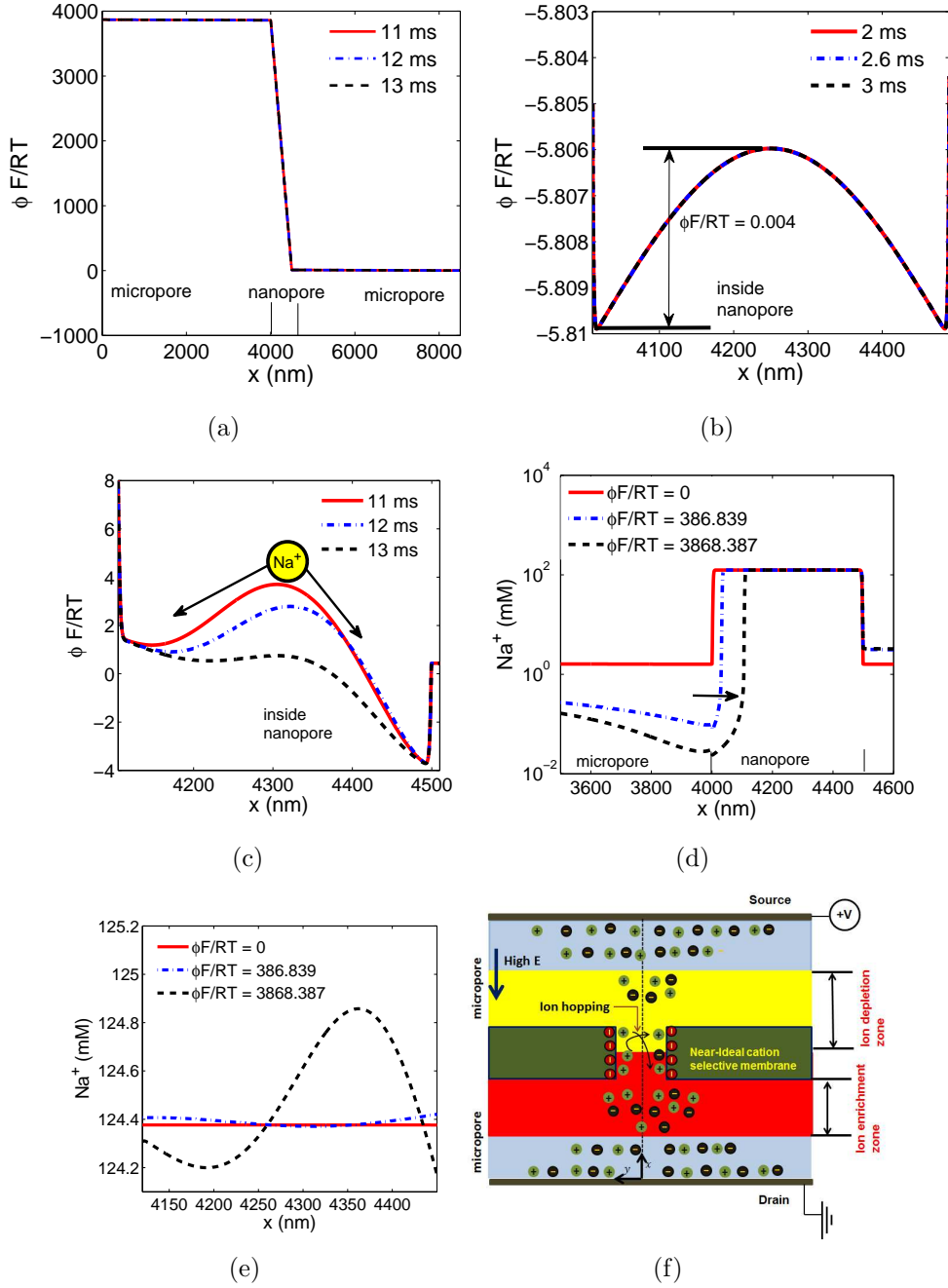


Figure 5.3: Axial potential distribution along the micro–nanopore at (a) nonequilibrium potential,  $\phi^* = 3868.387$  and  $Du = 0$ , (b) equilibrium, for  $Du = 124.37$  (c) nonequilibrium potential,  $\phi^* = 3868.387$  and  $Du = 124.37$ . Axial sodium ion concentration distribution along (d) micro–nanopore system. The solid arrow reveals the propagation of depletion region inside the nanopore. (e) Non–homogeneous concentration distribution inside the nanopore. (f) A schematic representation of the mechanism for chaos.

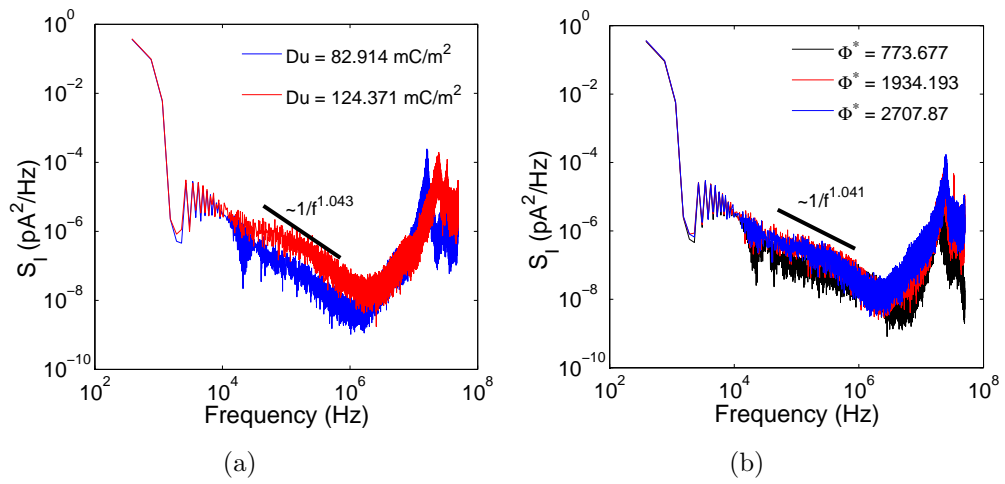


Figure 5.4: Power spectral density as a function of frequency for (a) different Dukhin number at  $\phi^* = 3868.387$  and (b) various nonequilibrium potential, at  $Du = 124.37$ .

## 5.3 References

1. [Howorka and et al.(2009)] S. Howorka, et al., Chem. Soc. Rev. 38 (2009) 23602384
2. [Saleh and et al.(2003)] O. A. Saleh, et al., Nano Lett. 3 (2003) 3738.
3. [Chen and et al.(2010)] Z. Chen, et al., Nat. Mater. 9 (2010) 667675.
4. [Chang and et al.(2004)] H. Chang, et al., Nano Lett. 4 (2004) 15511556.
5. [Heng and et al.(2004)] J. B. Heng, et al., Biophys. J. 87 (2004) 29052911.
6. [Kasianowicz and et al.(1996)] J. J. Kasianowicz, et al., Proc. Natl. Acad. Sci. 93 (1996) 1377013773.
7. [Kim and et al.(2007)]S. J. Kim, et al., Phys. Rev. Lett. 99 (2007) 044501.
8. [Yossifon and et al.(2008)] G. Yossifon, et al., Phys. Rev. Lett. 101 (2008) 254501.
9. [Chang and et al.(2008)] G. Yossifon, et al., Phys. Rev. E 79 (2009) 046305.
10. [Siwy and et al.(2002)] Z. Siwy, et al., Phys. Rev. Lett. 89 (2002) 198103.

# Chapter 6

## Super large velocity in osmotic nano pumps

### 6.1 Abstract

In this article, we present a novel AC electroosmotic nanofluidic pump (ACEOP) that does not need the complex electrode array structures used in an AC microfluidic electroosmotic pump. Further, we preserve the nanopore symmetry and do not require a conical nanopore or a surface diode. Instead, asymmetric concentration polarization (CP) is used to produce a net electroosmotic flow (EOF). An asymmetric CP zone is created by introducing an asymmetry in the reservoir geometry connected to the nanopore. The reservoir geometry with larger diameter is referred to as the macropore, while, the other reservoir diameter is referred to as the micropore. Numerical simulations reveal the mean electroosmotic flow (EOF) observed in our experiments under an AC field, is due to the out of phase behavior between the first harmonic mode of the space charge density and the electric field. The asymmetric concentration polarization is responsible for the generation of higher harmonic modes in the space charge density and gives rise to the out of phase behavior. The direction of EOF is from macropore towards micropore for a frequency range  $0.5Hz$  to  $5Hz$ . The net EOF can be controlled by varying the amplitude of AC field and its frequency. The maximum EOF achieved by our pump is 400% higher than other ACEO nanofluidic pumps, and our design is compatible compared to ACEO microfluidic pumps. Further, bubble generation can be controlled by this technique.

## 6.2 Introduction

The advent in technology of fabricating devices of the order of a few micro/nanometers have paved way for single molecule sensing[Howorka et al.(2009)], DNA sequencing, water desalination and protein translocation. A key functionality in these systems is the ability to pump fluids, ions and other biomolecules through the micro/nanochannels. Traditional pressure-driven flows (mechanical pumps) can not be used for the pumping applications. Further, pressure pumps are not easily portable as these devices require complicated off-chip plumbing. Hence, electric field is applied to achieve pumping mechanism [Chen et al.(2010), Piruska et al.(2010), Kim et al.(2007)]. In electric field driven pumps, there are two types of transport, electroosmotic flow (EOF) and electrophoretic flow. EOF refers to the movement of uncharged liquid (typically water) relative to a stationary charged surface under the action of an external electric field. Electroosmotic pumps can be fabricated using standard microfabrication technologies and thus can be readily integrated with lab-on-chip (LOC) devices. Further, EOP's do not require any moving part unlike the mechanical pumps. In most of the EOP design, the fluid is typically driven under the action of a DC electric field[Qiao et al., Jin et al.(2007), Mani et al.(2009) and Postler et al.(2008)]. An ongoing challenge of using a DC electric field is bubble formation on the electrodes and reservoir pH variation due to electrolysis [Choi et al.(2009), Pu et al.(2004)].

In order to overcome these challenges, a significant amount of work has been done to design an electroosmotic pump in microfluidic channels, using periodic electric potential (ACEOP). To generate a net electroosmotic flow (EOF) using an AC field, the symmetry of the system has to be broken. To this end, a complex asymmetric planar electrode structure is fabricated on the microfluidic channel and an AC electric field is applied on these electrodes. Asymmetry in the geometry of the pair of electrodes generates a nonuniform electric field. The component of the ac field normal to the electrode surface induces charge in the double layer, while the tangential component results in a body force on the induced charge,

thereby generating a net EOF. A 3D electrode structure on the microchannel walls instead of the planar electrodes is conferred to increase the net EOF. Net electroosmotic flow was also induced by applying a traveling-wave electric potential on an array of microelectrodes. An asymmetric planar electrode design on the walls of nanometer-sized channels is set forth. However, the EOF generated was 50 times smaller compared to microfluidic systems. Further, the design involves many challenges to fabricate electrodes on the nanochannel walls. One of the ways to overcome this design problem is to break the symmetry in the nanopore geometry or nanopore surface chemistry and achieve net fluid flow using an AC electric field. AC field can be applied across the electrodes placed at the ends of the reservoirs. Conical nanopores are an example of asymmetry in the nanopore geometry. Conically shaped pores have a diameter of the order of few nanometers on the “tip” side and a diameter of order of few microns on the “base” side. The device helps in rectifying ionic current, resulting in higher currents when the electric field is directed from tip to base direction compared to the currents generated when the polarity of voltage is reversed. An alternative demonstration includes a cylindrical nanopore with asymmetric surface charge distribution to rectify ionic current. In these devices, half of the nanopore wall was coated with biotin, which imparts a neutral surface charge; while avidin was bound to the other half of the nanopore surface, which imparts a positive charge. Both these rectifying devices have the potential to be used as ACEO pumps. However, there are still fabrication challenges in both these designs since we need to manipulate at the nanoscale level to break the symmetry.

In this article, we demonstrate an AC electroosmotic nanofluidic pump. In this design, we do not manipulate the geometry or surface pore of the nanopore, but achieve an asymmetry by manipulating the geometry of the reservoirs. We fabricate the reservoirs consisting of two different diameters. The larger reservoir diameter is referred to as the macropore, while the smaller diameter reservoir is referred to as the micropore. Previously, the current rectification was postulated by changing the geometry of the reservoirs . The physical mechanism for the current rectification is the change in the cross-sectional areas of the fluidic

reservoirs and the polarity dependent propagation of the enriched and depleted concentration polarization zones into these regions. In this article, we demonstrate that under the action of an external AC electric field, a net electroosmotic flow is achieved owing to the asymmetric reservoir geometry resulting in an asymmetry in the concentration polarization zones. We measure the net flow over  $0.5Hz - 5Hz$  frequency range. We use numerical simulations to qualitatively explain the mechanism behind the net EOF observed in our experiments and the flow direction. Furthermore, we compare the maximum EOF achieved by our design with other ACEO pumps. The maximum EOF achieved in the present work is 400% higher than other ACEO nanofluidic pump and the design is compatible compared to the ACEO microfluidic pumps. Furthermore, the device does not generate bubbles owing to the effects of electric field as we apply a harmonic potential.

## 6.3 Theory

### 6.3.1 Governing Equation

We use continuum theory to model the fluid and ion transport, as continuum model is found to give an accurate description of transport physics for dimensions larger than several nanometers. We assume that the concentration of  $H^+$  and  $OH^-$  is much lower compared to the bulk concentration of the ionic species as the pH of the solution considered is 7, resulting in a concentration of  $H^+$  and  $OH^-$  to be  $1e-7$ . Hence, the water dissociation effects are not considered in the numerical model. Further, we assume that the ions inside the Steric layer are rigidly held and do not contribute to the ionic current. We also neglect the Faradaic reactions that occur near the electrode. Under these assumptions, the total flux of the ionic species is contributed by a diffusive component resulting from the concentration gradient, an electrophoretic component arising due to the potential gradient and a convective component

originating from the fluid flow. The total flux of each species in the solution is given by,

$$\mathbf{\Gamma}_i = -D_i \nabla c_i - \Omega_i z_i F c_i \nabla \phi + c_i \mathbf{u} \quad (6.1)$$

where  $\mathbf{\Gamma}_i$  is the flux vector,  $F$  is Faraday's constant,  $z_i$  is the valence,  $D_i$  is the diffusion coefficient,  $\Omega_i$  is the ionic mobility,  $c_i$  is the concentration of the  $i^{\text{th}}$  species,  $\mathbf{u}$  is the velocity vector of the fluid flow and  $\phi$  is the electrical potential. Note that the ionic mobility is related to the diffusion coefficient by Einstein's relation,  $\Omega_i = \frac{D_i}{RT}$ , where  $R$  is the ideal gas constant and  $T$  is the thermodynamic temperature. The mass transport of each ionic species is,

$$\frac{\partial c_i}{\partial t} = -\nabla \cdot \mathbf{\Gamma}_i \quad (6.2)$$

The individual ionic current through the pore is calculated by integrating their respective fluxes over the cross-sectional area, i.e.,

$$\mathbf{I}_i = \int_S z_i F \mathbf{\Gamma}_i dS \quad (6.3)$$

and the total ionic current through the pore is calculated as,

$$\mathbf{I} = \int_S \sum_i z_i F \mathbf{\Gamma}_i dS \quad (6.4)$$

where  $S$  is the cross-sectional area of the pore. We solve Poisson equation to determine the electrical potential distribution along the system,

$$\nabla \cdot (\epsilon_r \nabla \phi) = -\frac{\rho_e}{\epsilon_0} \quad (6.5)$$

where  $\epsilon_0$  is the permittivity of free space,  $\epsilon_r$  is the relative permittivity of the medium and  $\rho_e$  is the net space charge density of the ions defined as,

$$\rho_e = F \left( \sum_{i=1}^m z_i c_i \right) \quad (6.6)$$

where  $m$  is the total number of species considered in the system. Eq. (6.5), Eq. (6.2) and Eq. (6.3) are the classical Poisson–Nernst–Planck (PNP) equations, which describe the electrochemical transport. The incompressible Navier–Stokes and the continuity equations are considered, to describe the movement of the fluid flow,

$$\rho \left( \frac{\partial \mathbf{u}}{\partial t} + \mathbf{u} \cdot \nabla \mathbf{u} \right) = -\nabla p + \mu \nabla^2 \mathbf{u} + \rho_e \mathbf{E} \quad (6.7)$$

$$\nabla \cdot \mathbf{u} = 0 \quad (6.8)$$

where  $p$  is the pressure,  $\rho$  and  $\mu$  are the density and the viscosity of the fluid, respectively, and  $\mathbf{E} = -\nabla \phi$  is the electric field.  $\rho_e \mathbf{E}$  is the electrostatic body force acting on the fluid due to the space charge density and the applied electric field.

We need the necessary boundary conditions for the closure of the problem. The normal flux of each ion is assumed to be zero on all the pore walls so that there is no outage of current. The fluid velocity on the wall surfaces is assumed to be subjected to non–slip boundary condition and the gradients of pressure are assumed to be zero on the walls. To conserve charge on the walls of the pore, the electrostatic boundary condition is given by,

$$\mathbf{n} \cdot \nabla \phi = \frac{\sigma}{\epsilon_0 \epsilon_r} \quad (6.9)$$

where  $\mathbf{n}$  denotes the unit normal vector (pointing outwards) to the wall surface and  $\sigma$  is the surface charge density of the walls. An AC electric field, with amplitude,  $V_{AC}$  and frequency,  $f$  is applied on the ends of the micro/macropore reservoirs. The boundary conditions at the

ends of the micropore (Eq. (6.10)) and macropore (Eq. (6.11)) are specified as:

$$\phi = 0, \quad c_i = c_o, \quad \mathbf{n} \cdot \nabla \mathbf{u} = 0, \quad p = 0 \quad (6.10)$$

$$\phi = V_{AC} \sin(2\pi ft), \quad c_i = c_o, \quad \mathbf{n} \cdot \nabla \mathbf{u} = 0, \quad p = 0 \quad (6.11)$$

$c_0$  is the bulk concentration of the ionic solution. The coupled PNP and Navier–Stokes equations are numerically solved using the finite volume method in OpenFOAM (Open Field Operation and Manipulation). The details regarding the solver implementation is discussed in our earlier works.

## 6.4 Simulation details

The simulated domain consists of a nanopore of length  $L_n = 0.5 \mu m$  and diameter  $d_n = 13 nm$ . The length of the nanopore is reduced by 100 times compared to the experimental system to reduce the computational cost as the objective of the numerical model is to qualitatively explain the mechanism behind the experimental observations. We considered the micropore of diameter of  $d_{micro} = 50 nm$ , while the macropore diameter,  $d_{macro} = 100 nm$ . The length of the micro and macropore reservoirs is  $L = 1 \mu m$ . An AC voltage is applied across the reservoirs. The frequency of the AC field was varied from  $0.5 Hz - 1 MHz$ , while the amplitude of AC voltage is kept constant, at  $V_{AC} = 10 V$ . Phosphate buffer of constant concentration ( $0.39 mM$  of  $NaH_2PO_4$  and  $0.61 mM$  of  $Na_2HPO_4$ ) is used in all the simulations. The temperature is  $T = 300 K$ . The diffusivities of  $Na^+$ ,  $H_2PO_4^-$  and  $HPO_4^{2-}$  are  $1.33 \times 10^{-9} m^2/s$ ,  $0.879 \times 10^{-9} m^2/s$ , and  $0.439 \times 10^{-9} m^2/s$ , respectively. We assume the dielectric constant of the aqueous solution to be,  $\epsilon_r = 80$ . We also assume zero surface charge density on the walls of the micropore,  $\sigma_m = 0$ , as they are away from the nanopore membrane to have an influence on the transport. The charge on the walls of the nanopore

is assumed to be  $\sigma_n = -0.05mC/m^2$ . Note, the flow direction is positive from micropore to macropore.

## 6.5 Results and Discussion

The experimental system and a 2D schematic illustration consisting of an array of nanopores open to the fluidic reservoirs is shown in Fig. 6.1. An AC electric field is applied across the ends of the reservoirs. Initially, the amplitude of the AC field is kept constant at  $V_{AC} = 100V$ , and the frequency is varied from  $0.5Hz - 5Hz$ . No DC voltage is applied across the system.

We calculate the mean electroosmotic flow velocity  $\langle u_{EOF} \rangle$  over 5 cycles using  $\langle u_{EOF} \rangle = \frac{1}{NT} \int_0^{NT} u_{EOF}(t) dt$ , where  $T$  is the time period of oscillation for each frequency,  $f$  ( $T = \frac{1}{f}$ ) and  $N$  is the number of cycles. Fig. 6.2(a) shows the variation of mean EOF with frequency. The magnitude of mean EOF increases with increase in frequency. The negative sign indicates that the mean EOF moves from macropore towards micropore reservoir. The experiments were performed until  $5Hz$  as that was the maximum frequency that could be achieved using our frequency generator. However, using our numerical simulations we investigate the effect of frequency from  $0.5Hz - 1MHz$  on the EOF. The numerical results and the mechanism behind the net EOF is discussed later in the text.

The dependence of AC amplitude on the experimentally measured mean EOF is depicted in Fig. 6.2(b). Here the frequency of AC field is kept constant at  $f = 1Hz$ , while the AC amplitude is varied from  $10V - 100V$ . We achieve a maximum mean EOF of  $-20.1\mu m/s \pm 2.3\mu m/s$  at  $V_{AC} = 10V$  and the magnitude of mean EOF decreases by 20 times when the AC amplitude is increased by 10 fold. Here, the DC electric field is switched off.

Using numerical simulations, we try to reveal the mechanism behind the net EOF and the direction of the EOF under AC field, in the absence of any DC voltage. A combined Poisson-Nernst-Planck and Navier-Stokes model discussed in the earlier section was solved considering the micro-nano-macropore system. Fig. 6.3(a) shows the simulation results of

the variation of the mean EOF with frequency, varying from  $0.5Hz - 1MHz$ . The mean EOF was calculated at the center of the nanopore, at  $L_{nano} = 250nm$  and  $r = 0$ ,  $r$  is the radial direction. We can clearly observe a non-zero EOF with the application of AC field, and the magnitude of mean EOF varies non monotonically with frequency and reaches a maximum at  $5Hz$ . The direction of EOF is from macropore towards micropore consistent with the experimental observations. To understand the physics behind the net EOF observed in the numerical simulations, we develop a simple theoretical model. We assume the fluid flow is laminar, fully developed and the axial component of the velocity varies only in the radial direction inside the nanopore, and there is no radial velocity. Further, we also assume electric body force ( $\rho_e E_z$ ) is the only force acting in the axial ( $z$ ) direction balanced by the viscous force. Under these assumptions, the Navier-Stokes equations in  $z$ -direction reduces to,

$$\mu \left( \frac{1}{r} \frac{\partial}{\partial r} \left( r \frac{\partial u_z}{\partial r} \right) \right) = -\rho_e E_z \quad (6.12)$$

We solve Eq. 6.12 in the radial direction, assuming the body force does not vary in this direction,

$$u_z(r) = -\frac{\rho_e E_z}{4\mu} (r^2 - R^2) \quad (6.13)$$

As we are interested in the velocity at the center of the pore, i.e., at  $r = 0$ ,  $u_z|_{r=0} = \frac{\rho_e E_z R^2}{4\mu}$ .

Further, the average EOF over the cross section of the nanopore is given by,

$$u_{avg} = \frac{\rho_e E_z R^2}{8\mu} \quad (6.14)$$

In order to obtain a mean EOF under AC field, we need to have a mean body force,  $\langle \rho_e^{AC} E_z^{AC} \rangle$ , where  $\rho_e^{AC}$  and  $E_z^{AC}$  are the amplitude of harmonic modes of space charge density and electric field. Approximating  $\rho_e^{AC}$  and  $E_z^{AC}$  by Fourier series,  $\rho_e^{AC} = \frac{\rho_{e0}}{2} +$

$\sum_{n=1}^{\infty} \rho_{e_{a_n}} \cos(\omega_n t + \theta_n)$  and  $E_z^{AC} = \frac{E_0}{2} + \sum_{n=1}^{\infty} E_{a_n} \cos(\omega_n t + \phi_n)$ , where  $\frac{\rho_{e_0}}{2}$  and  $\frac{E_0}{2}$  are the mean space charge density and electric field inside the nanopore, respectively.  $\frac{E_0}{2}$  is zero in our study, as we apply only a harmonic AC electric field. However,  $\frac{\rho_{e_0}}{2}$  is non-zero, since the nanopore is negatively charged resulting in higher concentration of cations compared to anions.  $\rho_{e_{a_n}}$  and  $\theta_n$  are the amplitude of space charge density and its associated phase angle for each mode  $n$ .  $E_{a_n}$  and  $\phi_n$  are the amplitude of electric field and its associated phase angle for each mode  $n$ .  $\omega_n$  is the frequency of each mode. From our numerical simulations, we observe that the space charge density has contributions from higher harmonic modes upto  $n = 4$ , while the higher harmonic modes ( $n > 1$ ) are negligible for the electric field oscillations. The reason for the higher harmonic modes for the space charge density is due to the asymmetric concentration distribution of the charges near the interfaces for different time intervals over a time period. This is illustrated in Fig. 6.6. For instance, Fig. 6.6 reveals that for a time period of  $t = \pi/2$  and at  $t = 3\pi/2$ , the space charge density distribution near the micro-nanopore interface differs in magnitude by 1.5 times. The asymmetric charge is observed owing to the asymmetric reservoir geometry. The amplitude of the harmonic modes and the respective phase angles, are obtained from our numerical results, by performing Fast Fourier Transform (FFT) on space charge density and electric field. To simplify our theoretical model, we consider only the first harmonic mode contribution for both the space charge density and electric field. Under these assumptions, the mean electroosmotic flow at the center of the nanopore is,

$$\langle u_z |_{r=0} \rangle = \frac{R^2}{4\mu} \left\langle \frac{\rho_{e_{a_1}} E_{a_1}}{2} \cos(\theta_1 - \phi_1) \right\rangle \quad (6.15)$$

Fig. 6.3(a) shows a comparison between the numerical results and the theoretical model. We observe that, the theoretical model illustrates a net non-zero EOF, and predicts well with the numerical simulations for frequencies,  $f \geq 1kHz$ . However, at low frequencies, the theory under predicts the numerical model, owing to the negligence of higher harmonic

modes. From Eq. 6.15, we understand that to observe a net EOF, the harmonic contributions of the space charge density and electric field, should be non-zero. Further, the relative phase difference between the first harmonic mode of space charge density and electric field plays a pivotal role in controlling the velocity of fluid flow along with its direction. Fig. 6.3(b) shows the numerical results of first harmonic mode of space charge density and normalized electric field with frequency. The amplitude of first mode of electric field is normalized with  $\frac{RT}{Fx_0}$ , where  $x_0$  is the characteristic length of the system.  $E_{a_1}$  is constant for each frequency, as the amplitude of electric field is same for all frequencies. However, the amplitude of space charge density is relatively independent of frequency, for  $f < 1kHz$ , but reduces by an order of magnitude at  $f = 1MHz$ . This is because at very high frequencies, the ions have very little time to respond to the electric field oscillation and they behave as a solid. The relative phase difference between the first harmonic mode of space charge density and electric field is shown in Fig. 6.3(c). Two interesting observations can be made from the results. First, the first harmonic mode of space charge density and electric field is out of phase with each other,  $90^{Ph.D.} < (\theta_1 - \phi_1) > 270^{Ph.D.}$ . This results in  $\cos(\theta_1 - \phi_1)$  in Eq(6.15) to be negative, resulting in a mean body force to be negative, implying it is directed from macropore towards micropore. Hence, we observe a net EOF from macropore towards micropore consistent with experimental observations. Second, the relative phase difference monotonically decreases with frequency. At  $f = 5Hz$ , the charge density and electric field are almost out of phase with each other by  $180^{Ph.D.}$ , where  $\cos(\theta_1 - \phi_1)$  reaches a maximum value. Hence, we observe maximum EOF at this frequency. The maximum EOF is observed at a frequency of  $5Hz$  owing to the asymmetric charge distribution.

In order to understand the effect of DC field on the EOF, we apply a constant DC voltage from  $V_{DC} = 5V - 40V$  in our experiments. A positive DC voltage is applied on the macropore reservoir end, while the micropore reservoir is grounded. Fig. 6.4 shows the variation of mean EOF with DC voltage. We observe a linear scaling in  $u_{EOF}$  with DC field and the direction of EOF is from macropore towards micropore, consistent with the direction of electric field.

Furthermore, the experimental EOF matches the theoretical model (Eq. 6.14) as shown in Fig. 6.4. In the theoretical model, we assume  $\rho_e = 10.43 \text{ kC}/m^3$  based on the calculations of surface charge density obtained. Also, the entire voltage is assumed to drop linearly inside the nanopore.

We further observe that the mean EOF can be modulated when we apply an AC voltage offset by the DC field. An AC voltage of  $V_{AC} = 100V$  at  $f = 1Hz$  was applied. For this AC field, the mean EOF in the absence of DC voltage is  $\langle u_{EOF} \rangle = 1.1\mu m/s$  (see Fig.6.2(b)). In principle, we would expect the mean EOF to be shifted by this magnitude when the system is driven by both DC and AC voltage compared to the EOF obtained with only DC voltage. Fig. 6.4 surprisingly shows that the difference between the mean EOF under combined AC and DC offset and without AC field is not constant but increases with DC voltage. In order to understand this phenomenon, Eq. 6.16 discusses the mean electroosmotic flow ( $\langle u_z^{AC+DC}|_{r=0} \rangle$ ) at the center of the nanopore, under combined AC and DC field,

$$\langle u_z^{AC+DC}|_{r=0} \rangle = \frac{R^2}{4\mu} \left( \frac{\rho_{e0} E_0}{4} + \left\langle \frac{\rho_{e_{a1}} E_{a1}}{2} \cos(\theta_1 - \phi_1) \right\rangle \right) \quad (6.16)$$

Here, we again consider only the contribution of the first harmonic mode of space charge density and electric field. We postulate that the mean space charge density,  $\frac{\rho_{e0}}{2}$  changes under the influence of AC+DC electric field compared to that obtained under AC field only. This further results in a change in the amplitude of the first harmonic mode of the space charge density,  $\rho_{e_{a1}}$  for combined AC+DC field compared to AC only case. This results in a change in the net body force. Owing to this situation, we observe that the difference between the mean EOF under combined AC and DC offset and without AC field is not constant but changes with DC voltage.

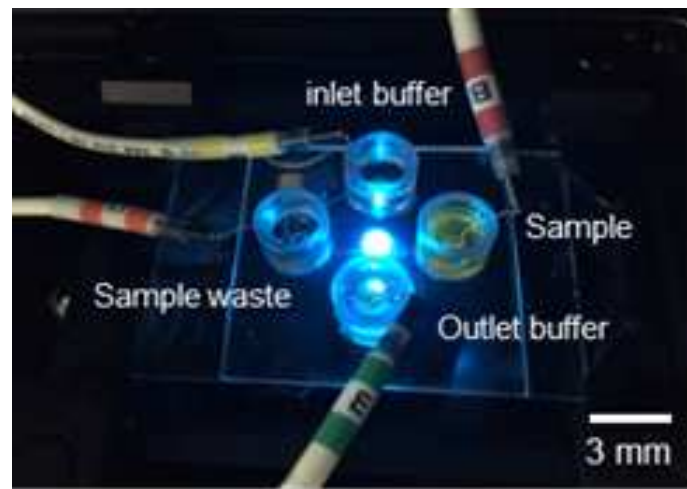
Finally, we compare the maximum EOF achieved by the current ACEO nanofluidic pump with other ACEO pumps (see Fig. 6.5). The maximum EOF achieved in the present work is 400% higher than other ACEO nanofluidic pump, indicating that one can achieve better

performance of the pump by simply breaking the symmetry of the reservoirs.

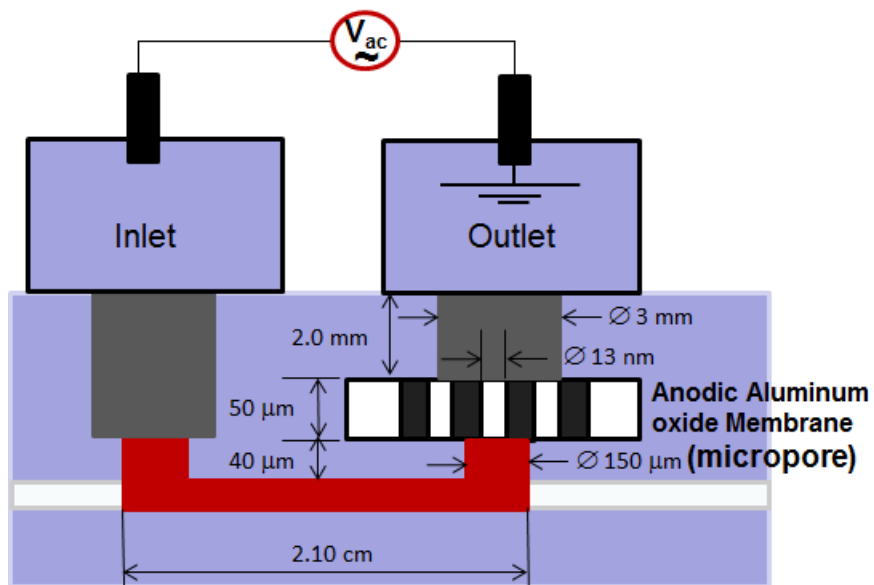
## 6.6 Conclusions

To summarize, a novel ACEO nanofluidic pump that works on the principle of asymmetric concentration polarization was experimentally constructed and was verified using our numerical simulations. Unlike ACEO microfluidic pumps reported in the literature, the fabrication of complex electrode structure is denecessitated. Our design is simple, and there is no need to chemically modify the nanopore. Further, we do not require a conical or diode nanopore. Asymmetry is achieved in the geometry of the reservoirs. Owing to this asymmetry, a net electroosmotic flow could be achieved under the action of an AC electric field. Using numerical simulations and theoretical models, we postulate the out of phase behavior between the first harmonic mode of the space charge density and the electric field to be responsible for the net EOF inside the nanopore. The magnitude of the mean EOF is controlled by varying the frequency or amplitude of AC field. Furthermore, we compare the maximum EOF achieved by our design with other ACEO pumps. The maximum EOF achieved in the present chapter is 400% higher than other ACEO nanofluidic pumps. We believe, the present design could be potentially used to control the translocation speed of fluids, ions, biomolecules for efficient DNA sequencing and protein translocation using nanopores. Furthermore, in the present device, we do not observe any bubbles in the nanopore system which is a predominant limitation of a DC driven system.

## 6.7 Figures

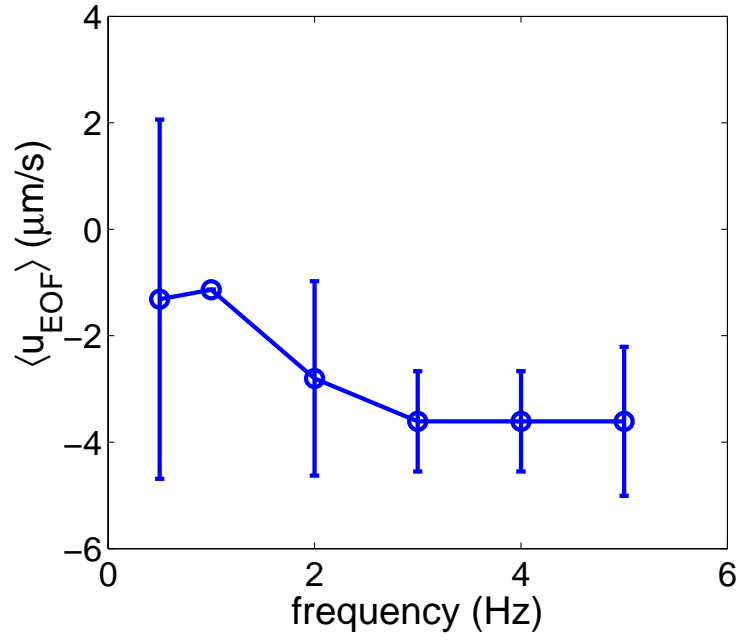


(a)

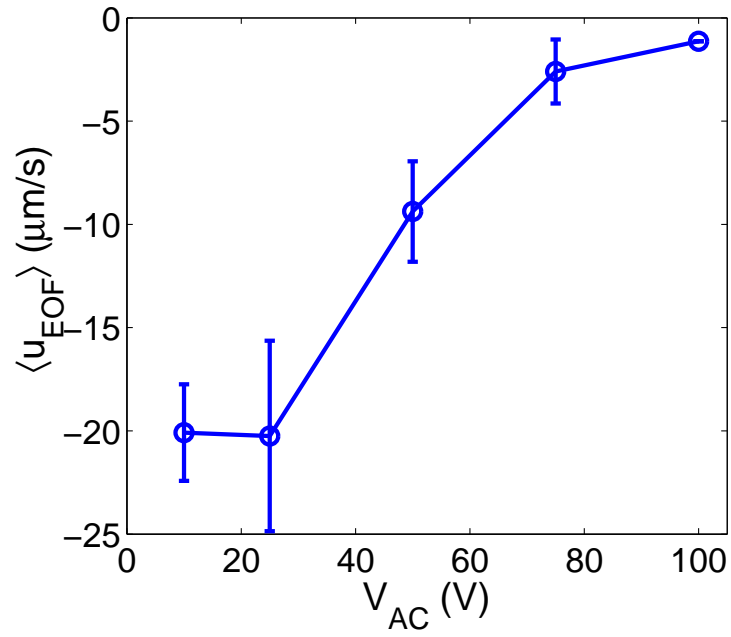


(b)

Figure 6.1: (a) Experimental set-up of a typical micro-nano-macropore system driven by an AC electric field. The nanopore membrane is made of Anodic Aluminum oxide (AAO). (b) 2D schematic illustration of the experimental set up.



(a)



(b)

Figure 6.2: Variation of mean electroosmotic flow (EOF) with (a) frequency at a fixed AC amplitude,  $V_{AC} = 100$  (b) amplitude of AC field at a fixed frequency,  $f = 1\text{Hz}$ . The negative sign indicates net EOF flows from macropore towards micropore. Here  $V_{DC} = 0$ .

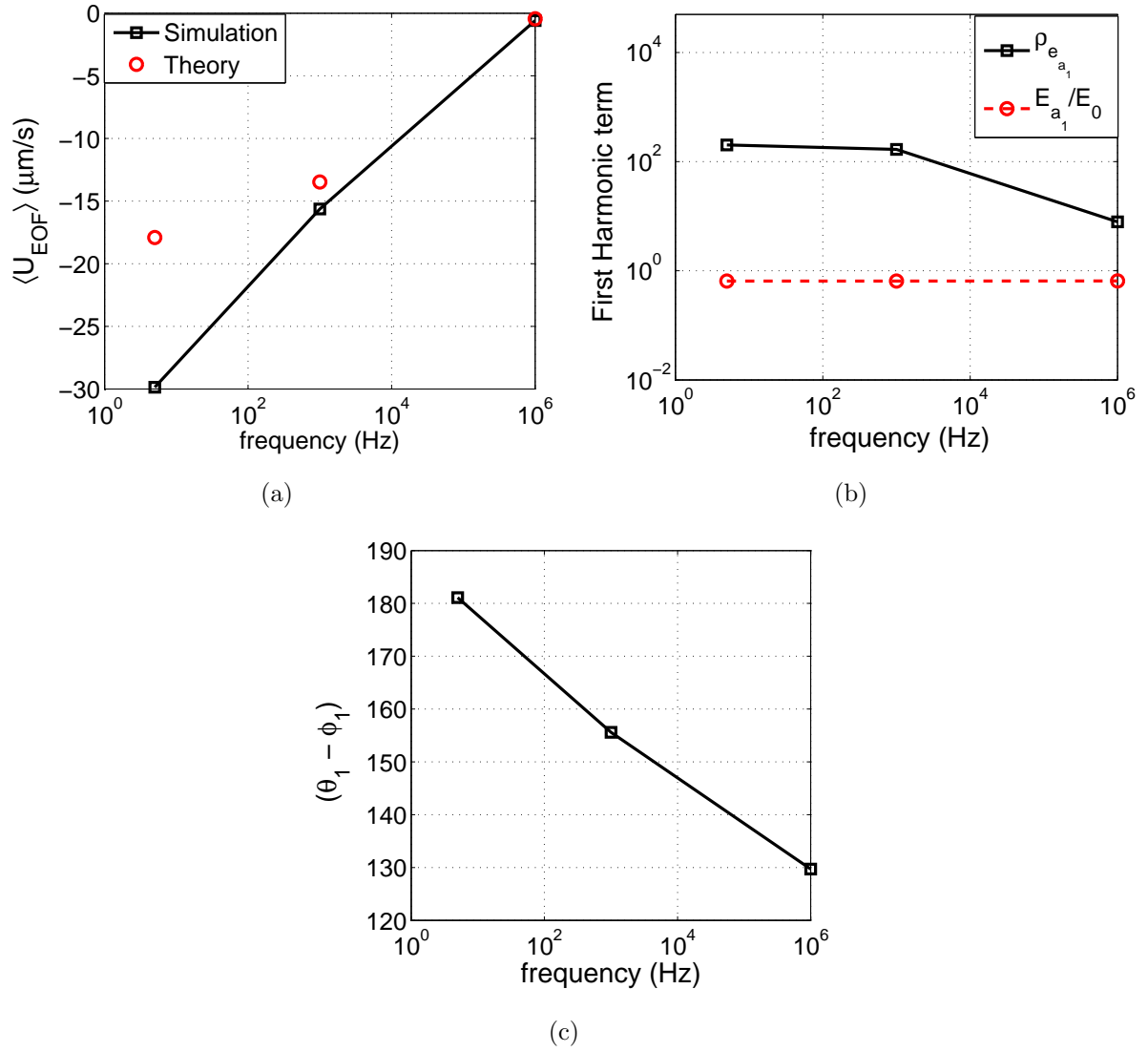


Figure 6.3: Variation of (a) mean electroosmotic flow (EOF), simulation (squares) and theoretical model (circles). The negative sign indicates net EOF flows from macropore towards micropore. (b) first harmonic mode of space charge,  $\rho_{e_{a_1}}$  and electric field,  $E_{a_1}$  (c) net phase difference between  $\rho_{e_{a_1}}$  and  $E_{a_1}$  with frequency, at an AC amplitude,  $V_{AC} = 10V$ . Here  $V_{DC} = 0$ .

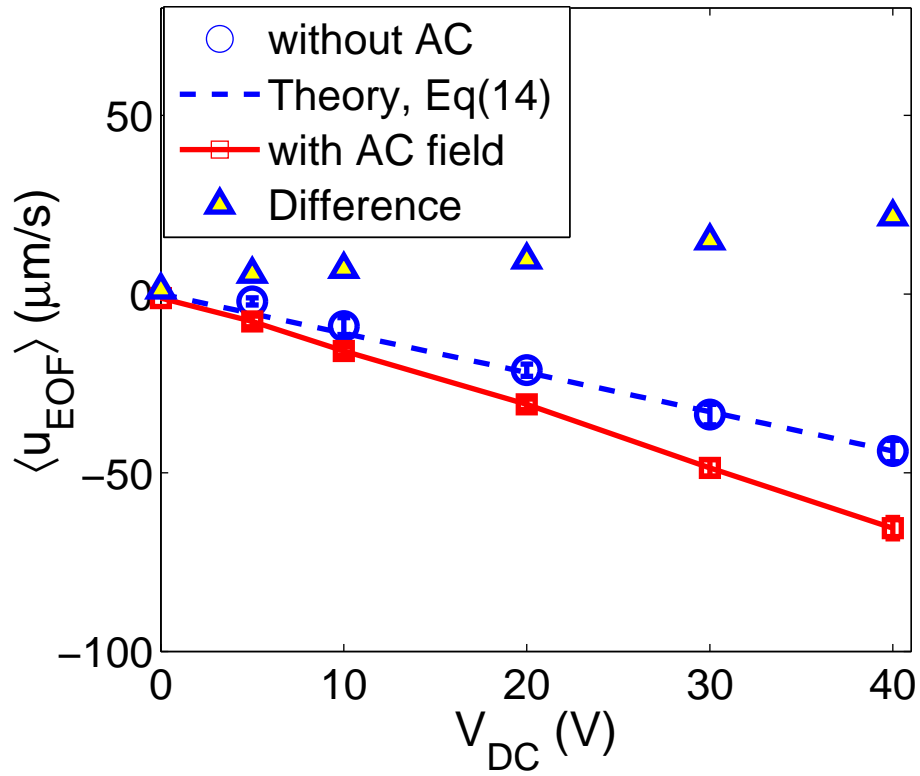


Figure 6.4: Variation of mean electroosmotic flow with DC voltage, without AC voltage (circles - simulation, dashed line - theoretical model) and with an AC voltage (squares) of amplitude,  $V_{AC} = 100V$  and at a fixed frequency,  $f = 1Hz$ . The difference between mean EOF with and without AC voltage (triangles) monotonically increases with  $V_{DC}$ . Here, DC voltage is applied at the macropore.

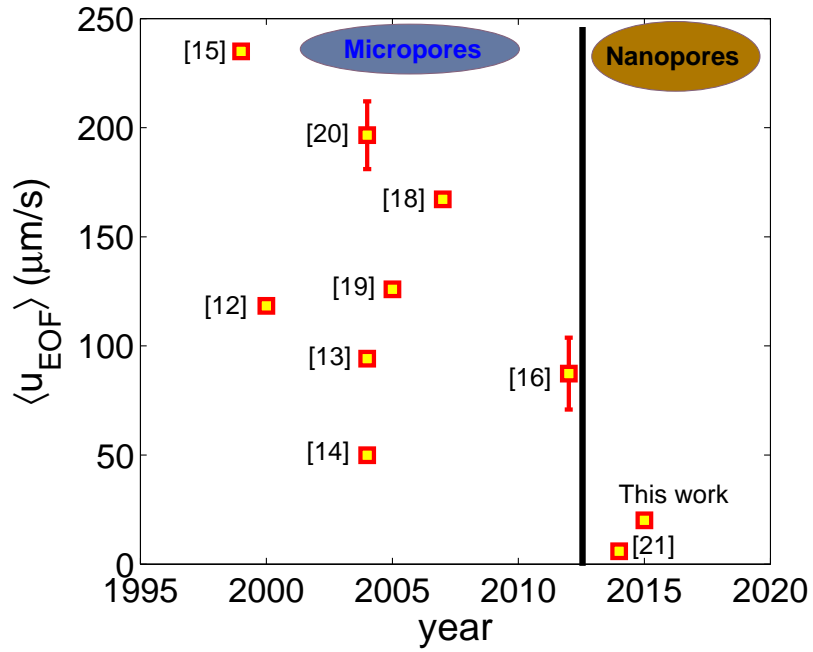


Figure 6.5: Mean Electroosmotic velocity versus year for both microfluidic device and nanofluidic device driven by an AC electric field. Each data point represents the maximum electroosmotic velocity achieved in each device; for each data point the relevant reference is shown in square brackets. There is no correlation between year and electroosmotic velocity. The mean EOF is 400% higher than the mean EOF achieved in other ACEO nanofluidic pumps.

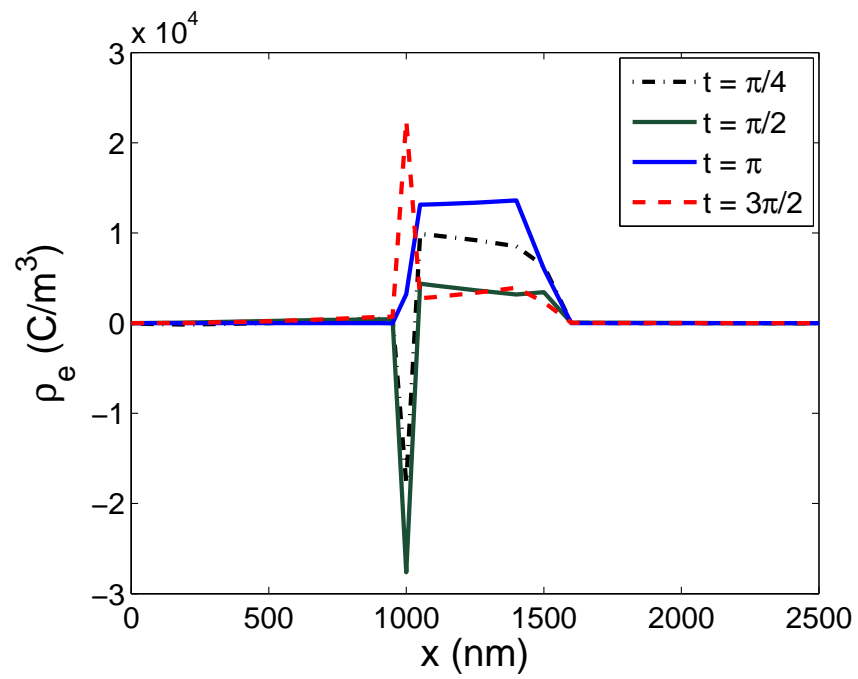


Figure 6.6: Charge density distribution with respect to different time periods throughout the entire micro-macro reservoir system.

## 6.8 References

1. [Howorka and et al.(2009)] S. Howorka, et al., Chem. Soc. Rev. 38 (2009) 23602384
2. [Chen and et al.(2010)] Z. Chen, et al., Nat. Mater. 9 (2010) 667675.
3. [Piruska and et al.(2010)] A. Piruska, et al., Chem. Soc. Rev. 39 (2010) 10601072.
4. [Kim and et al.(2007)]S. J. Kim, et al., Phys. Rev. Lett. 99 (2007) 044501.
5. [Qiao and et al.(2005)] R. Qiao, et al., Colloid. Surface. A 267 (2005) 103109.
6. [Jin and et al.(2007)]X. Jin, et al., Langmuir 23 (2007) 1320913222.
7. [Mani and et al.(2009)]A. Mani, et al., Langmuir 25 (2009) 38983908.
8. [Postler and et al.(2008)]T. Postler, et al., J. Colloid Interface Sci. 320 (2008) 321332.
9. [Choi and et al.(2009)]Y. S. Choi, et al., J. Colloid Interface Sci. 333 (2009) 672678.
10. [Pu and et al.(2004)] Q. Pu, et al., Nano Lett. 4 (2004) 10991103.

# Chapter 7

## Conclusions

In chapter one, I have postulated the origin of large yet finite differential resistance in the limiting resistance region, and the transition to the overlimiting current region in a nanoporous architecture owing to the influence of external microporous environment. The regimes are corroborated by demarcating the concentration physics in the induced space charge region at the nanoporous junction. I challenge the existing electroosmotic flow instability (EOI) mechanism as the origin of overlimiting current and conjecture the charge redistribution as the true origin. Furthermore, I manifest anomalous current rectification, summarizing an enhancement of the current, under combined AC/DC electric field. The anomalous current characteristics sophisticates in the field of energy storage systems, supercapacitors, water desalination and selective species separation.

In chapter two, I put forth an in-house computational impedance spectroscopic model (CIS) to characterize the fundamental electrochemical properties of a nanoporous architecture leveraged with a microporous environment. Under no external DC bias and in the Ohmic regime, we conferred two distinct arcs. The low frequency diffusional arc characterizes the diffusion–transport and the electric double layer charging effects at the nano-junctions, while the high frequency geometric arc characterizes the electric migration and displacement current effects inside the nanochannel and the microporous architecture. An anomalous inductive arc at low frequencies was inferred in the overlimiting regime. The origin of this arc was attributed to the phase effects between the harmonic disturbance of the total ionic concentration and the electric field in the induced space charge region. Using the impedance spectra, I highlight the important time scales at which negative and positive AC rectification effects are corroborated in the system. Finally, equivalent circuit models are designed

to interpret the impedance response.

In chapter three, we put forth a novel nano-diode, under which the current rectification factor can be tailored by controlling the asymmetry ratio between the reservoir baths that are connected to opposite sides of a nanoporous membrane. As the asymmetry ratio of the micropore and macropore increases, the current rectification factor of the device increases as well. The current rectification is a result of the polarity dependent extension of the concentration polarization depleted zones into the fluidic regions with different cross-sectional areas and critical dimensions. Chaotic oscillations in the measured current indicate that electroconvection is the origin of  $1/f$  type pink dynamics.

In chapter four, I postulate an advanced numerical study of a nanopore leveraged to fluidic reservoirs of asymmetric cross-sectional environments. The system exhibits local non-equilibrium chaotic motion of ions under the action of an applied electric field. I conjecture the dynamic cascading/avalanche of charges at the nano-junction as the fundamental mechanism for chaos. Further, I correlate the  $1/f$  type pink dynamics in the power spectral density to the voltage dominant chaos and  $1/f^2$  type dynamics to the macropore reservoir dominant chaos.

In chapter five, I conclude a transition from stable and steady ion transport to unstable/chaotic current oscillations inside the nanoporous membrane when the cation transference number reaches unity (under near-ideal nanoporous membrane). I postulate the mechanism behind the chaotic current oscillations to the propagation of depletion region inside the nanopore, and the non-homogeneous distribution of the ions owing to the nonequilibrium instability in the potential. The instability manifests in bi-directional hopping of the ions, thereby changing the directionality of the currents. Finally, I establish a computational correlation between the low frequency  $1/f$  type dynamics to chaos, and postulate a new mechanism for nonequilibrium  $1/f$  type pink dynamics.

In the final chapter of my dissertation, I put forth a novel AC electroosmotic nanofluidic pump that works on the principle of asymmetric concentration polarization. I collaborated

with experimentalists to manufacture a nano pump and reveal the transport physics using my computational models. Unlike AC electroosmotic micro pumps, the fabrication of complex electrode structure is denecessitated. Our design is simple, and there is no need to chemically modify the nanopore. Asymmetry is achieved in the geometry of the reservoirs. Owing to this asymmetry, a net electroosmotic flow (EOF) was achieved under the action of an AC electric field. Using numerical simulations and theoretical models, I conjecture the out of phase behavior between the first harmonic mode of the space charge density and the electric field to be responsible for the net EOF inside the nanopore. The maximum EOF achieved is 400% higher than other ACEO nanofluidic pumps.